THE ROLE OF GEOMETRY IN THE HEMODYNAMICS ASSOCIATED WITH STROKE DEVELOPMENT IN SICKLE CELL ANEMIA

A Dissertation
Presented to
The Academic Faculty

by

Christian Poblete Rivera

In Partial Fulfillment
Of the Requirements for the Degree
Doctor of Philosophy in Biomedical Engineering

Georgia Institute of Technology
Emory University
Peking University

May 2019

THE ROLE OF GEOMERTY ON THE HEMODYNAMICS ASSOCIATED WITH STROKE DEVELOPMENT IN SICKLE CELL ANEMIA

Approved by:

Dr. Manu O. Platt, Advisor
School of Biomedical Engineering
Georgia Institute of Technology

Dr. Yunlong Huo, Advisor
School of Mechanics and Engineering Science
Peking University

Dr. Alessandro Veneziani
School of Mathematics and Computer Science
Emory University

Dr. Edward Botchwey
School of Biomedical Engineering
Georgia Institute of Technology

Dr. Wilbur Lam
School of Biomedical Engineering
Georgia Institute of Technology

Dr. Tequila Harris
School of Mechanical Engineering
Georgia Institute of Technology

Date Approved: 02 12 2019

To my parents for their unwavering support and encouragement

ACKNOWLEDGEMENTS

I would first like to thank the members of my thesis committee for their invaluable support and feedback over the years, Dr. Manu Platt, Dr. Yunlong Huo, Dr. Alessandro Veneziani, Dr. Edward Botchwey, Dr. Wilbur Lam, and Dr. Tequila Harris. Dr. Harris was always able to calm me down before a committee update, and her emphasis on focusing on the conclusions and major findings rather than the minute details, has helped me improve the overall story for my thesis. I will always appreciate Dr. Lam's clinical feedback, insight into the major hurdles of my project. I thank Dr. Botchwey from asking the hard questions and trying to keep me focused on the larger picture. His insight has been very valuable, and he has really helped with developing the story for my dissertation. I would also like to thank him for giving me the opportunity to be his teaching assistant in the past. Teaching has been one of the most fulfilling parts of graduate school, and Dr. Botchwey really allowed me to take a major role in the class. I was able create a lesson plans, write and grade exams, and heavily interact with students. Most other TA's do not get such freedom with the classes they teach, and I thank Dr. Botchwey for trusting me with such responsibilities. Lastly, it has been wonderful to work with him in various other projects. Working with Jada Selma from his lab on the sickle femur project has been wonderful, and I was glad to use my skills in under areas of research. Additionally, I have learned a lot I learned a lot about grant writing from you in our bi-weekly sickle meetings, and your insight in those matters has help me improve aspects within my own writing.

I owe much of my knowledge in computational fluid dynamics to Dr. Veneziani. It was in his class back in 2013 where I first learned the fundamentals of finite element analysis and the process for performing CFD. It was through his tools that I was able to accomplish much of the reconstruction and simulations required for my project. In addition, I appreciate how he would always make time for me when I was struggling with my simulations and would help me go through my scripts to determine the problem. Dr. Veneziani has also created a great team of knowledgeable personnel that could provide me with feedback. Tiziano, Marina, and Huijuan have all assisted me in some way during my thesis. It was sometimes difficult being the only person in my lab performing CFD, but it was great to know that I could always go to Dr. Veneziani and his team for their knowledge and expertise.

I can never thank Dr. Huo, enough for letting me join his lab and taking care of me during my time in China. The wonderful events I was able to experience at Peking University was in part due to him. Dr. Huo runs his lab very similarly to Dr. Platt, so I had no problem adjusting and joining right in with everyone else. Dr. Huo treats his lab like a giant family so I never felt like an outsider. I appreciate how he provided the sickle animals and tools necessary to do my research and created an environment where I had no difficultly performing the experiments I needed. Lastly, I also appreciate how Dr. Huo allow me to take short trips to explore China and Asia so I could experience an unfamiliar culture.

I owe the most to my career and professional growth to Dr. Manu Platt. Dr. Platt has been an incredible mentor, and his advice on research, time-management, assertiveness, and just general life are things I will never forget. I appreciate how he has

never given up on me even when I felt like my research was going nowhere. He always knew when to push me towards the next stage, even when I thought I wasn't ready and for that I will always be grateful. I also want to thank him for the numerous career opportunities he has given me. Allowing me to go to conferences in Italy, and to research abroad in China. They were all amazing experiences and I truly appreciate those opportunities. Lastly, I just want to thank him for creating just a diverse and fun learning environment. The Platt lab is like a second family and I truly have enjoyed my time with everyone there. The diversity of individuals that Dr. Platt recruited into his lab has created a melting pot where we can all learn and experience each other's culture. Despite the times when coming to work was difficult because I was going crazy over research, I knew everything would be ok because I was surrounded by so many amazing individuals. I had an amazing graduate experience and I know it was in part to how Dr. Platt established his lab.

I have been fortunate to be a part of two wonderful labs one in America and one in China. Both are filled with amazing people and everyone there has impacted me in some way during my dissertation. To being I would first like to thank my lab twin Dr. Meghan Ferrall-Fairbanks. Meghan and I started at the same and it has been interesting to watch our journey though graduate school. When I first began, I was heavily invested with the wet lab, and Meghan was mostly performing computational modeling. However, as time progressed, I soon became more involved with my CFD simulations and Meghan began doing more wet lab work. As we transitioned to each other's specialties it was great to talk to Meghan about each other's struggles and how to troubleshoot problems. Watching her become so proficient in the wet lab has been a pleasure, and now I can go to her about experiments I haven't performed before. In addition, Meghan is probably the most

organized person I will ever meet. I know for a fact that a lot of lab events, such the move to EBB and journal club scheduling would not have been as smooth without her leading the way. She has a great apt for organization and I can only wish to be half as skilled as her.

In addition to Meghan, I would also like to thank Dr. Philp Keegan, Dr. Ivana Parks, Dr. Catera Wilder, and Dr. Keon-young Parks. Known as the "Core Four" these students were the first to graduate in Dr. Platt's lab and helped establish the foundation for which this this lab was built. All four of them helped create a wonderful lab environment, and truly live by the concept of work hard play hard. Their enthusiasm for science was an inspiration for me when I first joined the lab, but in addition their ability to goof off and have fun after a hard week was also a lesson I needed to learn. Phil was the first in our lab to study sickle cell anemia, laying the foundation for much of my own work. He is incredibly inquisitive, and his knowledge in so many random facts is astonishing. Keon-young's work ethic is something I will always envy, the amount of work she was able to accomplish in such a short time is amazing. In addition, her baking skills are amazing, and I still miss the random desserts she would make. I will always appreciate Ivana's ability to remain so calm and collected despite the challenges ahead. I've never met someone who can go with the flow as easily as Ivana, and it's a skill I'm still trying to master. Lastly, I admire Catera's fortitude, her ability to work through such a complicated project provided me inspiration when I was struggling with my own research.

A year after Meghan and I joined the Platt lab, the now Dr. Akia Parks and Andrew Shockey joined. They were a great addition to the lab and with Meghan and I, the four of us were able to carry the traditions the first four left us. Like Keon-young Andrew is an

amazing chef, but in addition he's calm and collected like Ivana, and knowledgeable like Phil. Andrew is a truly talented person with amazing oratory skills, and I will always appreciate his feedback during grad school. Akia is just as incredible, she brought a lot of life to the lab and was always taking care of us all. Her ability to distill complicated topics is amazing, and I will always appreciate her encouragement during difficult times. Simone Douglas joined a few years after Akia and Andrew, but regardless of the age gap she has kept the Platt lab tradition going. Simone adopted many of the skills from previous graduate students before her, such as Meghan's organization and Catera's fortitude. Simone has an amazing personability and I know in the future she will make a wonderful professor.

The latest recruits to the Platt lab include Victor Omojola and Darwin Carbajal. Victor is newest person to take upon sickle cell research, and his assistance with my own project is something I am thankful for. I could not have finished as many of the reconstructions as I did without his assistance. In addition, Victor is a great chef and I know he will continue the tradition of amazing desserts in Platt lab. Lastly, Darwin, though he is the newest person, his excitement for research is inspiring and I hope it continues throughout his degree. I would also like to thank all the post-docs and research scientist who have been part of the Platt lab, Dr. Kristi Porter, Dr. Hannah Song, Dr. Chris Kieslich, Dr. Adeola Michael, and Maurizzo Affer. Their mentorship and guidance have been invaluable. Hannah and Chris, especially, have been a great source of help for my project. The number of times I was going crazy over some piece of data, and they were there to help me figure it is innumerable.

From my lab in China, I would first like to thank Dr. Feng Yundi “Fendy”. My entire survival during my first month in China is entirely due to Fendy’s help. She found me housing, established my bank account, and taught me how to order food. Fendy is one of the nicest people I have ever met and will always try to help those in need. After Fendy, the main team I worked with was Li Li and Nu Pei. These two are amazing researchers and I wish I could be as comfortable working with animals as they were. In addition to these two I would also like to thank all the people in Baoding at Heibei University, who helped me with my project. Lastly, I would also like to thank, TingTing Fan, Xu Huang, Qiao Li, Wu Hao, and Jaheong Li. I know from talking with others that transitioning to our Chinese labs wasn’t easy, but I felt I transition the best. These people never made me feel excluded and I honestly felt like a true member of the lab. Especially Jaheong Li and Wu Hao, who had no trouble trying to beat me in basketball. It was an honor to work with all of you and I hope to meet all of you again in the future.

I would like to thank Dr. Cheng Zhu for creating the joint BME Graduate Program between Georgia Tech, Emory, and Peking University. Not only was I able to live abroad in Beijing for year, I was able to perform a high level of research during this time. It is often difficult to describe my time while in China, as it was one of the greatest most life-shaping events that has ever occurred and will forever leave a last impacting on who I am as a person. I will never forget my experiences nor the friends I met over there, and it is all due to the efforts of Dr. Zhu and all the personnel at Peking University.

I have had the pleasure to work with several undergraduate students. Beginning with Nina Mohebi, I’ve also had the pleasure to train Shuxin Li, Dakarai Moton, George McAlear, “Cheryl” Shuangyi Cai, Victor Ariyo, and Keval Bollavaram. All these students

have contributed to my thesis and I know I could not have done everything I was able to accomplish without their assistance. Though my time with Nina, Shuxin, and Dakarai was short, as I was only able to work with them for the length their summer programs, I appreciate their help and assistance through the first few years of my thesis. It was a pleasure to bounce ideas with them and try experiments I haven't performed before. Even though some of those experiments did no work, their interest and enthusiasm for science helped drive me to form new ideas that ultimately shaped my dissertation. It has been a pleasure to see how each of them has grown, all pursuing different avenues in biomedical engineering. Nina is now in industry, Shuxin graduate school, and Dakarai medical school, and I wish all of them success with their future careers.

After returning from China, I was excited to analyze all the data I had collected but I was faced with a mountain of tasks that seemed almost impossible to overcome. The undergrads who helped me tackle this mountain consisted of George, Cheryl, Victor, and Keval. I gave each of them large projects, and it was through their effort I was able to complete the second aim of my dissertation. George was the first person I recruited, and who I met him sporadically during a volunteer event. Asking if he wanted to help me with my research was probably one of the greatest decisions I have ever made during graduate school. George has been with me the longest of any undergrad, over a year at this point, and he is an interesting individual who's both quirky and down to earth. However, if you put him in front of a computer and ask him to write you a script, he will have something for you in no time. George's ability behind the computer is truly incredibly and I know the programs I asked him to write would have taken myself two to three times as long. From developing the functions which compiled all the velocity profiles together to producing the

complicated graphs needed for my paper, I could always rely on George to write a useful script. I can really seem him doing incredible work in the future and can only hope that whoever hires him will use his computational skills to its fullest.

After George I took upon Cheryl, and she joined a unique time during my PhD. I was in the middle of writing a paper and George and I could not finish everything that needed to be done. Despite not being familiar with the project she jumped right in with no complaints. While George was my "coder" Cheryl was my "worker". When Cheryl joined, I gave her the promise that if she helped me with my computational work that I will give her the opportunity to work in the wet lab. She took upon this request whole-heartedly and completed every task I asked of her. No matter how tedious, I could always rely that she would finish the task in a timely matter. Halfway through her second semester with me, Cheryl began working with Hannah as per the stipulations of my promise. I was sad to have such a great worker leave, but it was great to see her work in the wet lab space. I could really tell she enjoyed her time doing wet lab experiments and was becoming more skilled in those areas. I wish her the best in her future pursuits in graduate school and know she will do just fine.

My last cohort of undergraduate students consisted of Victor "Young Vic" and Keval. Vic is an incredible person, and despite the short time he was able to work for me he took upon the project with all its complexity. I respect his tenacity and know he will do great pursuing his future endeavors. Keval is like my second Cheryl. Part of the reason I could part ways with Cheryl after her amazing work, was because Keval was there to pick everything up. When I recruited Keval, I was a part of several different projects. In addition to my thesis, I was part of a sickle bone project and a sickle vasculopathy project. Keval

was my go-to when I need some aspect completed in any of these projects. He is a fast learner and would quickly finish the tasks asked of him. I wish him the absolute best when he begins medical school in a few years. In addition to my own undergraduate mentees I would like to thank all the undergraduate and high school researchers that have gone through our lab, such as Binbin, Monet, Daniel, Suhass, Charline, Johnathan, Han, Simon, Katrina, Niara and all the rest. Dr. Platt has truly created an environment of mentorship in his lab, and it has been a pleasure watching each of these students grow in their individual skills and abilities.

I would like to thank all my students. When I first started graduate school, I wasn't sure what I wanted to do when I finished, but when I began teaching during my TA years, I really found a passion for education and mentorship. Watching my students learn and grow throughout the semester has been one my proudest accomplishment in graduate school. It is through my interactions with them that I know I want to purse a path in education.

Lastly, I would like to thank the funding sources that provided the monetary support to make my research possible. The National Science Foundation for supporting the PKU program and giving scientist such as myself an opportunity to pursue research abroad. Lastly, the Ford Foundation pre-doctoral fellowship, which gives opportunities to minority researchers pursuing careers in academia and providing a network such that academics in all fields could interact with each other.

TABLE OF CONTENTS

LIST OF TABLES

LIST OF FIGURES

LIST OF SYMBOLS AND ABBREVIATIONS

ACA	Anterior cerebral artery
CCA	Common carotid artery
CFD	Computational fluid dynamics
ECA	External carotid artery
FEA	Finite element analysis
FEM	Finite element method
ICA	Internal carotid artery
MCA	Middle cerebral artery
MRA	Magnetic resonance angiogram
RBCs	Red blood cells
SCA	Sickle cell anemia
SCD	Sickle cell disease
TCD	Transcranial doppler
TMMAV	Time-average
v	Velocity (cm/s)
P	Pressure (dynes/cm^2)
t	Time (s)
τ	Shear Stress (dynes/cm^2)
μ	Viscosity (cP)
ρ	Density (kg/m^3)

SUMMARY

Sickle cell anemia (SCA) is a genetic blood disorder which affects over 4 million people globally. Though SCA is caused by a single point mutation in the hemoglobin of red blood cells, this change has devastating affects which can impact the entire human body and reduce life expectancy. Amongst the complications associated with SCA, there is a 200-fold increase in the likelihood of ischemic stroke in children and adolescents. Approximately 11.5% of individuals with SCA will develop an overt stroke before 18 years of age, and those between 2 and 5 at the greatest risk. Additionally, 37% of individuals will have a silent stroke before the age of 14. The only method to determine stroke risk is with through transcranial doppler and measuring blood flow in the cerebral arteries. Individuals who have a time-average maximum-mean blood velocity exceeding 200 cm/s have a significantly elevated risk of developing a stroke in the future. The objective of this thesis is to provide insight into these elevated blood velocities by identifying and validating flow-mediated mechanisms predisposing children with sickle cell anemia to strokes.

Individuals with SCA have shown remarkable cerebrovascular remodeling characterized by intimal hyperplasia and luminal narrowing, specifically in the distal internal carotid artery (ICA), middle cerebral artery (MCA), and anterior cerebral artery (ACA). Formation of stenoses in these arteries could produce elevated velocities; however, higher blood velocities have also been measured in individuals despite a lack of morphological abnormalities. Therefore, the relationship between geometry and hemodynamics is crucial to understanding the biomechanical mechanisms causing accelerated stroke development in SCA.

Using computational fluid dynamics (CFD), we have demonstrated that individuals with SCA have elevated blood velocities, even when inlet boundary conditions were equivalent to those without SCA. This indicates geometrical differences are a plausible cause for the elevated velocities indicative of strokes risk. In addition to these findings, individuals with SCA had increased regions of low and oscillatory shear stress, a stimulus for endothelial dysfunction and vascular remodeling. The role of geometry was further investigated using the Townes sickle cell transgenic mouse model. Through a combination of live imaging with ultrasound and perfusion casting, morphometrics were measured in the carotid and cerebral arteries of homozygous sickle (SS) and heterozygous sickle (AS) mice. SS mice were found to have significantly larger common carotid artery diameters than AS mice, and significantly larger diameters in the extracranial and intracranial portions of the ICA. Significant narrowing was also determined along ICA, decreasing by as much as 70%, such that the terminal tributaries of the MCA and ACA had no differences in size between genotypes. CFD simulations with mouse geometries indicated that narrowing in the cerebral arteries of SS mice correlated with elevated cerebral blood velocities. Specifically, narrowing along the right ACA produced significantly higher time-average maximum-mean velocities in mice afflicted with SCA. This work has laid the framework for determining potential biochemical mechanisms in SCA that are altering the cerebrovascular geometry and inducing elevated blood velocities, as well as enabling methods for testing future therapeutics.

CHAPTER 1 INTRODUCTION

1.1 Motivation

Individuals with sickle cell anemia (SCA) have a risk of stroke with children between the ages of 2 and 8 at the greatest risk [1, 2]. Approximately 11.5% of adolescents with SCA will have an overt ischemic stroke before the age of 18 a 221-fold increase to age matched non-sickle counterparts [2]. Additionally, up to 37% of children by 14 years of age will have a silent stroke, which can go undetected for years but impair mental function and cognitive abilities [3]. Currently, transcranial doppler (TCD) is the only technique used to diagnose stroke risk, by measuring blood flow in the cerebral arteries. Elevated time-average maximum mean velocities (TAMMV) exceeding 200 cm/s in the internal carotid (ICA), middle cerebral (MCA), or anterior cerebral arteries (ACA) are a strong indicator of stroke risk in SCA [1]. More than 60% of individuals who have surpassed this threshold will develop a stroke within 3 years of diagnosis if left untreated [1]. Cerebral angiograms of individuals who have suffered from strokes have shown that the occurrence of stenotic lesions in the cerebral arteries [4, 5]. Characterization of these stroke lesions have shown remarkable vascular remodeling characterized by intimal hyperplasia and luminal narrowing [5], but it is unclear how such accelerated remodeling is occurring in children with SCA. While it is expected for high centerline velocities to occur through stenotic regions in arteries, morphological abnormalities are not always detected by angiogram despite TCD measurements indicating elevated velocities [6]. Therefore, analyzing the relationship between the geometry and hemodynamics is crucial to understanding the potential biomechanical mechanisms causing accelerated stroke development in SCA.

Computational fluid dynamics (CFD) offers a powerful tool for investigating the cardiovascular system. Based on numerical approaches that use equations derived from physics to simulate blood flow, hemodynamic forces can be approximated in regions where traditional tools are ineffective, and thus can be used investigate the biological processes that are occurring. Wall shear stress plays an important role in cardiovascular health, with low and oscillatory shear inducing endothelial dysfunction and initiating the early stages of vascular remodeling [7-9]. Known to occur at specific regions of the cardiovascular system, such as bifurcations a dynamic cycle is created where the geometry affects the hemodynamics, which then affects the biochemistry that in turn affects the geometry [10]. This thesis investigates the effect of sickle cell anemia on the vascular geometry in order to understand the hemodynamics of stroke risk.

1.2 Research Objectives

The **objective of this research** is to identify and validate flow-mediated mechanisms of accelerated cerebrovascular remodeling predisposing children with sickle cell anemia to strokes. Therefore, the **central hypothesis** is that the pathophysiology in sickle cell anemia changes the cerebrovasculature, altering the hemodynamics and producing elevated cerebral artery velocities. The central hypothesis will be tested through following aims.

1.2.1 Specific Aim 1: Investigate geometric scenarios sufficient to recapitulate the hemodynamic profiles of children with sickle cell anemia at risk for stroke

Hypothesis: Elevated velocity profiles in children with sickle cell disease are generated from remodeling of the cerebral vascular anatomy.

Researchers often study the hemodynamics of the microvasculature in relation to sickle cell anemia. This creates a gap of knowledge in the large artery system where abnormal velocity profiles also exist. Two- and three-dimension computational models were used to investigate the hemodynamics in sickle cell anemia. In the 2D model, the characteristics for sickle blood were investigated in order to determine appropriate properties for simulating blood flow in SCA. Additionally, the impact of stenoses were examined to elucidate the magnitude required to produce abnormal velocities associated with stroke risk. In 3D, patient specific models were generated from magnetic resonance angiograms of individuals with and without SCA to determine the impact of geometry in producing elevated velocities associated with stroke risk.

1.2.2 Specific Aim 2: Investigate the hemodynamics and morphology in the carotid and cerebral arteries of a sickle cell transgenic mouse model.

Hypothesis: Sickle cell anemia causes changes to the cerebral vascular anatomy that produce elevated velocity profiles.

Mouse models can be powerful tools used for investigating cardiovascular diseases, however it is unknown if the hemodynamic abnormalities observed in humans with SCA also exist in murine counterparts. Using the Townes sickle cell transgenic mouse model, cerebral blood flow was examined in homozygous sickle (SS) and heterozygous sickle (AS) mice. Blood flow cannot be directly measured in the cerebral arteries of mice;

therefore, a computational model was developed to approximate cerebral blood velocities. Subject specific boundary conditions were acquired using a combination of ultrasound imagining and vascular casts. Velocities in the common carotid and internal carotid arteries were measured using high-frequency ultrasound and used as an inlet boundary condition for the computational model. To obtain subject specific geometries, an *insilico* model was created from micro-computed tomography images of a casting created by injecting a radio-opaque polymer into the cardiovascular system. The model was validated through comparisons of morphological and hemodynamic measurements taken in a live mouse.

CHAPTER 2 BACKGROUND

2.1 Sickle Cell Anemia

Sickle cell anemia (SCA) is of the most common genetic blood disorders in the world. More than 300,000 babies are born each year with SCA, and approximately 4 million worldwide are afflicted with the disease [11]. In the US alone, 100,000 people have SCA, which incurs a healthcare cost in excess of $1 billion US dollars annually [12, 13]. Life expectancy is also significantly reduced in males and females with SCA, living to an average of only 42 and 48 years of age, respectively [14].

Sickle cell anemia and sickle cell disease (SCD) are caused by a mutation in β-globin, a subunit of the hemoglobin protein. The sickle or "S" mutation in β-globin is denoted as HbS, as opposed to the normal β-globin gene referred to as HbA. The term "sickle cell disease" is an umbrella term that includes sickle cell anemia, which is defined as homozygous sickle (HbSS or SS), sickle trait (SCT) (HbAS or AS), and other sickle variant diseases that are combinations of HbS with another abnormal β-globin protein, for example HbC, HbD, HbE [15]. HbS is a single point mutation that changes a codon from GAG to GTG, and results in a negatively charged glutamic acid being substituted by a neutral charge valine, in the sixth position of β-globin [16]. In arterial circulation where the oxygen concentration is high, hemoglobin cooperatively binds and carries oxygen inside red blood cells. The protein conformation when carrying oxygen shields valine from the surrounding aqueous environment in the cytoplasm of RBCs; however, upon entering the capillaries a gas exchange occurs that leads to the release of oxygen, and results in a conformational change that exposes the hydrophobic valine to the surrounding aqueous environment. Under these conditions the hemoglobin molecules polymerize causing the

formation of a fibrous precipitate that change RBCs into the classical “sickle” shape for which the disease is known.

During sickling the overall RBC density, viscosity, and stiffness increase, which also increases the viscosity of whole blood by as much as 3-7 times at an equivalent hematocrit to individuals without SCA [17-20]. The sickling process also causes increased RBC lysing in individuals with SCA leading to lower levels of hematocrit (25%) as compared to those people without the genetic disease (45%) [17-20]. The repetitive polymerization and melting of hemoglobin fibers in the RBCs as they travel throughout oxygenated and deoxygenated circulation cumulatively damage the membrane, leading to the formation and existence of irreversibly sickled cells, which can make up as much as 30% of the blood in the arterial system and ultimately change bulk flow properties in unexpected ways [21, 22]. Continuous damage to RBCs eventually leads to lysing as the cell life span is reduced from a normal 120 to 20 days [23]. This reduction in RBC numbers are associated with the anemia commonly associated with SCA. Individuals with sickle trait are generally regarded as having a benign form of the disease [24]. This is because HbA is also produced which dilutes the total amount of HbS in the cell and reduces the chance of hemoglobin polymerization. There have been reports however of complications for individuals with SCT from lack of oxygen, produced either from over exhaustion [25] or a high-altitude environment [26].

One of the more characterized complications in SCA is impaired blood flow culminating in occlusive events occurring throughout the vascular tree, from the relatively low-shear post-capillary venules to the relatively high-shear large cerebral arteries [4, 13, 27-29]. The major causes of altered blood flow are 1) altered sickle cell blood rheology, 2)

increased inflammation, and 3) cellular adhesion [13]. It is important to note however that there is a wide diversity in phenotypes among individuals as some people experience an almost benign disease [13]. The mechanism for heterogeneity in phenotypes are wildly unknown, but finding and understanding potential clinical predictors for severe prognoses may pave the way for improved patient management and development of new treatments [30].

Amongst the types of vaso-occlusions which occur in SCA, sickle cell crisis is one of the most well characterized. Red blood cells are highly deformable allowing cells to travel through the capillaries, which can have a diameter smaller than the size of a single RBC. For individuals without SCA this causes no issue, however in those with SCA the increased rigidity of RBCs created by the polymerization of hemoglobin can prevent the cell from deforming and cause occlusions in the micro-circulation. These blockages can cause severe debilitating pain, necrosis, and organ damage [14, 31, 32].

2.2 Strokes in Sickle Cell Anemia

Though a majority of vaso-occlusive problems occur in the capillaries and post-capillary venules, SCA can also affect the large arteries. One of the most debilitating complications associated with SCA is the development of strokes in children. By the age of 18, 11% of adolescents will have an overt ischemic stroke, affecting key motor functions, with those between the age of 2-8 at greatest risk [3, 33]. Additionally, up to 37% of children by 14 years of age will have a silent stroke, which can go undetected for years but impair mental function and cognitive abilities [3, 34]. Furthermore, after the first stroke, the risk of recurrent strokes is elevated significantly by as much as 50-90% [35, 36].

The Stroke Prevention Trial in Sickle Cell Anemia (STOP), led by Robert Adams and others in the late 90s has paved the way for diagnosing and treating individuals at risk for ischemic stroke [37-39]. Using transcranial Doppler ultrasound (TCD), they showed that elevated cerebral blood velocities were correlated to stroke risk. Specifically, when the time-average maximum-mean velocity (TAMMV) exceeded 200 cm/s in either the internal carotid artery (ICA), middle cerebral artery (MCA), or anterior cerebral artery (ACA), the measurement is diagnosed as abnormal. If left untreated, individuals above this 200 cm/s threshold, have a greater than 60% chance of developing a stroke within 3 years of diagnosis [1, 40, 41]. A conditional range between 170-199 cm/s was also established as these patients had a high risk of converting to the abnormal velocity range [42].

Though 170 cm/s is considered the maximum cutoff for a normal velocity in individuals with SCA, this is still high in comparison to those without SCA. Normal ICA velocities in people without SCA range between 50-90 cm/s [37-39]. Elevated blood velocities not within the range associated to stroke risk can be related to anemia. Lack of oxygen caused by SCA requires increased blood flow to meet metabolic demands [37-39]. Increased cardiac output and reduction in cerebrovascular reserve have both been measured in individuals with SCA and hypothesized as mechanisms used to compensate for reduced blood oxygen availability.

While these mechanisms may be related to ischemic stroke risk in SCA, additional pathologies are found in those who have suffered from a stroke. Several studies have shown the presence of large stenoses, via angiograms in the cerebral arteries of individuals with elevated blood velocities [28, 43]. This is consistent with studies of blood flow in the vasculature, where increases in velocity at constant flow rates are due to localized stenoses

[44]. Furthermore, autopsies performed in the 1970s on individuals with SCA who died from ischemic strokes showed lesions associated with intimal hyperplasia in the luminal space. Characterized by infiltration and proliferation of smooth muscle cells, and fraying of the elastin lamina, these lesions show many similarities to atherosclerotic plaques, but are void of the lipid deposition know to occur with atherosclerosis [4, 5, 43, 45]. Therefore, similar mechanisms may exist between sickle-mediated strokes and atherosclerosis. The process of intimal hyperplasia in atherosclerosis has a wealth of literature [46-49], which can provide insight into the pathophysiology of sickle-mediated strokes [4, 5, 43, 50]. The timescale for atherosclerosis however is in the order of decades, whereas sickle cell-mediated strokes can occur within the first few years of life. Additionally, many cases have reported abnormal TCD readings, but with cerebral angiograms presenting no morphological anomalies [51]. Other mechanisms are required to explain the development of strokes in younger individuals with SCA.

While the chance of ischemic stroke decreases with age, the risk of stroke in individuals with SCA remains a persistent problem. By the third decade of life, risk of hemorrhagic stroke greatly increases [52]. The cause for this change in stroke type is not fully understood, however studies have shown low blood hemoglobin and high leukocyte numbers to be associated with hemorrhagic stroke [52]. Upon reaching the fourth decade of life, a switch occurs again and the risk of ischemic stroke begins to dominate in individuals with SCA [52].

2.3 Current Therapies for Stroke in Sickle Cell Anemia

In addition to developing criteria for diagnosing stroke risk the STOP trial also established the practice of monthly blood transfusions as the gold standard for preventing

strokes [35, 53]. Performed as either simple or exchange transfusions (erythrocytapheresis), long-term RBC transfusions are still the most popular prophylactic therapy used today. It is predicted that children who receive monthly blood transfusions have a 95% of remaining stroke free [1, 54]. Additionally, chronic transfusions have been shown to prevent stenoses and reduce cerebral blood velocities, an effect which is lost once transfusions are stopped[1, 15]. Monthly blood transfusions; however, carry significant risks. These included an increased chance on infection, alloimmunization, and iron overload, which are all life-threatening and prevent transfusions from being widely used in the general sickle population [27, 55].

Hydroxyurea was the first FDA (Food and Drug Administration) approved drug for treating SCA and was recently approved for pediatric treatment in 2017 [15]. It is a ribonuleoside diphosphate reductase inhibitor that was first used for treating various blood-related cancers. A beneficial effect of hydroxyurea is the production of fetal hemoglobin (HbF), a protein that is normally replaced by adult hemoglobin several months after birth [56]. Production of HbF reduces the concentration of HbS in red blood cells and prevents polymerization of sickle hemoglobin. Due to this benefit, treatment consisting of hydroxyurea has been shown to reduce the number of sickle crisis events [57]. In addition, the TWITCH (Stroke with Transfusions Changing to Hydroxyurea) trial found patients with abnormal TCD velocities who switched from chronic blood transfusions to hydroxyurea, were equally protected from strokes, but only in individuals without a pre-existing history of vasculopathy [58]. Hydroxyurea is not a cure for sickle cell anemia as damage can still occur in the brain and other organs [59]. In addition, there are adverse

effects such as rash, headaches, and nausea, as well as concerns about unknown effects of long-term treatment [15, 32, 60].

The only cure available for sickle cell anemia is allogenic hematopoietic stem cell or bone marrow transplantation (BMT) [61, 62]. By replacing hematopoietic stem cells with those from a non-sickle donor, an individual will be able to produce normal adult hemoglobin. Benefits of BMT are decreased SCA-associated mortality and prevention of organ damage [62]. Infection, graft-versus-host disease, and graft failure are all potential life-threatening risks of BMT [60, 61]. Age is another risk factor as the 5-year survivability of patients who underwent BMT decreases past the age of 16 [63]. Therefore, the procedure is only offered to those with severe cases of SCA, such as people with previous histories of strokes or recurrent sickle crises. Additionally, donor availability is an issue of BMT; in the US it is estimated that only 20% of patients with SCA have a matched sibling, matched unrelated donor, or preserved cord bloods available [60, 64].

Gene therapies are now seen as the future of curative therapies for sickle cell anemia [65]. Through manipulation of the human genome scientist are pursuing to remove and replace the HbS mutation. This avoids many of the donor issues with allogenic BMT as stem cells from the patient can be taken and modified [15, 60]. 2017 marks one of the first successful gene therapies for SCA, where an anti-sickling β-globin variant was transferred using a lentiviral vector into a 13-year-old boy [65]. Recent breakthroughs with CRISPR/Cas9 show promise, but it is unknown when such treatments will reach the larger population [66-68].

2.4 Hemodynamics in Cardiovascular Diseases

The endothelium is a monolayer of cells that line the inside of blood vessels and come in direct contact with blood. Comprised of endothelial cells this serves several important homeostatic functions, among which are its ability to act as a barrier, control vascular tone, respond to inflammatory cues, influence thrombosis, and modulate vascular remodeling [69]. Under normal conditions cellular interactions, chemical stimuli, and hemodynamic forces are all required for healthy endothelial function, however certain conditions can induce dysfunction. Endothelial dysfunction is a precursor of cardiovascular diseases, such as stroke, and considered a shift in the homeostasis of endothelial cells towards characteristics which are vasoconstrictive, prothrombotic, and/or proinflammatory [70].

Hemodynamic forces play a large role on vascular health, as the flow of blood continually applies mechanical stimulus on the endothelium. The role of hemodynamics on cardiovascular health was first theorized in atherosclerosis, where the pathology was observed to occurred preferentially at bifurcations in the vascular tree [7, 44, 71]. At these locations blood flow is disturbed, where the flow pattern is non-uniform and recirculates over time. This varies significantly from straight sections of the vasculature, where flow is ordered and unidirectional. Several hemodynamic forces act on endothelial cells, such as hydrostatic pressure and cyclic strain, but among these forces shear stress is most related to the movement of blood. Fluid shear stress is the tangential component of the frictional force created by the flow of a viscous substance such as blood. At the boundary of a wall, shear stress is defined as

$$\tau_w = \mu\dot{\gamma} \quad \text{(Equation 2.1)}$$

Where μ is the viscosity of the substance and γ is the shear rate. For Newtonian substances the viscosity is constant and independent of shear rate. Blood is non-Newtonian with viscosity increasing at low shear rates, this is especially important in the capillaries, where the small diameter of the vessel forces RBCs to come in close contact with each other [44]. In sickle cell anemia, polymerization of HbS in red blood cells increases the viscosity of blood, which can ultimately change the shear stress acting on endothelial cells [72-74].

In humans, along straight sections of the vascular, wall shear stress (WSS) ranges between 10-70 dynes/cm^2 in the arteries and 1-5 dynes/cm^2 in the veins. In the regions around bifurcations where atherosclerosis is known to occur, WSS will oscillate between ±5 dynes/cm^2 [44, 75]. Therefore, specific thresholds arise which inhibit or promote endothelial cell dysfunction [7-9, 76-78]. This was verified through *in vitro* experiments where the type of shear applied on endothelial cells would induce different phenotypes. For example, when high unidirectional shear is applied, endothelial cells will stretch and align along the direction of shear; whereas under low oscillatory shear endothelial cells have a random disorganized pattern and maintain a round appearance. The type of shear can also influence the expression of certain types of genes and proteins. One of the most well studied proteins is the upregulation of endothelial nitric oxide synthase (eNOS) under high shear, and down regulation under low shear [79-81]. eNOS synthesizes nitric oxide, which causes smooth muscles cells in the vessel wall to dilate and increase vascular tone. On the reverse side low shear stress can cause upregulation of endothelial cell adhesion molecules' VCAM-1, ICAM-1, E-selectin [49, 82, 83]. Under these conditions there is an increased chance for white blood cells to adhere to the endothelium, promoting a proinflammatory environment and endothelial cell dysfunction. This process however can

be reversed by applying high unidirectional shear. Low shear also causes the upregulation of certain proteases, such as cathepsin K and cathepsin L [84, 85]. These proteases degrade elastin and collagen, matrix proteins that comprise the blood vessel. When these proteins are degraded, smooth muscle cells in the vessel wall undergo a phenotypic change [48]. The cells will begin to migrate into any available space which can lead to intimal hyperplasia and narrowing of the lumen. Such as what is observed in stroke lesions of those with SCA.

2.5 Computational Fluid Dynamics in the Cardiovascular System

Computational fluid dynamics (CFD) is a powerful tool that can be used to simulate and approximate hemodynamic forces acting in the cardiovascular system [86, 87]. This is especially beneficial in areas where traditional medical devices are unable to make accurate measurements. CFD is a numerical approach that uses equations derived from physics to simulate fluid flow in a system of interest and approximate fluid properties. The basis for most CFD problems are the Navier-Stokes equations (Eq. 2.2), as defined below:

$$\rho \frac{D\boldsymbol{v}}{Dt} = \nabla P + \mu \nabla^2 \boldsymbol{v} + \rho \boldsymbol{g} \quad \text{(Equation 2.2)}$$

Where *v* is fluid velocity, P is pressure, ρ is density, and g is gravitational forces. and These equations describe the motion of fluids in a system though Newton's second law of fluid motion, and the different terms correspond to inertial, pressure, viscous, and external forces. Navier-Stokes is always solved with continuity equation (Eq. 2.3).

$$\frac{d\rho}{dt} + \nabla \cdot (\rho v) = 0 \quad \text{(Equation 2.3)}$$

The Naiver-Stokes equations represents conservation of momentum, while the continuity equation represents conservation of mass. By solving for these equations, it's possible to approximate the fluid velocity and pressure within as given system. However, transient problems and complex geometries require a numerical approach to solve these equations.

There are several different approaches to performing CFD. Among these methods, discretization approaches are some of the most often used. The first stage prior to the actual simulation are the completion of several pre-processing steps. This begins by defining the system or geometry of interest. Afterwards the region occupied by the fluid is discretized, or divided in smaller components, in a process known as establishing the mesh. Mesh size is critical as smaller sizes ensure higher accuracy, but at the cost of computational processing. Once the mesh has been created the system of equations, such as Navier-Stokes, are defined. The last step prior to the simulation is defining boundary conditions. This specifies properties of the fluid, behavior of the fluid at specific boundaries or walls, and initial conditions if the problem is transient. After all these steps are complete the simulation is performed and solved in an iterative manner. To improve the computational efficiency, CFD-based problems are often run using parallel computing, which divides the system into several smaller components that can be performed simultaneously. Once the simulation is complete the resulting solution can be visualized and examined for further analysis using a post-processing program.

Blood is a mixture of cells, proteins, and other constituents that make up plasma, and when examined these components causes blood to act like a non-Newtonian shear thinning fluid. However, in most arteries shear rates exceed 10 Hz, and blood behaves similarly to Newtonian substances [44, 73, 88]. In this region of the cardiovascular system, whole blood has an approximate viscosity of 4 cP. and density of 1.060 g/cm^3 [44, 88, 89]. In SCA, the individual RBCs are more viscous, but overall hematocrit of whole blood is lower due to lysing of the cells. Therefore, in high shear regions viscosity is similar between sickle and non-sickle individuals [72, 73].

At the walls of the artery a no-slip condition is often applied, which assumes velocity of the fluid at the boundary is equal to the velocity of the boundary itself. When simulating blood flow in the cardiovascular system, the vessel walls are often assumed to be rigid and velocity at the wall is zero. Realistically, vessels are often moving and diameter

changes throughout the cardiac cycle. This however adds increased complexity to the system of equations. In most regions of the vasculature, deformation of the wall does not significantly affect the velocity field, thus justifying the rigid wall assumption [90].

The heart pumps blood in a cyclic pattern, therefore blood is often simulated using a periodic function across several cardiac cycles. Inlets and outlets are the cross-sections at which the blood enters and exits the system. For inlets a velocity or pressure waveform measured from a patient is usually applied. Physiological waveforms are also desirable at outlets, but there are often difficulties obtaining accurate measurements from smaller downstream vessels. The Windkessel model can be used to overcome these problems [44, 91, 92]. Based on principals from electricity, a relationship between pressure (P) and blood flow ($\dot{V}$) can be established for the entire cardiovascular system using a mechanical circuit (Fig. 2.1 & Eq. 2.4).

$$\left(1 + \frac{R_1}{R_2}\right) V(\dot{t}) + CR_1 \frac{d\dot{V}(t)}{dt} = \frac{P(t)}{R_2} + C \frac{dP(t)}{dt} \quad \text{(Equation 2.4)}$$

As blood is pumped from the heart during systole, the downstream vessels act like a capacitor (C) storing the blood due to its elastic properties. In parallel to this capacitor a resistive element (R_2) is placed to represent the loss of energy as blood travels though the arterioles and smaller vessels of the cardiovascular. Often a third element (R_1) is added to this model to represent the impedance of blood flow due to the characteristic resistance of the vessel it is traveling though.

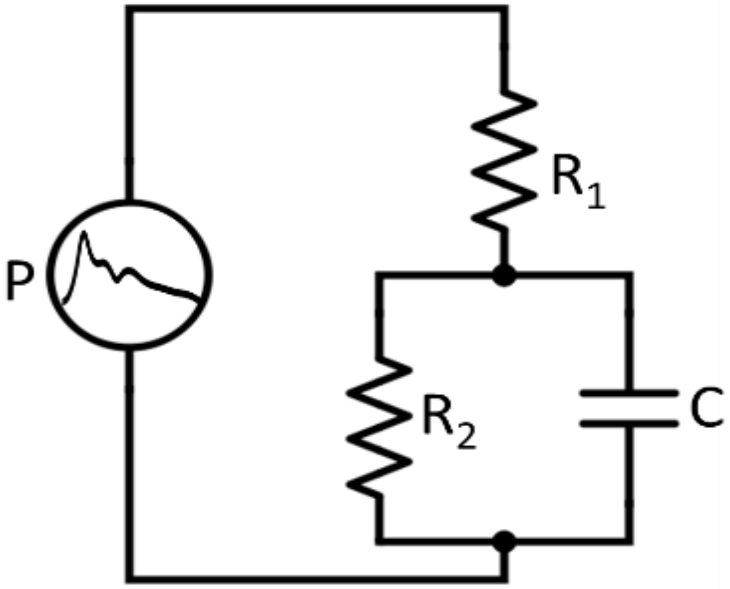

Figure 2.1: Three-element Windkessel model.
The Windkessel is used to relate pressure and flowrate in the cardiovasculature using a system of resistances and compliances. R_1 represents the characteristic vessel resistance, R_2 represents peripheral vessel resistance, and C is peripheral vessel compliance.

After the simulation is completed additionally hemodynamic parameters can be calculated through post-processing of the velocity solution. Wall shear stress can be derived by using the following equation

$$WSS = \overrightarrow{\boldsymbol{\tau_w}} = \boldsymbol{\tau} \cdot \boldsymbol{n} - (\boldsymbol{\tau} \cdot \boldsymbol{n})\boldsymbol{n} \text{ (Equation 2.5)}$$

where $\boldsymbol{n}$ is the outward unit vector normal to the wall, and shear ($\boldsymbol{\tau}$) is defined as

$$\boldsymbol{\tau} = \mu(\nabla \boldsymbol{v} + \nabla \boldsymbol{v}^T) \text{ (Equation 2.6)}$$

Though wall shear stress is important to vascular health two additional parameters time-average wall shear stress (TAWSS) (Eq. 2.7) and oscillatory shear index (OSI) (Eq. 2.8) can be derived to describe the wall shear stress throughout the entire cardiac cycle [7, 8]. Defined as follows

$$TAWSS = \frac{1}{T}\int_0^T \overrightarrow{\boldsymbol{\tau_w}} dt \text{ (Equation 2.7)}$$

$$OSI = 0.5\left(1 - \frac{\left|\int_0^T \overrightarrow{\boldsymbol{\tau_w}} dt\right|}{\int_0^T \left|\overrightarrow{\boldsymbol{\tau_w}}\right| dt}\right) \text{ (Equation 2.8)}$$

where T is the length of the cardiac cycle. Both play an important role for vascular health. In one study performed by, Cheng et al. the effect of in vivo alterations of shear stress showed TAWSS and OSI are both essential conditions for development of atherosclerosis in apoE-deficient mice [13].

CHAPTER 3 SICKLE CELL ANEMIA AND PEDIATRIC STROKES: COMPUTATIONAL FLUID DYNAMICS ANALYSIS IN THE MIDDLE CEREBRAL ARTERY

3.1 Introduction

Sickle cell anemia (SCA) is one of the most common blood disorders in the world with 300,000 babies born each year [11]; amongst them 11% of children with this genetic disease will have a major stroke by the age of 16 years; and up to 37% will have a silent stroke impairing mental function and cognitive abilities by age 14 [3, 34]. After the first stroke, the risk of recurrent strokes is elevated significantly to 50-90% [35, 36]. During the major clinical trial STOP, Transcranial Doppler ultrasound was used to measure the highest time averaged mean blood flow velocity in the internal carotid artery (ICA), middle cerebral artery (MCA) or the anterior cerebral artery (ACA). The study concluded that children had greater than a 60% chance of developing a stroke when time averaged maximum-mean velocities (TAMMV) were greater than 200 cm/s, deemed the abnormal range, but chronic transfusions could significantly reduce the risk of primary stroke [36, 93]. Patients in the conditional range from 170-199 cm/s are at increased risk as well and have high probability of conversion to the abnormal range [42]. The mechanisms that cause sickle cell-mediated strokes are still not fully understood but altered hemodynamics may be responsible as indicated by the elevated velocities. Deoxygenation causes a conformational change in the hemoglobin protein that exposes the mutant valine on the surface of the β-globin subunit that drives polymerization into stiff hemoglobin fibers that

deform the red blood cell (RBC) membrane into the sickle shape. The repetitive polymerization and melting of hemoglobin fibers in the RBCs as they travel throughout oxygenated and deoxygenated circulation cumulatively damage the membrane, increasing its viscosity and RBC density, which can ultimately change bulk flow properties in unexpected ways. RBC density, viscosity, and stiffness increase with each sickling, increasing viscosity of sickle cell blood by as much as 3-7 times greater than non-sickle blood at an equivalent hematocrit [17-20]. However, people with sickle cell anemia have a reduced hematocrit of only ~25% compared to 45% of those without the genetic disease.

The interplay between the altered rheological properties induced by the sickle cells and the hemodynamics is not trivial and needs to be properly modeled with mathematical and numerical tools. While the change in shape and mechanical properties of the red cells alters the apparent viscosity, which should slow down the blood, the velocity in children with SCA is elevated. It is also worth pointing out that while it is expected to find elevated centerline velocities through stenotic regions of arteries, abnormalities may not be detected by MRAs although an elevated velocity is measured by TCD [51]. The objective of this study is to provide preliminary insight into these inconsistencies by determining *in silico* scenarios by which pathological, elevated blood velocities can occur in the MCA, ICA, and ACA of children with sickle cell anemia. Utilizing computational fluid dynamics (CFD), blood flow was simulated in both two- and three-dimensional computational reconstructions rendered from actual patient angiograms, then manipulated to determine virtual stenotic scenarios in the cerebral arteries capable of reproducing the elevated velocities measured by TCD to locate regions where stenosis may not yet be detected by magnetic resonance angiography. Further, these scenarios will provide key insight into

hemodynamics that are counterintuitive to the general assumptions made about flow in tubes and at branches. Reconstructions from patients with and without sickle cell anemia were then compared for their hemodynamic properties to investigate inherent differences in geometry or anatomy that could be key to altering hemodynamics. This is the first work toward a progressively more accurate assessment of the rheological properties of patients affected by sickle cell anemia by using computational tools and their consequences on the hemodynamics.

3.2 Methods

3.2.1 System of Equations

The finite element method was implemented to simulate blood flow in the cerebral arteries. The commercial package, *Comsol 4.4*, and an open-source software, *LifeV* (www.lifev.org) were used to perform simulations in both two and three dimensions, respectively. The governing equations used for the study consisted of classical Navier-Stokes equations for incompressible fluids (Eq. 3.1) and conservation principles of mass and momentum (Eq. 3.2). At this first level of investigation, we assumed blood to be an incompressible Newtonian fluid, such that viscous effects are explained by a constant viscosity μ multiplied by shear stress. By denoting with $\boldsymbol{v}$ the velocity, P the pressure, ρ the (constant) density, the equations read

$$\rho \frac{D\boldsymbol{v}}{Dt} = \nabla P + \mu \nabla^2 \boldsymbol{v} \text{ (Equation 3.1)}$$

$$\nabla \cdot v = 0 \text{ (Equation 3.2)}$$

where D/Dt denotes the material or Lagrange derivative, and ∇^2 is the Laplace operator.

These equations were assumed to hold in the vascular lumen and delimited by the vascular walls and inflow/outflow sections. On the walls we postulate rigid displacement

and consequently assume a null velocity based on the no-slip condition. A zero-velocity and pressure were prescribed as the initial conditions for transient problems. However, since these conditions do not match the prescribed boundary conditions, this inconsistency may generate numerical instabilities. To avoid these spurious effects, before the actual simulation a “pre-load” phase is calculated, such that the initial conditions are gradually made consistent with the boundary data, by solving the Navier-Stokes equations for a certain number of fictitious time steps. At the end of this stage, the velocity and pressure fields at the beginning of the cardiac cycle are perfectly consistent with the prescribed boundary data.

3.2.2 Characteristics and properties of two-dimensional simulations in COMSOL

Arterial segments containing the distal internal carotid artery (ICA), the anterior cerebral artery (ACA), the middle cerebral artery (MCA), and segments from the first bifurcation of the MCA, known as the M2, were used for models in blood flow simulations (Fig. 3.1). These segments were chosen because of their diagnostic importance in determining stroke risk in sickle cell anemia by TCD [38, 94, 95]. The two-dimensional model was created from a representation previously published of a 71-year-old female subject (P0) [96], and used to perturb fluid properties, initial conditions, and stenoses placements (Fig. 3.1A). The representative figure was scanned into SolidWorks (Vélizy-Villacoublay, France), where an outline of the model was produced and scaled to the appropriate size. A velocity waveform was prescribed at the inflow as illustrated in Fig. 3-1B. These conditions are prescribed by postulating an arbitrary parabolic velocity profile fitted to the flow rate. To mitigate the impact of this arbitrary choice on the results, as common practice a flow extension was added upstream of the ICA [97, 98]. This fictitious

section has a length 10 times the diameter of ICA inlet. The mesh for the 2D simulations was created in Comsol (Stockholm, Sweden) using the program's in-house mesh generator, where a mesh containing ~21,000 elements was applied to the geometry.

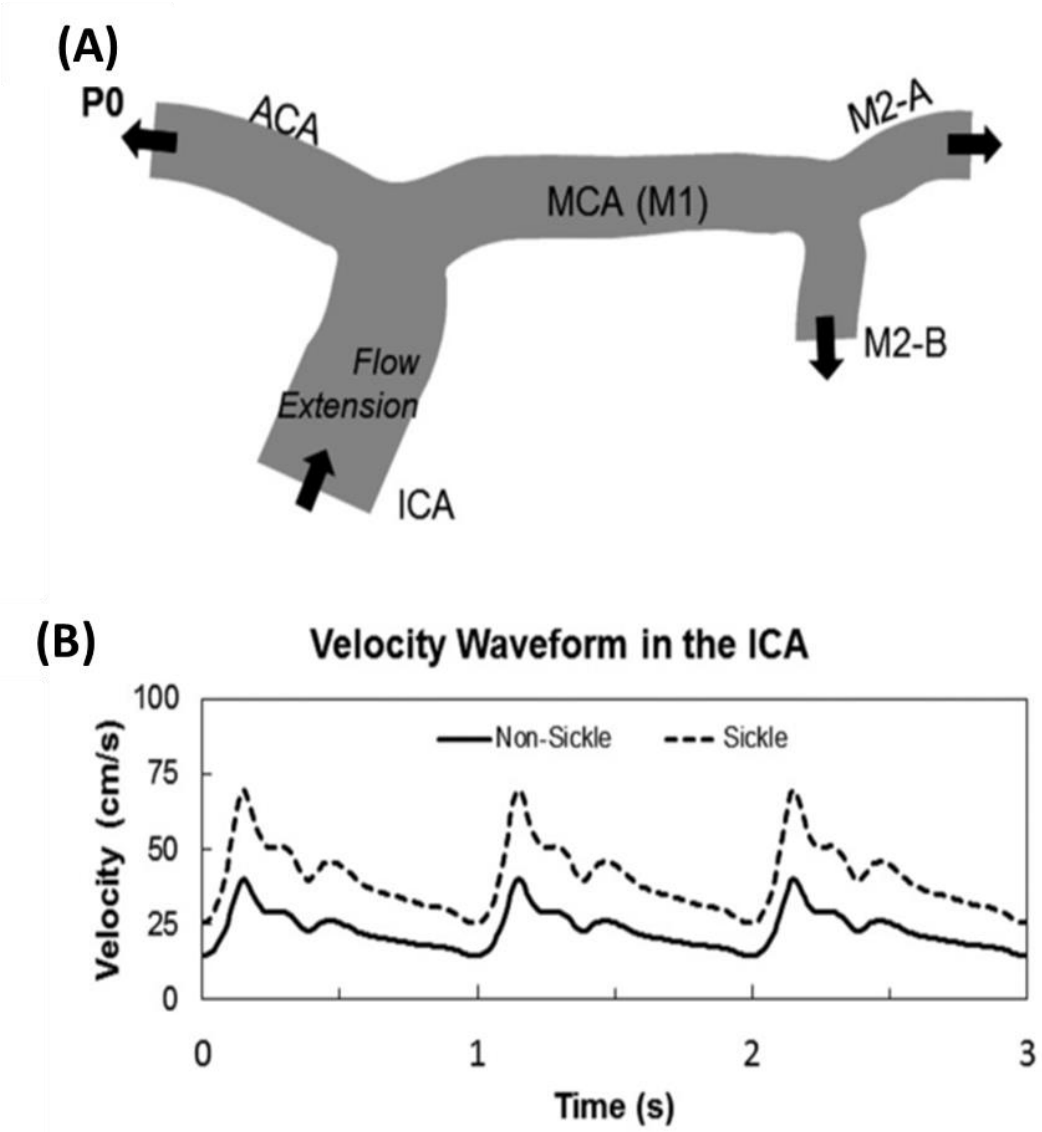

Figure 3.1: Outline of two-dimensional cerebral artery model.
(A) A 2D representation of the MCA from a 71-year-old female subject was used for the two-dimensional simulation. **(B)** Comparison velocity profiles over three cardiac cycles found in the ICA of SS and AA individuals. The elevated velocity profile caused by anemia in SCA was used as the inlet boundary condition for all simulations.

Simulated fluid properties were that of healthy blood (μ = 3 cP, and ρ = 1060 kg/m^3) [44, 88, 89]. Flow extensions at the ICA-inlet were added to the original geometry to guarantee velocity profiles entering the ICA during the simulation were laminar and parabolic. The outlet arteries (ACA, M2-A, and M2-B) had an open boundary, and *Comsol*'s suppression algorithm was used to prevent backflow at the outlets, preventing the need for flow extensions at these arteries.

Individuals with HbAA blood (RBC containing only normal hemoglobin) have a maximum-mean velocity of 40 cm/s in the ICA, based on values found in literature [99, 100], therefore to simulate conditions in a person with HbSS blood (RBC containing only sickle hemoglobin), this maximum-mean velocity at the inlet was changed to 70 cm/s. This was based on values found clinically and represents the elevated blood velocities caused by anemia in an individual with SCA [38, 101]. After the maximum-mean velocity of the profile was increased, the rest of the waveform was scaled accordingly. These two velocity waveforms over three cardiac cycles are shown in Figure 3.1B.

Simulations were run for three consecutive heart beats (1 Hz frequency) with a time step of 0.1 s. Post-processing of data for the 2D simulations were completed in Comsol. The maximum velocity during systole was determined across the entire model for all simulations, and the time-averaged velocity was calculated across cross-sectional slices at the proximal and distal ends of the MCA. Shear stress was calculated based on the following equation.

$$\boldsymbol{\tau} = \mu(\nabla \boldsymbol{v} + \nabla \boldsymbol{v}^T) \quad \text{(Equation 3.3)}$$

On the boundaries (walls), it is well known that the wall shear stress (WSS) has a clinical significance [44, 75]. The latter is defined as the tangential projection of the normal component of the shear stress,

$$WSS = \overrightarrow{\boldsymbol{\tau_w}} = \boldsymbol{\tau} \cdot \boldsymbol{n} - (\boldsymbol{\tau} \cdot \boldsymbol{n})\boldsymbol{n}$$ (Equation 3.4)

where $\boldsymbol{n}$ is the outward unit vector normal to the wall.

Table 3.1 Parameter values used in finite element model

Parameter	Nomenclature	Value
ρ	Density	1060 kg/m^3
v_{entr}	Average inlet velocity	70 cm/s
dt	Time Step	0.01s
T	Total Time	3s
v_{int}	Initial Velocity	0 cm/s
p_{int}	Initial Pressure	0 dynes/cm^2

3.2.3 Non-Newtonian Model for Viscosity

Blood is a heterogeneous mixture composed of plasma, red blood cells, white blood cells, and platelets. This heterogeneous makeup attributes blood with the non-Newtonian properties of a shear thinning fluid that has its viscosity decrease when subjected to shear. In healthy individuals the red blood cell (RBC) volume or hematocrit accounts for 45% of the total blood volume [102]. The other main constituent of whole blood is plasma, which consists mostly of water, thus RBCs are the main contributor to blood's non-Newtonian property. Blood rheology is affected by red cells in two ways: rouleaux formation at low shear rates and inelastic collisions at high shear rates [103]. In the large arteries, such as the MCA, the inelastic collisions will overtake rouleaux formation, as shear rates exceed a 100 Hz [104, 105]. These non-Newtonian properties become especially important in the case of sickle cell where deoxygenation of the red blood cell leads to a conformational change in the mutated hemoglobin protein. This leads to polymerization of the β-globin into stiff hemoglobin fibers which deform the RBC membrane into the classical sickle shape [106]. Oxygenation of hemoglobin causes melting of the polymerized fibers, but the time required for this process can exceed the pulmonary circulation time, allowing for sickled RBCs to exist in the oxygenated systemic circulatory system [22, 106]. Additionally, repetitive polymerization and melting of hemoglobin fibers in the RBCs as they travel throughout oxygenated and deoxygenated circulation will cumulatively damage the cell membrane, producing an irreversibly sickled RBC with increased cell viscosity and density [21, 22]. This can ultimately change bulk flow properties in unexpected ways.

An important feature that is overlooked when studying the viscosity of blood in sickle cell is the anemia associated with the disease. The accumulated damage from the sickling process shortens the RBC lifespan to only 10 days, reducing the total hematocrit from 45% to only ~25% [72, 106, 107]. Many of the initial studies investigating viscosity in SCA assumed equivalent hematocrits for HbSS (homozygous sickle) and HbAA (homozygous non-sickle) blood types, which lead to increased viscosity findings for HbSS blood which were 3-7 times greater than HbAA blood [73, 108, 109]. While the change of the shape and mechanical properties of the red cells increases the apparent red blood cell viscosity, conversely the decrease in hematocrit also lowers the total blood viscosity. Due to this information it is critical to analyze both HbAA and HbSS blood as non-Newtonian fluids in comparison to a traditional Newtonian model. This was accomplished by comparing results of a Newtonian simulation to those of a non-Newtonian simulation for both HbSS and HbAA blood types in a 2D model. The Carreau model [110-112] is one method that can be used to approximate blood as a non-Newtonian fluid. Based on the following equation:

$$\mu(\dot{\gamma}) = \mu_{\infty} + (\mu_o + \mu_{\infty})[1 + (\lambda\dot{\gamma})^2]^{\frac{n-1}{2}} \text{ (Equation 3.5)}$$

Where μ_{∞} is the viscosity at a high shear rates, μ_o is the viscosity at low shear rates, is $\dot{\gamma}$ the shear rate, and λ and n are model parameters specific to the fluid. Two different types of Carreau models were used for the simulations: **(1)** A sickle (HbSS) model with a hematocrit of 25% extrapolated from Alexy et al. (2006) [72], and **(2)** A non-sickle (HbAA) model with a hematocrit of 45% model extrapolated from Chen et al. (1970) [73]
.

Table 3.2: Parameter Values used in non-Newtonian Carreau model

Parameters	HbSS Blood 25% Hct (Alexy et al. 2006)	HbAA Blood 45% Hct (Chen et al. 1970)
μ_∞ (cP)	3.431	3.966
μ_o (cP)	131.7	103.2
λ (s)	14.96	8.693
n	0.2647	0.1898
R^2	0.9997	0.9963

3.2.4 Characteristics and properties of three-dimensional simulations with VMTK, Netgen, and LifeV

Magnetic resonance angiograms (MRAs) were used to create 3D models of the cerebral arteries for each subject (Fig. 3.2). Amongst the subjects, one did not have SCA (P1) (Fig. 3.2A), while the remaining two (P2 and P3) were afflicted with the disease. No identifying information was provided, other than P2 had no history of stroke (Fig. 3.2B), while P3 had a previous overt stroke that affected the left side of the brain (Fig. 3.2C). Using the reconstructive software, Vascular Modeling Toolkit (VMTK) [113], 2D MRA slices taken in the coronal plane were stacked together to produce a 3D layered object [114]. Arterial branches were segmented out from the layered object and used to reconstruct the vascular tree. Once the vascular network was created, only the segments of interest were kept, and all the other vessels were removed. Re-meshing and smoothing algorithms from *VMTK* were applied to remove irregular artifacts created during the reconstructive process. The finished models include flow extensions at the inlets and outlets with lengths equal to 10 times the diameter. Flow extensions have a twofold purpose. As for the 2D case, at inflow boundaries they are intended to take the effect of the arbitrary velocity profile used to compensate the lack of patient specific data away from the region of interest, so to mitigate (or even discard) its impact on the solution; at the outflow they are not strictly needed, but they contribute to reduce the risks of backflows – the latter are well known to be a source of numerical instabilities at outlets [115]. The flow extensions reduce the impact of the arbitrary choice for the velocity profile in the region of interest [116]. The third subject, P3, contains a slightly longer ICA due to a stenosis featured in that arterial segment.

A mesh of approximately 75,000 elements was applied to each of the three-dimensional artery models. While for more accurate quantitative assessments, more refined meshes may be needed, at this preliminary qualitative stage of analysis, this mesh size is fine enough for a qualitative analysis of blood flow in view of comparative discussion. Meshes for the 3D simulations were first produced in the open-source software, *Netgen* [117] before being imported into *LifeV* [116]. The latter is an open source Object Oriented C++ Finite Element solver developed as a joint initiative of Department of Mathematics at EPFL, Lausanne CH, Department of Mathematics at Politecnico di Milano, Milan, IT and the Department of Mathematics and Computer Science at Emory University, Atlanta (GA) USA. The same SS velocity waveforms from 2D simulations were applied in 3D. Properties of Newtonian blood were assumed, and the artery walls were assumed to be rigid with a blood velocity of zero at the wall. In the 3D models, a lumped parameter (or 0D) model was used at each individual outlet to relate the outgoing artery velocity to the pressure of the outlet, known as the 3-element Windkessel Model [118]. While not the same as the boundary conditions used in the 2-D model, by applying this boundary equally to all outlets, the resistances on the system acted similarly to the open boundary condition. Simulations were run in parallel on a local Linux cluster. The open-source software Paraview was used for postprocessing and for computing maximum systolic velocity. Average velocity was taken across cross-sectional slices at the proximal and distal ends of the MCA, using a custom script developed in Matlab (Natick, Massachusetts, USA) (Appendix 1) that integrated individual velocity points across a surface. Lastly, wall shear stress (WSS) was calculated during diastole from the velocity profile using LifeV.

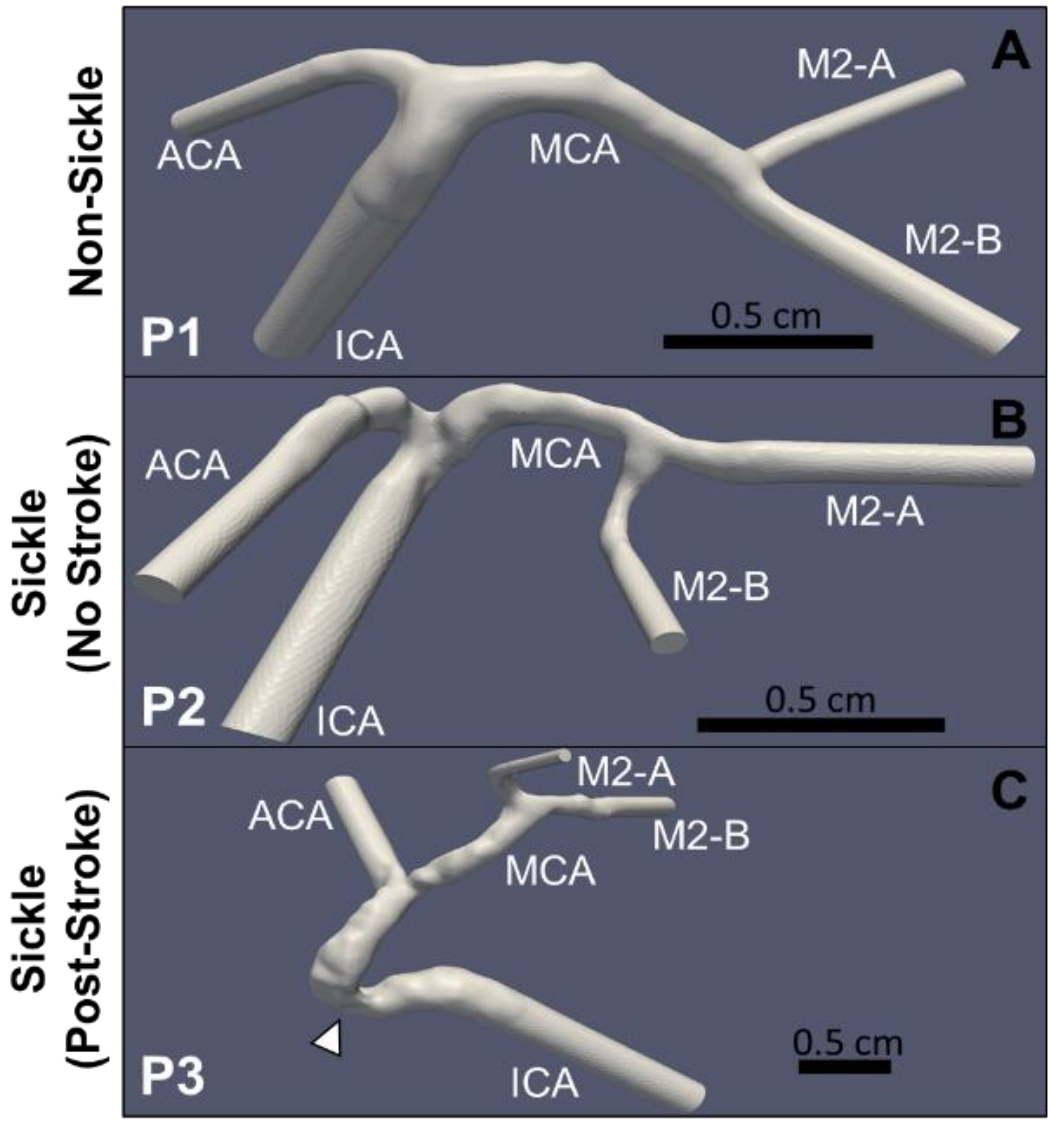

Figure 3.2: Reconstructed geometries of sickle and non-sickle cerebral arteries. Three-dimensional models were generated from MRAs of one non-sickle subject (P1) **(A)** and two sickle patients: one with no history of stroke (P2) **(B)**, and another post-stroke (P3). **(C)** The model of Patient 3's artery is extended due a stenosis in the ICA (arrowhead).

3.3 Results

3.3.1 Viscosity of SS and AA blood do not differ in the middle cerebral arteries

After data points for the non-sickle and sickle Carreau models were extrapolated from literature, parameters for the model were fitted using the curve fitting tool in Matlab (Table 3.2). Both the HbSS and HbAA blood types had excellent fits with R^2 value of 0.9997 and 0.9963, respectively. Two-dimensional simulations were performed comparing the non-Newtonian models to a Newtonian model of healthy blood ($\mu = 3$ cP, and $\rho = 1060$ kg/m^3) [119]. At high shear rates >10 Hz the viscosity for the Newtonian and all the non-Newtonian models were found to behave similarly (Fig. 3.3A) with viscosities ranging between 3 and 4 cP at these high shear rates. Shear rates in the MCA and large arteries are greater than 10 Hz, thus based on these models, blood would behave as a Newtonian fluid [105]. Compared to HbAA blood, HbSS blood has a higher viscosity for shear rates below 10 Hz, but a slightly lower viscosity for shear rates above 10 Hz (see magnified image in Fig. 3.3A), signifying that in the large arteries, SS blood has a lower viscosity than non-sickle blood. These differences, however, did not greatly impact the hemodynamics in the large arteries.

Figures 3.3B-D depict the viscosity for each of the different blood models during diastole. Viscosity in the Newtonian model (Fig. 3.3B) is consistent throughout the entire geometry as expected. For the non-Newtonian Carreau models, the viscosity is highest along the centerlines and the inner curvature of bifurcations. Viscosity for the non-Newtonian models range between 3 and 30 cP indicate shear rates in some regions were lower than 10 Hz. The viscosity of the SS and AA models are very similar with the SS model showing to have a slightly higher viscosity at bifurcations (Fig. 3.3C-D). Despite

the slight variations in viscosity between the models there are no distinguishable changes in the velocity profiles during systole (Fig. 3.3E-G), and the shear stress profiles during diastole (Fig. 3.3H-J), as compared to the non-Newtonian model. These suggest Newtonian AA blood can be used in a sickle model.

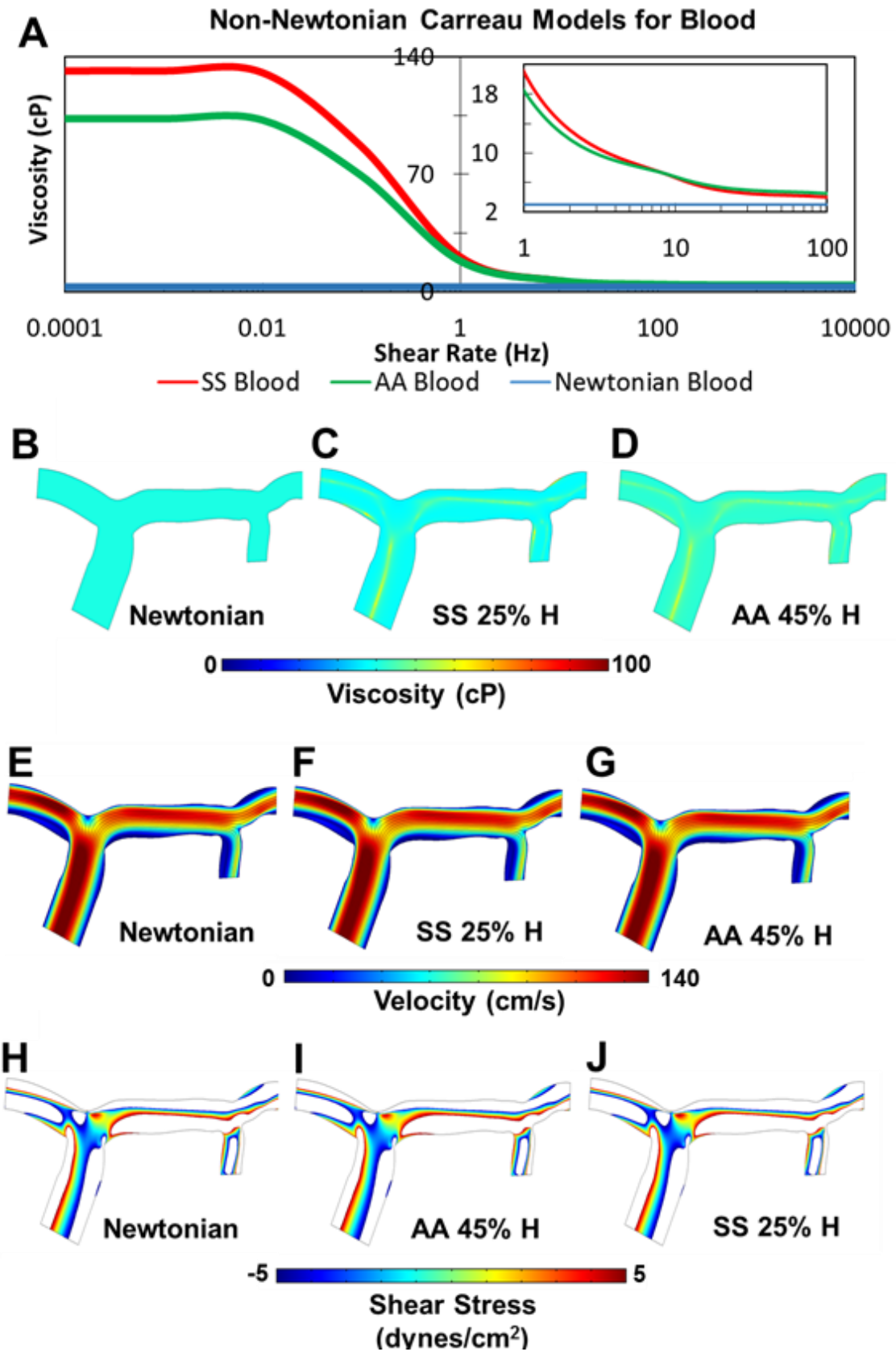
A
Non-Newtonian Carreau Models for Blood
Viscosity (cP)
140
70
0
18
10
2
1
10
100
0.0001
0.01
1
100
10000
Shear Rate (Hz)
SS Blood
AA Blood
Newtonian Blood
B
C
D
Newtonian
SS 25% H
AA 45% H
0
100
Viscosity (cP)
E
F
G
Newtonian
SS 25% H
AA 45% H
0
140
Velocity (cm/s)
H
I
J
Newtonian
AA 45% H
SS 25% H
-5
5
Shear Stress
(dynes/cm²)

Figure 3.3 Effects of Viscosity are Negligible in the Middle Cerebral Artery.
Whole blood was simulated as a non-Newtonian fluid through the Carreau model in the 2D simulations. **(A)** Two non-Newtonian models were utilized in the simulation: (1) a HbSS Blood Model with a hematocrit of 25%, and (2) a HbAA Blood Model with a hematocrit of 25% were compared to a Newtonian model of blood. **(B-D)** The viscosity of the fluid during diastole is displayed in the top right panel. **(B)** Viscosity in the Newtonian model is constant for the whole model. The viscosity in the non-Newtonian models are higher along the centerlines and inner curvature of bifurcations. Viscosity is highest in the sickle model **(C)** followed by the non-sickle model **(D)**. Between the Newtonian and non-Newtonian models, no noticeable differences are observed in the velocity profiles during systole **(E-G)**, nor in the shear stress profiles during diastole **(H-J)**.

3.3.2 MCA-elevated velocities indicative of stroke risk could not be generated in a two-dimensional computational fluid dynamic model.

First, we tested the hypothesis that an elevated velocity profile at the ICA-inlet caused by anemia would be sufficient to produce time-averaged mean velocities in the MCA greater than 200 cm/s, the magnitude that is indicative of stroke risk. Despite elevated inlet velocities approximately 40% greater than individuals with AA blood, the velocities in the MCA only reached a maximum speed of 90 cm/s during systole (Fig. 3.4A). Diastole values were of course lower, reaching only a maximum of 40 cm/s. Under these conditions, higher fluid velocities were observed in the ACA (100 cm/s) as compared to the MCA.

Since the elevated inlet blood velocity was insufficient to generate threshold velocity values indicative of stroke risk, shear stress was determined to identify regions of low or oscillatory shear stress. Such regions are known to cause endothelial cell responses that promote proteolytic mediated vascular remodeling leading to the formation of intimal hyperplasia that could possibly form stenoses in the artery [76, 77, 120]. Wall shear stress values were calculated from the velocity profiles, and areas of the artery wall exposed to shear stress in the range of ± 5 dynes/cm^2 are found to occur preferentially along the inner curvature of bifurcations (Fig. 3.4B). The length of the wall region exposed to this low, and in some cases oscillatory shear stress is shorter in systole than diastole.

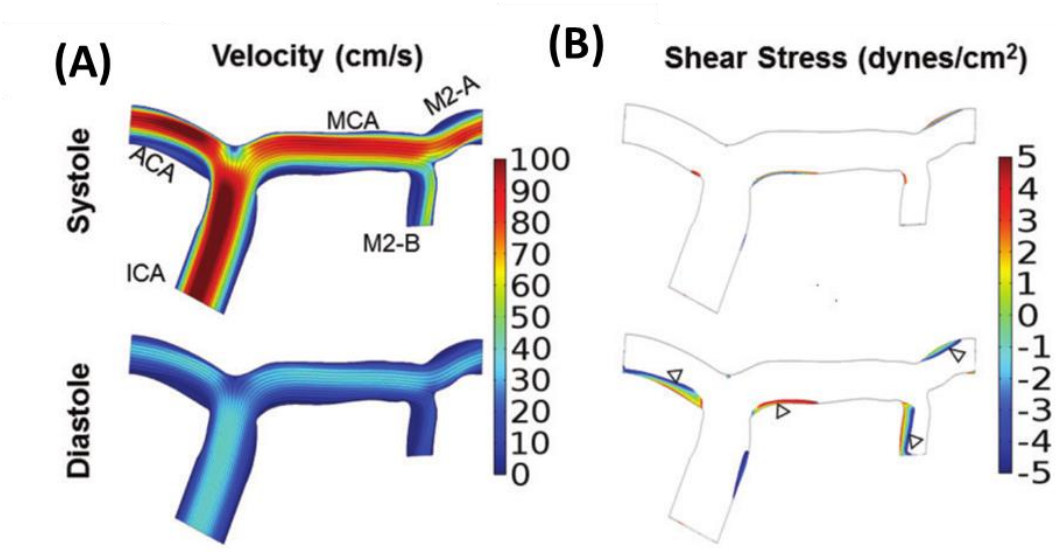

Figure 3.4 Elevated internal carotid artery velocities caused by sickle cell anemia does not generate velocities greater than 200 cm/s in the middle cerebral artery. Velocity and shear stress profiles were calculated for a 2-D arterial model with the TAMMV of the ICA inflow velocity set to those of a patient with SCA (70 cm/s). **(A)** Velocity profiles during systole and diastole. Velocity was highest in the ICA and ACA, and the maximum velocity in the MCA did not exceed 90 cm/s. **(B)** Regions of low wall shear stress during systole and diastole are depicted with a maximum threshold of ± 5 dynes/cm^2. The affected regions correlate to regions with low velocities **(A)** and include: the apex of the terminal end ICA bifurcation and inner curvature of bifurcations.

3.3.3 Effects of stenosis placement and size on velocities in the MCA

The original model was modified to simulate the development of intimal hyperplasia and vascular lesions that would occur at sites exposed to low wall shear stress, and these regions were informed by the sites of low wall shear stress from the previous model (Fig 3.4B). To test the hypothesis that stenoses formed by such lesions could produce an elevated time-average maximum-mean velocity greater than 200 cm/s, vascular lesions were placed one at a time, in either the ACA, the proximal MCA, the M2-A, or the M2-B. This was to determine the percent stenosis necessary to generate elevated velocities. Simulations were performed over a range of stenosis magnitudes: 25% (green), 50% (orange), or 75% (red) of the artery diameter (Fig. 3.5A).

The mean velocity was calculated at the proximal and distal ends of the MCA, and the effects of stenosis magnitude and location on mean blood velocity in the proximal and distal MCA were determined. As the magnitude of a stenosis in the MCA increased from 0% to 75% the artery diameter the mean velocity also increased in the proximal MCA, reaching a maximum-mean velocity of about 90 cm/s (Fig. 3.5B). A similar effect was observed when a stenosis was placed in the ACA; however, the velocity at the proximal MCA only increased from stenoses sizes ranging between 50% and 75%, and 25% lesions having little to no effect on blood velocities at proximal MCA site (Fig. 3.5C). Stenoses in both the M2-A and M2-B had minimal effect on velocity in the proximal MCA despite large stenoses that filled 75% of the artery diameter (Fig. 3.5D&E).

Stenosis placement in the ACA and the downstream arteries of the MCA, the M2-A and M2-B had similar effects on velocity calculated at the distal MCA site (Fig 3.5G-I), but when the stenosis was placed at the entrance to the MCA, the results were significantly

different (Fig. 3.5F). There was a decrease in mean velocity at the distal MCA site from 60 cm/s to 25 cm/s which was opposite of what occurs to velocities measured at the proximal MCA location. Taken together, the data could be plotted as percent change in the maximum-mean velocity to distinguish differences between velocities at the proximal or distal end of the MCA (Fig. 3.5J-M). Only for stenoses placed at the entrance of the MCA, can a stark difference in maximum-mean velocities be generated along the length of the MCA (Fig. 3.5J). The percent change in velocity increased as a function of percent stenosis for velocities measured at proximal MCA, but conversely decreased with percent stenosis at the distal end. This has important implications for determining patient stroke risk. It could be, that when averaging velocities measured by TCD over the length of the entire MCA, an incorrect and significantly lower velocity reading might be obtained, misleading clinicians to thinking the patient is safe, although a large stenosis may be present, and the patient is at high risk. Despite this interesting disparity for proximal MCA lesions, the mean MCA velocity never exceeded a 100 cm/s, regardless of lesion size and location.

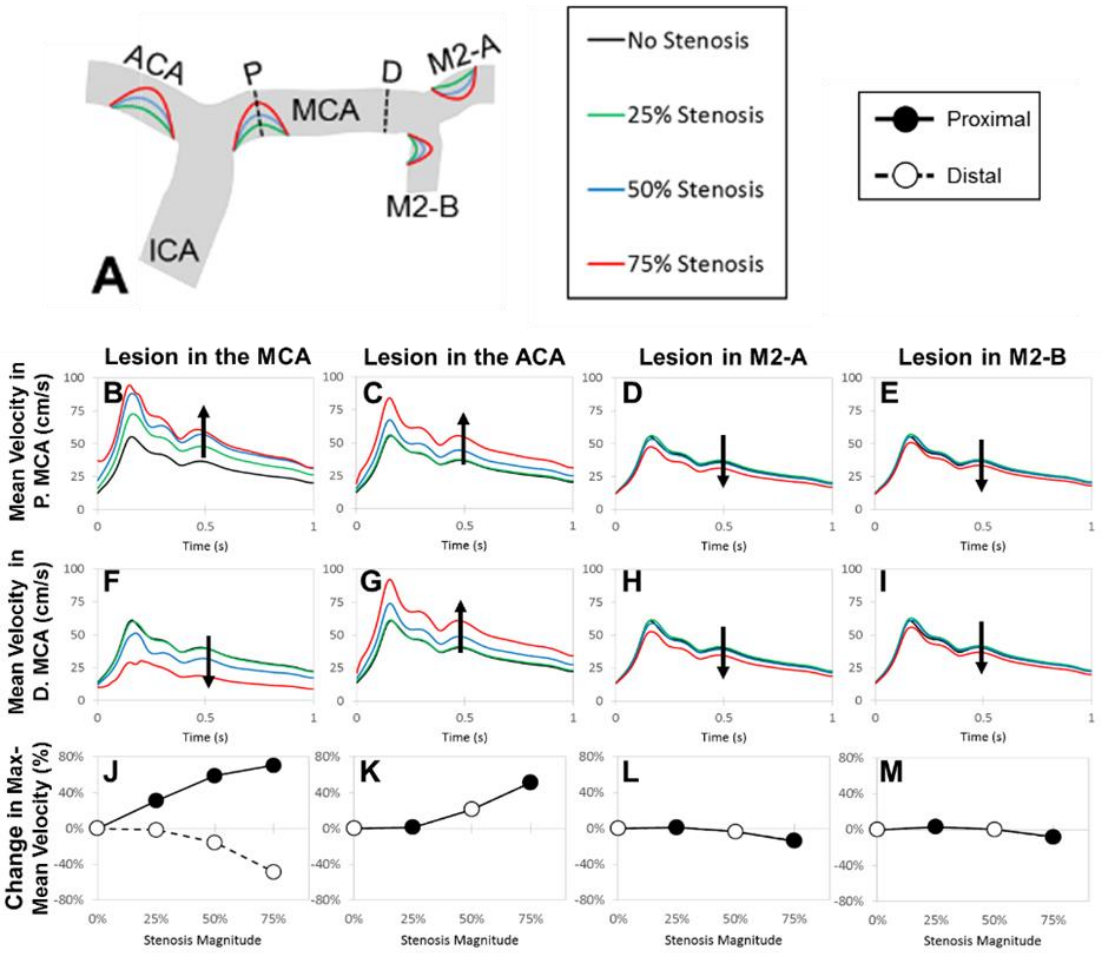

Figure 3.5 A lesion at the entrance of the middle cerebral artery produces the largest difference in the proximal and distal velocities.

(A) A lesion at the entrance of the middle cerebral artery produces the largest difference in the proximal and distal velocities. Lesions of increasing size from 25% -75% of the artery diameter were placed in entrance of the MCA, ACA, MCA-1, and MCA-2 (areas affected by low WSS) in order to produce stenotic lesions. Dotted lines represent slices where the mean velocity was measured in the proximal (top panel) and distal (middle panel) MCA. Mean velocity in the proximal MCA increased with lesion magnitude when narrowing occurred at the entrance of the MCA **(B)** and ACA **(C)**. **(D, E)** Lesions in M2-A and M2-B had a negligible effect on velocity despite a lesion magnitude of 75%. **(F)** In the distal end of the MCA, the mean velocity decreased with increasing MCA stenosis. Increasing the magnitude of the ACA lesion led to an increased velocity in the distal MCA **(G)**, and stenoses in the M2-A and M2-B did not affect velocity **(H, I)**. In the bottom panel, percent change in the maximum-mean velocity was calculated in respect to lesion magnitude and location. **(J)** A lesion in the MCA entrance produced the greatest difference in percent change, increasing and decreasing in the proximal and distal MCA velocity, respectively.

(K- M) Lesions in the ACA, MCA-1, and MCA-2 entrances have the same effect on both the proximal and distal velocities.

3.3.4 Mean Velocity is elevated in 3D patient-specific cerebral artery geometries of individuals with SCA

The inability to reach high pathological MCA velocities indicative of stroke risk in individuals with SCA in the 2D simulations maybe due to a lack of features only available in three dimensions; therefore, the importance of using full 3D models were investigated. Three subjects were compared to determine if anatomical differences between sickle and non-sickle individuals could influence the hemodynamic properties. ICA, ACA, and MCA vessels were reconstructed as described in the Methods sections from magnetic resonance angiograms (Fig. 3.2). Simulations were run with the same fluid properties and inlet values for all three subjects as in 2D.

A slice of the velocity streamlines during systole are shown for each subject: (P1) non-sickle cell; (P2) sickle patient with no history of stroke; and (P3) sickle cell patient that had a previous stroke (Fig. 3.6A-C). Maximum velocities differ for each of these reconstructed cerebral artery trees with P1, the non-sickle subject maximum reaching 170 cm/s in the ACA, up to 230 cm/s in the ICA of P3, the sickle patient post-stroke, and then the highest max value of 250 cm/s occurs in P2, the sickle patient no history of stroke (arrows, Fig. 3.6A-C). The velocity in the MCA remains consistent throughout the entire length of subject P1 (Fig. 3.6A). Velocity in the MCA of P2 gradually increased starting at 120 cm/s at the proximal side before reaching a maximum toward the distal end (Fig. 3.6B). The velocity profile slowed across the length of the MCA for P3 with the proximal end reaching a maximum value of approximately 180 cm/s, and gradually decreased to ~90

cm/s at the distal MCA. Subject P3 also had a localized increase in velocity occurring at the stenosis in the ICA (arrowhead Fig. 3.6C).

The mean velocities in the proximal and distal ends of the MCA were calculated for each subject. Subject P1 had the greatest consistency across the length of the MCA with the proximal end reaching a TAMMV of 72 cm/s and the distal end as high as 90 cm/s (Fig 3.6D). Subject P2 had the largest variance between both ends of the MCA. The proximal MCA was much lower reaching 66 cm/s, but the distal end had a maximum-mean velocity of 140 cm/s. A stenosis right at the bifurcation to the M2-B that may be the cause for this increase (Fig 3.6E). P3 fell in between the other subjects, for both velocity and maximum speed and variance in the MCA. This subject had a TAMMV of 92 cm/s and 61 cm/s for both the proximal and distal ends respectively (Fig 3.6F).

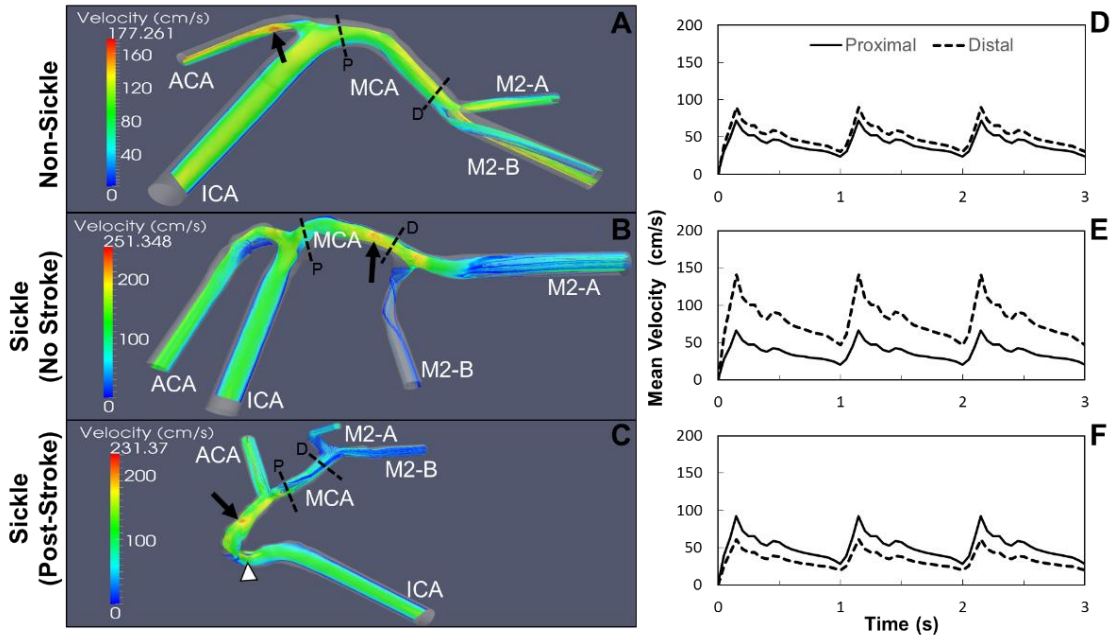

Figure 3.6: Velocity profiles in the middle cerebral are elevated in individuals with sickle cell anemia.

Slices of the velocity streamlines are depicted for each subject during systole. **(A)** The maximum velocity in the non-sickle patient (P1) is highest in the ACA (arrow), and the MCA presents a consistent profile that peaks at ~150 cm/s. **(B)** In the sickle patient with no stroke (P2), the velocity is highest in the MCA (arrow), increasing from the proximal to the distal end with a maximum speed of 251 cm/s. **[C]** The sickle subject with a previous history of stroke (P3) has the highest velocity occurring along the ICA prior to the bifurcation (arrow) and at the stenosis (arrowhead). The maximum velocity in the MCA reaches approximately 180 cm/s at the proximal end and decreases towards the distal MCA bifurcation. **(D)** The velocity in the MCA of P1 has the least variance with the velocity at the proximal and distal ends reaching 72 and 90 cm/s, respectively. **(E)** The velocity profile in the MCA of P2 has the largest variance amongst all the subjects with velocity increasing from the proximal end at 66 cm/s to the distal end at the 141 cm/s. **(F)** Subject P3 has its velocity in the MCA decrease from 92 cm/s at the proximal side to 61 cm/s at the distal end.

3.3.5 Areas of flow recirculation and low wall shear stress are more prevalent in reconstructed vessels of individuals with sickle cell anemia

Post-stenotic regions are subject to flow separation and flow reversal during the cardiac cycle [121], which also impose oscillatory shear stress on the endothelial cells lining the arteries that contributes to endothelial dysfunction and vascular remodeling [7-9]. With identification of elevated velocity regions in the cerebral arteries of these three subjects due to their individual geometry differences and not unique fluid inlet profiles, we next determined where regions of flow separation and low shear stress could influence biological remodeling. Velocity streamlines for each subject during systole is displayed in Fig 3.7 to display areas affected by disturbed flow with particular interest in regions of flow separation and recirculation. Magnified images of flow recirculation (circles) and vortices (square) are labeled to distinguish the differences (Fig 3.7). Subject P1, the individual without sickle cells disease, did not show regions of disturbed flow (Fig 3.7A); however, subjects with SCA, P2 and P3, both demonstrated fluid recirculation along multiple locations despite given the same inlet profile as P1. The sickle subject with no history of stroke (P2) had regions of recirculation along the inner curvature of bifurcations in the ACA, MCA and M2-A (Fig 3.7B). Subject P3, sickle post-stroke, had regions of flow recirculation at MCA along the inner curvature of the ICA bifurcation, and at the ICA stenosis (Fig 3.7C).

In addition to velocity, the wall shear stress (WSS) profiles were calculated during diastole. Areas of low shear stress (±5 dynes/cm^2) appeared near the recirculation zones, as expected (Fig 3.8). Front and back views of the model for subject P1 show areas of low shear stress to be located at the apex of the internal carotid bifurcation (Fig 8A). In both

subjects with SCA (P2 and P3), regions of low WSS were found in multiple locations that encompass a larger area as compared to the non-sickle subject. In the first individual with SCA (P2), regions of low WSS occurred along the inner curvature of the ICA and MCA bifurcations at the ACA, MCA, and M2-A (Fig 3.8B). Subject P3 had regions of low WSS along the ICA and MCA arterial segments (Fig 3.8C).

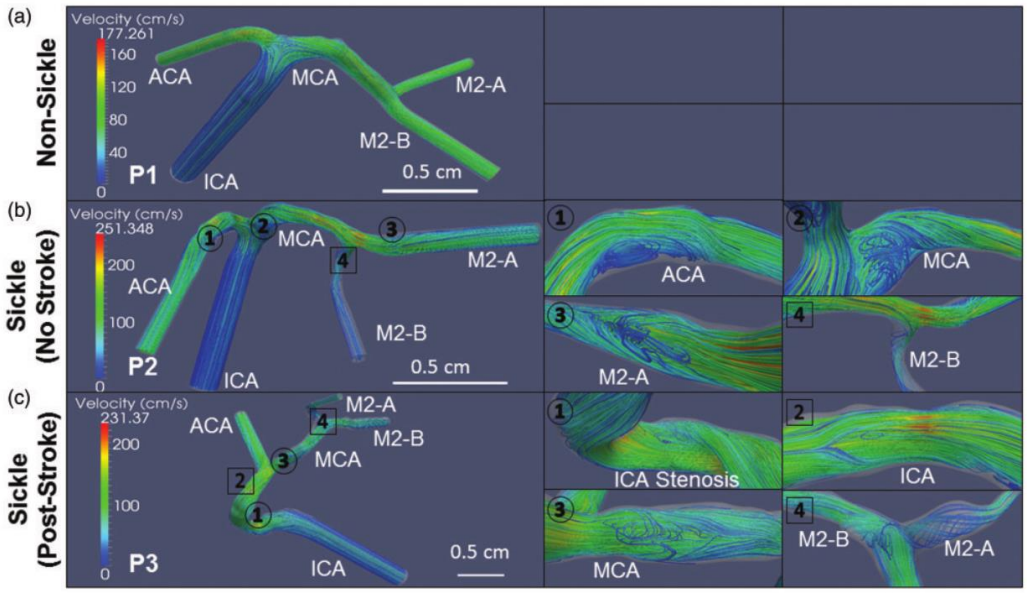

Figure 3.7: Recirculation of velocity streamlines are more prevalent in SCA

Patient-specific velocity streamlines during systole are depicted for the 3-D vascular models with recirculations *(circles)* and vortexes *(squares)* magnified for easier viewing. **(A)** The non-sickle subject's (P1) artery is completely void of any regions of fluid recirculation. **(B)** The first sickle subject (P2) has fluid recirculating at multiple locations near the inner curvature of bifurcations: specifically, at the ACA *(1)*, MCA *(2)*, and M2-A *(3)* arterial segments. A vortex is observed in the M2-B segment (4). **(C)** The second subject has recirculations occur at the ICA stenosis (1), and the MCA (3) following the ICA bifurcation. Vortexes are observed along the ICA (2) and at the MCA bifurcation (4).

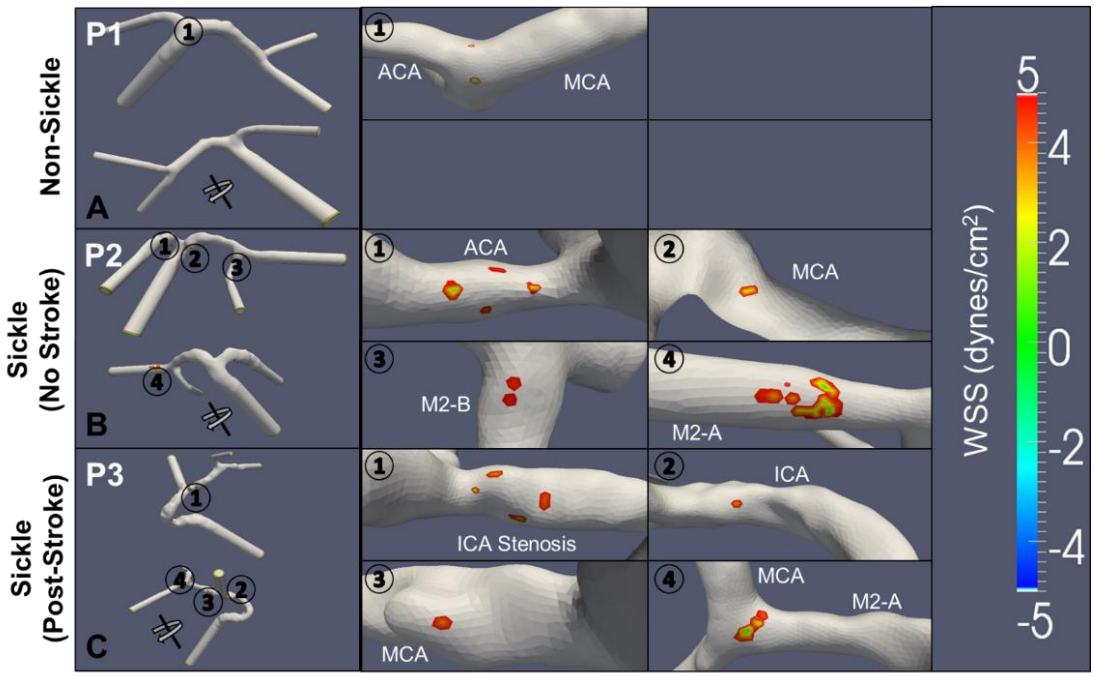

Figure 3.8: Areas of low shear stress are greater in sickle cell anemia arteries. Low WSS (±5 dynes/cm^2) during diastole were calculated from velocity profiles of non-sickle and sickle subjects. The locations of these low WSS *(circles)* are magnified in the images to the right for easier viewing. **(A)** In the non-sickle subject (P1), two spots of low stress areas of low shear stress occur at the apex of the internal carotid bifurcation *(1)*. **(B)** The sickle subject with no history of stroke (P2) has regions of low WSS occur along the inner curvature both bifurcations in the ACA *(1)*, MCA *(2)*, M2-B *(3)*, and M2-A *(4)*. **(C)** The second subject (P3) has multiple regions of low WSS. Two occur in the ICA, first at the stenosis *(1)*, and then preceding the ICA bifurcation *(2)*. Low shear areas also occur along the length of the MCA, one following the ICA bifurcation *(3)*, and the other at the apex of the MCA bifurcation *(4)*.

3.4 Discussion

The maximum velocities measured in the 3D simulations ranging between ~180 and 250 cm/s were much higher than in 2D, where only a max velocity of 100 cm/s was achieved. The 3D models therefore offered a better representation of the fluid profiles. While none of the mean velocities surpassed the 200 cm/s threshold value indicative of stroke risk, velocities in the simulations created from individuals with sickle cell anemia (P2 and P3) were higher than the reconstruction from an individual without SCA (P1). Therefore, despite the same boundary conditions across all simulations, the patient-specific geometries were sufficient to produce elevated velocities. This is an important result given that only a percentage of children with sickle cell anemia will have a major or silent stroke; the patient-specific differences responsible for this variability may include the individual anatomy.

The mean velocity in the distal MCA for both sickle subjects P2 and P3, were greater than the non-sickle subject P1, and greater changes in magnitudes of the velocities occurred at the proximal vs. distal ends of MCA (Fig 4). In the proximal MCA the mean velocity for subject P2 was greater than the mean velocity for P1; however, the sickle subject P3 was the lowest. This lower velocity in the sickle subject may be due to the presence of a small stenosis occurring in the distal end of the artery. Along the length of the MCA, subject P1 (non-sickle) had lower velocities, compared to SS subjects P2 and P3, (Fig. 3.6). This may be due to the surface texture of the endothelial surface in the arteries from sickle cell patients as they presented a “bumpy” appearance not seen in the non-sickle patient. These patient-specific geometries may be indicative of cellular or

pathophysiological phenomena that should be studied as causative phenomena for elevated velocities and stroke risk. Autopsies of patients who passed away from strokes indicated vascular remodeling characterized by fragmented elastic lamina, intimal hyperplasia, and luminal occlusion [50, 122, 123]. The luminal narrowing may cause the high blood velocities indicative of stroke risk, but it is unknown if it acts as the main contributing mechanism to the pathology. Additionally, an array of other pathological mechanisms including, increased red blood cell (RBC) and leukocyte adhesion, inflammation, and increased viscosity of individual red blood cells may be responsible for the bumpy texture and also provide biological mechanisms to be investigated as novel mechanisms that accumulate to cause sickle cell - mediated strokes [28, 103, 124, 125].

Although the TAMMV of the MCA did not exceed 200 cm/s in the 3D simulations, subjects with SCA when compared to the non-sickle patient were found to have higher streamline velocities. Additionally, both individuals with SCA had altered hemodynamic profiles, characterized by greater regions of flow reversal (Fig. 3.7) and large areas affected by low WSS (Fig. 3.8). These regions of low shear stress also correlated to zones of fluid recirculation, and occurred preferentially at the inner curvature of bifurcations or following stenoses, as seen in subject P3, corroborating findings from the atherosclerosis literature and previous studies [44, 75, 126]. Subjects with SCA were affected by low shear stresses over a larger surface area compared to the non-sickle patient, indicating that those individuals may be subject to shear stress mediated vascular remodeling. This result also illustrates the power of computational fluid dynamics as shear stress cannot be directly measured. Computational fluid dynamics could potentially be used to predict stroke risk by allowing clinicians to look for signs of altered blood flow, as these abnormal

hemodynamic forces may precede large stenosis formation that can cause high streamline velocities. Vascular remodeling may precede stroke formation, but it can sometimes be difficult to detect such small vascular changes with MRA. Unfortunately, radiological findings of large stenoses often coincide with stroke, as seen in subject P3, and preventative measures cannot reverse the damage. More simulations will need to be performed in the future to show statistical significance correlating disturbed flow profiles to stroke risk, but these current results show promise.

Higher MCA velocities could be achieved in silico by manipulating the ICA-inlet boundary condition, as the 70 cm/s maximum velocity chosen for this study was the lowest measured value acquired from a sickle patient in a cohort of six individuals. In general, sickle patients will have higher velocities as caused by anemia [37, 38]. Thus, the lower, but still elevated value of 70 cm/s, was deemed an appropriate input value for this study. An interesting phenomenon observed in the 2D stenotic simulations and in both 3D sickle models was the occurrence of a velocity gradient, which varied along the length of the MCA. This finding poses a question on the precision of TCD and the potential for misdiagnosis. Currently, TCD cannot perform the precise measurements taken from the simulations, as averages are taken across an area which can spans a width of 4 mm to 1.5 cm [127]. Measurements typically are made at 2-mm intervals, and thus only approximate values that extend over an entire arterial segment. This can potentially lead to incorrect diagnoses, as localized regions with high elevated velocities are in the same frame of measurement as regions with significantly lower velocities.

This study does have limitations. In particular, geometries are rigid, we do not have patient specific boundary conditions, and viscosity is assumed to be constant and tuned to

literature values. Results from non-Newtonian simulations suggest that in the large arteries, specifically in the MCA and its adjacent branches, Newtonian AA blood can be used in a sickle model. Utilizing this assumption in the sickle model greatly reduced the computational complexity and increase the speed of simulations. It is important to note that these assumptions can only be applied in the large arteries as the contribution of each individual RBC becomes increasingly more important in the smaller vessels. Known as the Fareus-Lindqvist effect the viscosity of healthy blood decreases with vessel dimeters ranging between 10 and 400 microns [128]. This is because erythrocytes will move to the center of the vessel leaving only plasma at the wall. Sickle cell anemia hinders this effect as the reduced elasticity and increased viscosity of each individual RBC prevents deformation of the cell through the microvasculature. If velocity through the microvasculature is reduce significantly because of these effects the shear rate in vessel will drop and cause rouleaux formation to occur [103]. The red blood cells will begin to aggregate at these low shear rates and block blood flow causing the ischemia that is often associated with sickle crisis.

After this qualitative assessment, we plan to perform a campaign of numerical simulations – possibly with patient-specific boundary data and certainly with more refined meshes - for a more quantitative analysis of the interplay of rheology and fluid patterns. The follow up of the study is exactly to retrieve pediatric data of sickle vs. non-sickle age-matched geometries, and reproduce the results obtained here with a precise quantitative assessment. The ultimate goal is to find a precise correlation between the altered rheological properties and the stroke risk in young people with sickle cell anemia. As for the rheological models, another important aspect of CFD is the solution of rigorous data

assimilation problems for a patient-specific quantification of apparent viscosity in diseased patients. This means that we systematically compare numerical results with available measures for different values of the viscosity to find the value that best describes measurements. This can be done by performing rigorous numerical procedures of what is called “variational data assimilation” [129-131].

Currently, few researchers are examining the fluid dynamics in large arteries associated with sickle cell anemia, and the difficulty in doing so is not minimal. Blood rheology is affected by red cells in two ways: rouleaux formation at low shear rates and inelastic collisions at high shear rates [103]. The altered shapes, density, and membrane viscosity, and associated variability among the RBCs in sickle cell anemia as they progress from reticulocytes to irreversibly sickled cells over the 9-10 days of their lifespan [106], probably affects both of these aspects. The impact of the shape on the effects of the collision (with consequent altered energy balance) may require some sophisticated rheology based on differential models. However, all these models require the quantitative tuning of many parameters (beyond the viscosity) which at this stage is out of reach. There are investigations of the cerebral anatomy in the MCA and ICA by other groups, and they have found tortuosity to be implicated in stenosis formation [132]. This is interesting to note as certain tortuosity and curvature has been associated with aneurysm formation and rupture [133]. As demonstrated in this paper geometrical differences in the arteries themselves between sickle and non-sickle individuals can have drastic effects on the hemodynamics. Quantifying these differences may allow clinicians to predict patients who are at risk of stroke prior to the elevated velocities used currently, enabling patients to get treatment sooner.

CHAPTER 4 AGE-DEPENDENT CHARACTERIZATION OF THE CAROTID AND CEREBRAL ARTERY MORPHOLOGIES IN A TRANSGENIC MOUSE MODEL OF SICKLE CELL ANEMIA

4.1 Introduction

Sickle cell disease (SCD) is one of the more prevalent blood disorders worldwide with more than 300,000 new individuals born each year afflicted by the disease. Sickle cell anemia (SCA), specifically, is caused by a missense mutation that substitutes glutamic acid for valine in hemoglobin. This change in molecular structure causes the hemoglobin in red blood cells (RBCs) to polymerize and aggregate under de-oxygenated conditions, leading to deformation and increased rigidity of the cell that cause blockages in the microvasculature that can damage organs and lead to painful episodes known as sickle crisis. SCA also has effects on the large arteries, most notably in the elevated occurrence of strokes in individuals with SCA.

The chance of ischemic stroke is greatly elevated for young individuals with SCA, occurring in 11% of people between the ages of 2 and 18 [33]. Then, during ages 20-30, the risk of ischemic stroke falls, but is replaced with an increased risk of hemorrhagic stroke. Upon reaching early to mid-30s, the risk of ischemic stroke begins to dominate again in individuals with SCA [52]. Age is an important factor for sickle cell-mediated strokes, and mechanisms behind variations in types of strokes during specific times of life with SCA are unknown. Some clues can be extracted from investigating the vascular morphology. In individuals who have suffered ischemic strokes, cerebral angiograms have

shown the presence of stenosis [28, 43, 50]. Additionally, autopsies of individuals who have died from sickle-related strokes, show defined markers of intimal hyperplasia [4, 50].

In order to provide insight into underlying structural changes that affect stroke risk in relation to age, mouse models can be used. The murine cerebral circulation displays similarities to humans; the brain is supplied by a pair of vertebral and carotid arteries that branch to form a network resembling the Circle of Willis (CoW) in humans [134]. The Townes sickle cell transgenic mouse model has been beneficial for investigating pulmonary and hematological pathophysiology [135-137], with a few studies on cerebrovascular complications of SCA [138-143]. These studies however have not investigated changes to the cerebral vascular anatomy, specifically in the arteries associated with stroke risk.

The goal of this study is to determine how morphology of carotid and cerebral arteries change as the mice age, and any differential effects caused by sickle cell anemia. In a cross-sectional study, we use a combination of ultrasound and microcomputed topography (micro-CT), to determine morphometries of carotid and cerebrovascular arteries of Townes mouse model. Both techniques have distinct advantages and disadvantages, which, when combined, can provide a comprehensive morphometric characterization. Ultrasound in living mice allows for longitudinal studies that can be used to obtain arterial dimensions during systole and diastole. However, murine vasculature is much smaller than humans, with vessels approximately $1/30^{th}$ the size introducing limitations in resolution and access to arteries in the skull [144-146]. Alternatively, advances in micro-CT imaging procedures for small animal models through the use of perfused contrast agents have enable researchers to investigate structures within a voxel

size of 8 μm [147, 148]. For these reasons, we also used micro-CT on casts of the carotid and cerebral arteries in mice. Casts were created by a plastination method using a radiopaque polymer that hardens in the vessels. This cast was then scanned by micro-CT and reconstructed *in silico* to acquire morphological information of the smaller carotid and cerebral arteries. Casts of the arteries have their own tradeoffs in that it is an endpoint analysis, disallowing longitudinal studies from the same subject. These modalities were used to obtain detailed morphologies of the primary branches of the common carotid artery (CCA), internal carotid artery (ICA), middle cerebral artery (MCA), and anterior cerebral artery (ACA) of mice homozygous for human β globin S, the sickle cell allele (SS) or mice heterozygous for human sickle cell allele and wildtype β globin A allele (AS). Our results suggest sickle cell disease alters the vascular morphology in mice 12 and 24 weeks old, and these age-specific changes may be relevant for age-related risk of types of strokes.

4.2 Methods

4.2.1 Townes Sickle Transgenic Moise

Townes sickle cell transgenic mice (Jackson Laboratories, Bar Harbor ME) were used for a cross-sectional study. This humanized knock-in model of sickle cell anemia was generated by knocking in the human hemoglobin genes (α, β, and γ), including the β-globin S mutation, into mice null for murine hemoglobin genes [135]. Mice homozygous for β-globin S mutation (SS) were compared to littermate heterozygous (AS) controls. Three different ages were used for the study: 4-weeks, 12-weeks, and 24-weeks, with each age corresponding to a different risk and type of stroke risk in humans with SCA (Table 4.1) [52, 149]. Each age group consisted of 4-7 mice [4 weeks old ($n_{AS} = 6$, $n_{SS} = 4$), 12 weeks old ($n_{AS} = 7$, $n_{SS} = 4$), 24 week ($n_{AS} = 4$, $n_{SS} = 4$)], and all mice were cared for at Peking

University (Beijing, China) using standard mouse caring techniques, and ethical protocols were followed based on the Institutional Animal Care and Use Committee of Peking University (Beijing, China).

Table 4.1 Relation of mouse and human ages and types of stroke most likely to occur in humans with sickle cell anemia

Mouse Age (Weeks)	Approximate Human Age (Years)	Most Likely Type of Stroke in Humans with SCA
4	12.5	Ischemic
12	20	Hemorrhagic
24	30	Ischemic

4.2.2 High Frequency Ultrasonography

Ultrasound measurements were performed in all mice using a VEVO 2100 Doppler system (VisualSonics, Toronto, ON, Canada) with a 22-55 Mhz transducer (MS550D, wavelength ~50μm – 2mm). Mice were anesthetized with 5% isoflurane on a horizontal platform in the supine position in order to monitor heart rate. Hair was then removed from the neck and pectoralis, before ultrasound gel (Aquasonic, Parker Laboratories) was applied to improve signal acquisition. After the specimen was secured to the platform 1% isoflurane mixed with oxygen is provided to maintain the anesthesia. The right carotid bifurcation was visualized in the sagittal plane with B-mode by applying the ultrasound beam perpendicular to the arteries, which were identified based on their depth from the surface of the skin, the direction of flow, and spatial orientation. A 2D recording was taken of the right carotid bifurcation over 2-3 seconds, and then the process was repeated for the

left side. Dicom recordings were analyzed in ImageJ to determine arterial diameter during systole and diastole. Diameter was determined as perpendicular distance from the top to bottom of a vessel in the sagittal plane. Two measurements were taken to obtain an average common carotid artery diameter at 0.5 and 1.5mm upstream of the bifurcation. In the extracranial internal carotid artery, only one measurement could be taken 0.5mm downstream of the bifurcation. Three measurements were acquired at each of the above locations to obtain an average across multiple cardiac cycles.

4.2.3 Preparation for arterial casting

Following ultrasound measurements, each mouse recuperated for 6-24 hours before being prepared for casting of arteries [150, 151]. Briefly, mice were anesthetized with urethane at a dose of 1g/kg, and laparotomy was performed to gain access to the abdominal aorta, where a 24-gauge catheter was used to make a direct puncture. An incision was created in the vena cava to provide an exit point for blood, whereupon a heparinized saline (25 U/mL) was injected through the catheter at a pressure of approximately 100-120 mmHg, the systolic pressure in mice [152, 153]. Pressure was monitored using a sphygmomanometer, and a heparinized solution was perfused through the mouse until the effluent at the vena cava became clear. Following exsanguination, a 10% solution of buffered formaldehyde was perfused through the catheter for 15 minutes at a pressure of 100 mmHg to fix the blood vessels. Afterwards, 5 mL of Microfil HV 122 Yellow (Flow Tech, Carver, MA) was manually perfused. Following the procedure, the upper torso, including the head, was removed and stored in 10% buffered formaldehyde for 5 days before undergoing decalcification in 10% HCl for 48 hours to remove bone.

4.2.4 Micro-Computed Tomography

Carotid and cerebral artery casts were examined using a high-resolution micro-CT imaging system (Quantum GX, Perkin Elmer). Heads to be scanned were placed prone in a specimen tube (diameter 30.7 mm) with the long axis of the head parallel to the tube's long axis. Micro-CT images were collected over a 4-mm thick section extending from the nose to the back of the neck, scanning in the transverse plane. Each scan was performed with a beam intensity of 80 microamperes, a beam energy of 70 kV, and an isotropic voxel resolution of 50 μm.

4.2.5 Image Processing and Morphological Analysis

Micro-CT images were used to create 3D models of the cerebral and carotid arteries for each specimen. Mimics Materialise 15.0 (Leuven, Belgium), was used to manually segment and reconstruct the left and right vasculature, extending from the common carotid arteries to the middle cerebral and anterior cerebral arteries. A minimum threshold was optimized for each specimen, which produced the largest vessel diameter without creating large irregularities on the surface. After a threshold was chosen, a preliminary mesh of the vascular network was created, containing arterial segments of the common carotid artery (CCA), external carotid artery (ECA), internal carotid artery (ICA), anterior cerebral artery (ACA), and middle cerebral artery (MCA). Smoothing algorithms from Vascular Modeling Toolkit *(VMTK)* were applied to remove artifacts created from the reconstruction and re-meshing [113]. The internal carotid artery is divided into two sections: the extracranial internal carotid artery (eICA) and intracranial internal carotid artery (ICA), separated by the bifurcation at the ophthalmic artery (OA) branch. After reconstruction, Mimics was used to calculate morphometric centerline properties along the length of each arterial

segment at a resolution of 0.05 mm. These morphometric values include the maximum inscribed internal diameter, perimeter, and cross-sectional area, along the length of each arterial segment. When analyzing the morphometric values, regions associated with bifurcations were considerably larger than the rest of the artery, thus, to avoid skewing results 0.5mm was removed from the end of each arterial segment if that section was part of a bifurcation. The arteries could not be reconstructed in one SS 4-week mouse and one SS 24-week mouse.

4.2.6 Statistical Analysis

All statistical tests were performed in Graphpad Prism 7. Ultrasound and micro-CT data were plotted across age, and data from each group of animals are reported as the mean ± standard error of the mean. A value of $p<0.05$ was taken to be significant. The effect of genotype was examined using unpaired t-test, and a paired t-test was used to compare measurements taken from ultrasound and micro-CT methodologies. A one-way ANOVA was performed to determine differences across the various ages.

4.3 Results

4.3.1 Enlarged common carotid diameters in 12-week SS mice measured by ultrasound and micro-CT

From ultrasound imaging, luminal diameters were measured in the common carotid and the extracranial portion of the internal carotid arteries of mice 4, 12, and 24-weeks of age. An average diameter between two points 0.5 mm and 1.5 mm upstream from the carotid bifurcation was calculated for the common carotid artery (Fig. 4.1A). At 12-weeks, CCA luminal diameters in SS mice during systole were 19.3% and 11.5% larger than those

of age-matched AS mice on the left and right sides, respectively (n=4, $p<0.05$) (Fig 4.1B). The CCA remained significantly enlarged during diastole with a 20.1% and 13.7% diameter increase occurring in the left and right sides of SS mice. In the extracranial ICA, a single point, 0.5 mm distal from the carotid bifurcation was measured, and no significant differences were found in this segment at any age (Fig. 4.1A). Table 4.2 contains all the measurements from ultrasound imaging of the extracranial carotid arteries.

Since there was a limitation in obtaining measurements intracranially with ultrasound, we validated that comparable measurements were acquired between ultrasound performed on living mice, and the arterial casts measured by micro-CT, on non-living animals (Fig. 4,2). Mice 12 weeks old were used for comparisons since that was the age when statistically significant differences were observed between SS and AS carotid arteries (Fig. 4.3). Values calculated from the reconstructed arteries were only comparable to systolic ultrasound measurements as a systolic pressure of at least 100 mmHg was maintained throughout the casting process. The maximum inscribed diameter, which is the largest circle that can fit within the boundaries of a vessel cross-section (Fig 3A), were averaged along the length of the CCA and extracranial ICA. In the CCA this length extended 0.5 to 1.5 mm proximal of the carotid bifurcation, and in the extracranial ICA this extended 0.4 to 0.6 mm downstream of the bifurcation.

There were no significant differences between diameters from ultrasound and micro-CT methodologies (paired T-test, n=4, $p>0.05$). Diameters calculated through the micro-CT method paralleled the significant differences in the common carotid artery of the 12-week group for SS vs. AS mice (Fig 3B). Statistically significant differences were

measured in the extracranial ICA using the micro-CT technique, but not by ultrasound (Fig. 4.3C).

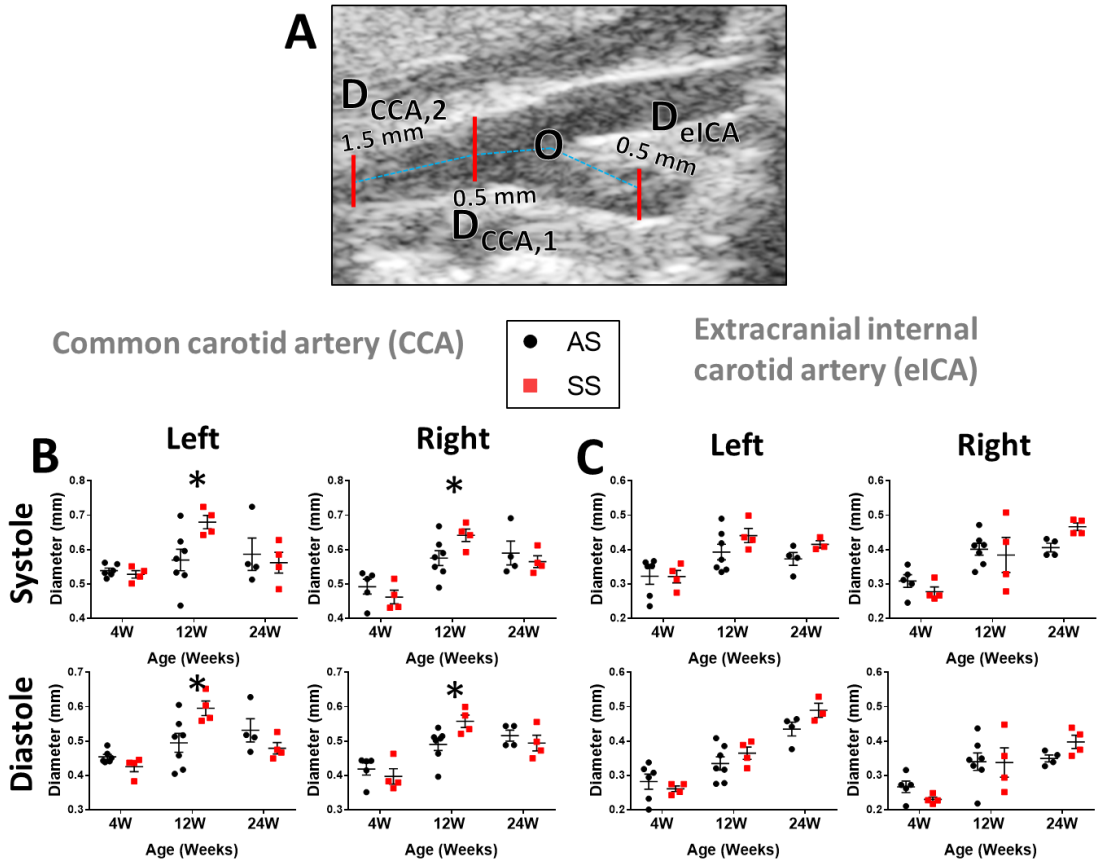

Figure 4.1: The common carotid artery (CCA) luminal diameter is enlarged in SS mice at 12 weeks of age during the entire cardiac cycle

(A) The luminal diameter was measured at in the CCA 0.5 and 1.5 mm upstream from the carotid bifurcation (labeled O), and in eICA 0.5 mm downstream from the carotid bifurcation. **(B)** The common carotid artery was significantly larger in 12-week SS mice during both systole and diastole for the left and right sides. **(C)** There are no significant differences found in the eICA diameters of SS and AS mice. *$p < 0.05$ SS compared with AS by T-test. Error bars are SEM.

Table 4.2 Morphological measurements from ultrasound of the extracranial internal carotid arteries in mice with sickle trait (AS) and sickle cell anemia (SS).

	Systolic					
Age (Weeks)	4		12		24	
Genotype	AS	SS	AS	SS	AS	SS
Left CCA Diameter (mm)	0.539 (0.007)	0.531 (0.015)	0.57 (0.031)	0.68 (0.019)[a]	0.54 (0.029)	0.464 (0.007)
Right CCA Diameter (mm)	0.493 (0.022)	0.473 (0.024)	0.576 (0.022)	0.642 (0.018)	0.59 (0.035)	0.576 (0.019)
Left eICA Diameter (mm)	0.323 (0.023)	0.309 (0.018)	0.393 (0.023)	0.441 (0.021)	0.435 (0.02)	0.495 (0.035)
Right eICA Diameter (mm)	0.311 (0.023)	0.264 (0.003)	0.401 (0.017)	0.385 (0.051)	0.406 (0.012)	0.473 (0.013)

	Diastolic					
Age (Weeks)	4		12		24	
Genotype	AS	SS	AS	SS	AS	SS
Left CCA Diameter (mm)	0.454 (0.008)	0.422 (0.02)	0.495 (0.027)	0.596 (0.021)[a]	0.587 (0.047)	0.532 (0.034)
Right CCA Diameter (mm)	0.419 (0.018)	0.409 (0.027)	0.491 (0.018)	0.558 (0.018)[a]	0.516 (0.016)	0.493 (0.032)
Left eICA Diameter (mm)	0.282 (0.022)	0.257 (0.01)	0.335 (0.019)	0.365 (0.018)	0.373 (0.019)	0.419 (0.017)
Right eICA Diameter (mm)	0.268 (0.022)	0.224 (0.003)	0.341 (0.025)	0.338 (0.043)	0.35 (0.01)	0.411 (0.019)

CCA, Common Carotid Artery; eICA, Extracranial Internal Carotid Artery.
[a] $p < 0.05$ compared with AS by t-test. Number in parentheses is standard deviation of the measurement.

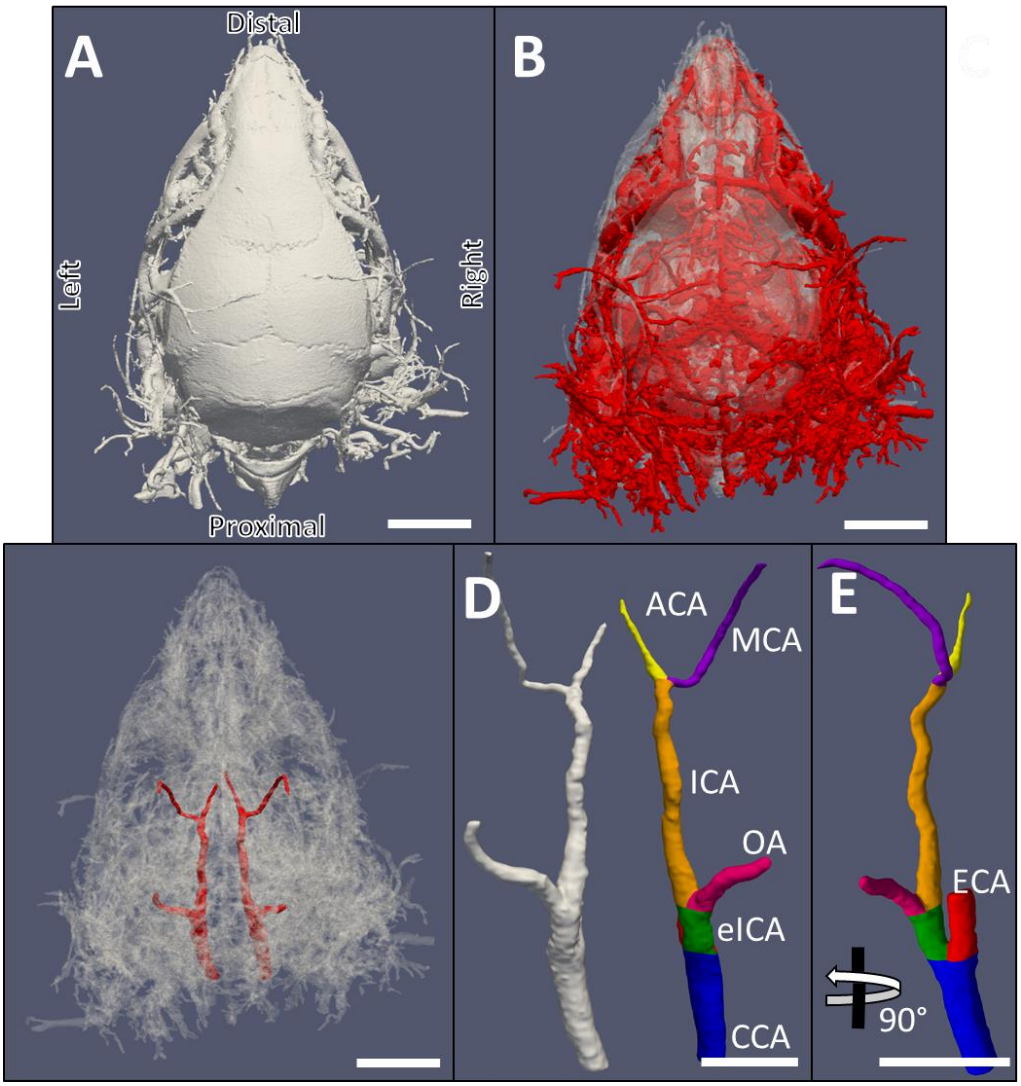

Figure 4.2 Casts of blood vessels to acquire morphology of carotid and cerebral arteries.

Top view of perfusion casting process. **(A)** Microfil, a radio-opaque polymer, was injected into the aorta of mice after exsanguination and fixation of the blood vessels under pressurized conditions. **(B)** The head of mouse was decalcified in a 10% HCL solution for 36 hours to remove bone. **(C)** The reconstructive software Mimics Materialise was used to segment and reconstruct carotid and cerebral arteries. **(D,E)** Final vascular model with individual arterial segments colored. CCA (common carotid artery), eICA (extracranial internal carotid artery), ECA (external carotid artery), OA (ophthalmic artery), intracranial ICA (internal carotid artery), ACA (anterior cerebral artery), MCA (middle cerebral artery). Scale bars = 5 mm.

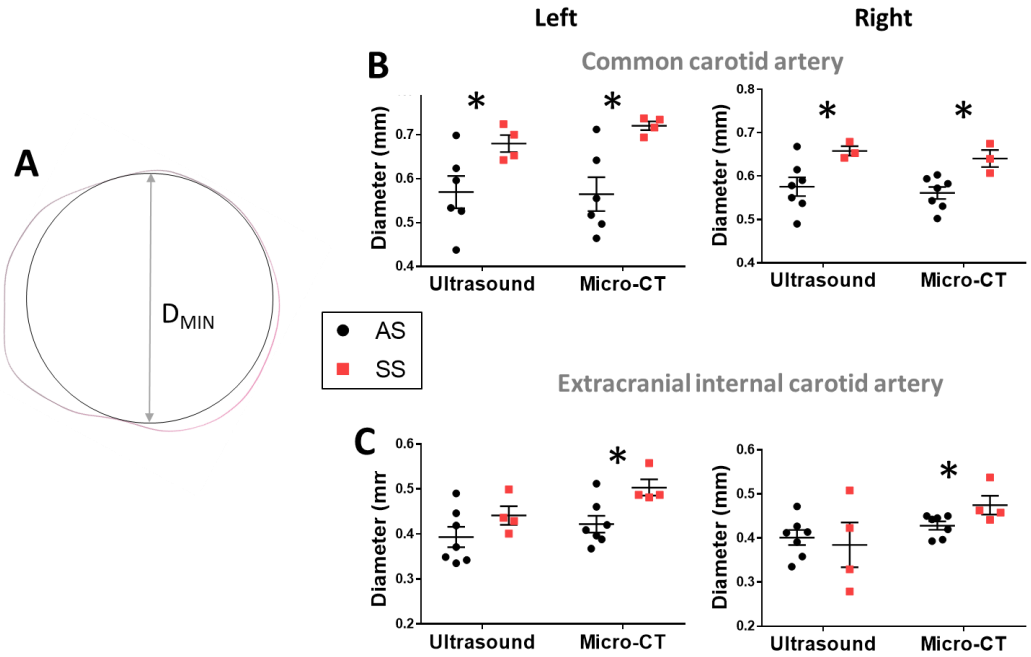

Figure 4.3: Reconstructed models from artery casts recapitulate ultrasound measurements from living animals

Comparison of diameters measured from ultrasound and micro-CT in the 12-week age group. **(A)** micro-CT measurements reveal CCA diameters were larger in SS mice, paralleling results from the ultrasound study. No significant differences were found between the CCA diameters measured through ultrasound and diameters calculated from reconstructed micro-CT images. **(B)** Diameters calculated from micro-CT were significantly larger in SS mice. No significant differences were observed between both methodologies, however, diameters calculated through micro-CT had smaller SEM. *$p<0.05$ SS compared with AS by T-test. Paired T-test was performed between ultrasound and μCT methodologies for the same genotype. Error bars are SEM.

4.3.2 Diameter vs. perimeter and cross-sectional area as reliable metrics.

Diameter measurements were useful to extract data from the ultrasound, but it assumed a perfectly circular geometry, which was not usually the case for these arteries. Using the micro-CT analysis of casts, cross-sectional shapes of the artery were evaluated for ellipticity, a metric that can be used to determine the roundness of polygons. An ellipticity value of 0 is perfectly circular, and values closer to 1 indicate a flatter object. The ellipticity in both AS and SS was found to be in the range between 0.4 and 0.6, denoting non-circular geometry (Figure 4.4A). Although the diameters (Figure 4.4B) were useful for comparing methods of ultrasound vs. micro-CT (Figure 4.3), using micro-CT, the cross-sectional perimeter and area of carotid arteries could also be calculated along the same length of the artery and were better at capturing the irregular geometry presented by the arteries. The perimeter and cross-sectional area were 34.6% and 65% larger, respectively, in the left extracranial ICA of SS mice 12 weeks of age ($p<0.05$, $n=3$), whereas the right extracranial ICA increase was only 8.3% and 18.4%, which was not significant (Fig 4.4C&D). There were no significant differences in either perimeter or area at 4 or 24 weeks between AS and SS mice. Table 4.3 contains all the measurements from micro-CT imaging of perfusion casts for the extracranial carotid arteries.

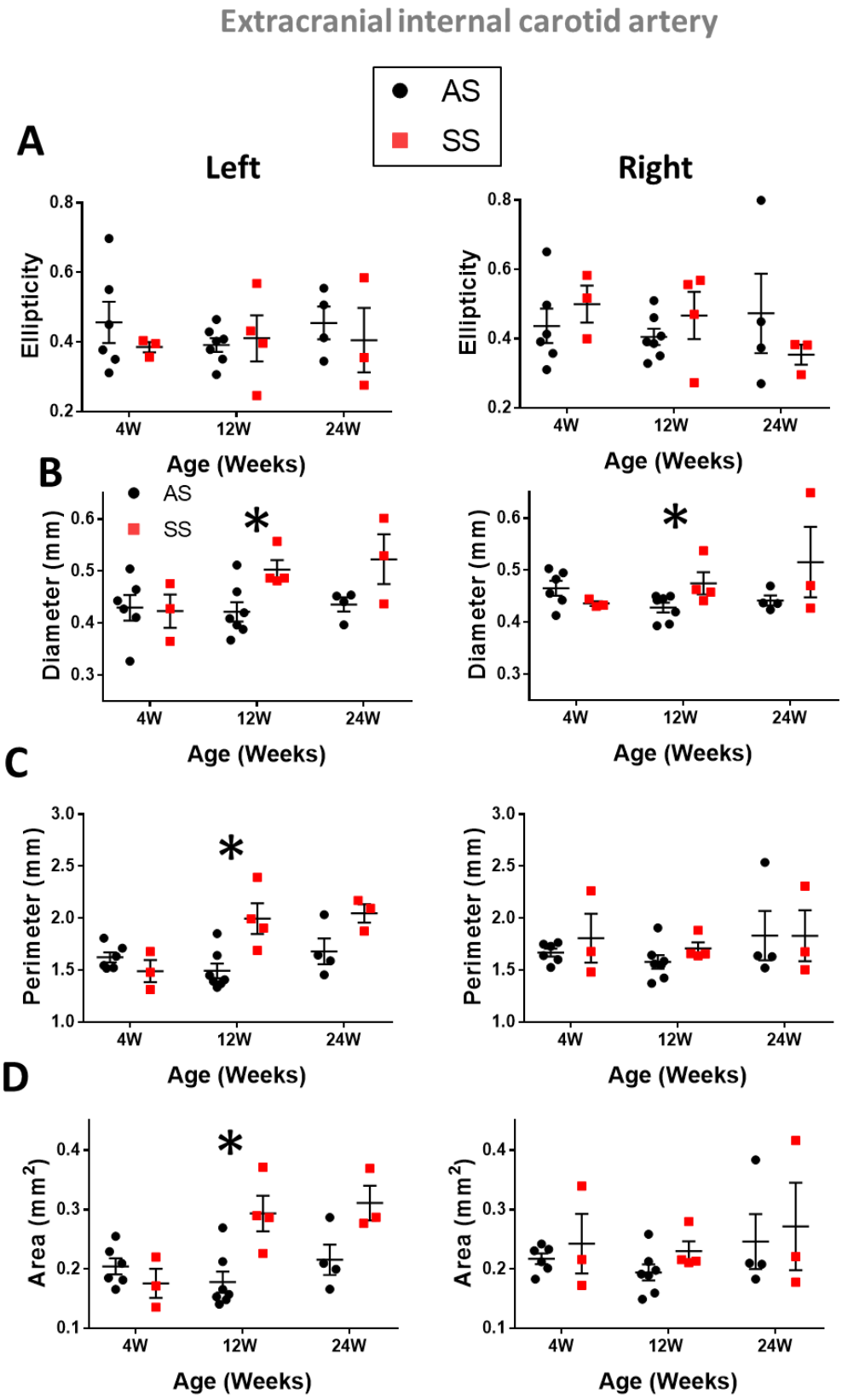
Extracranial internal carotid artery
AS
SS
A
Left
Right
Ellipticity
0.8
0.6
0.4
0.2
4W
12W
24W
Age (Weeks)
B
Diameter (mm)
0.6
0.5
0.4
0.3
*
C
Perimeter (mm)
3.0
2.5
2.0
1.5
1.0
D
Area (mm²)
0.4
0.3
0.2
0.1

Figure 4.4: The extracranial internal carotid artery is enlarged on the left side
(A) The maximum inscribed circle in a cross-section of the internal carotid artery. **(B)** The maximum inscribed diameter in the extracranial ICA was found to be significantly larger in SS mice for both the left and right sides at 12 weeks. **(C)** The average ellipticity was calculated along the extracranial internal carotid artery from 0.4 - 0.6 mm downstream of the carotid bifurcation. Ellipticity for both AS and SS mice are between 0.4 and 0.6, denoting a more irregular shape (E = 0). Further examination of **(D)** perimeter and **(E)** cross-sectional area reveals only the left side to have significantly larger morphometric values at 12 weeks. *$p < 0.05$ SS compared with AS by T-test. Error bars are SEM

Table 4.3: Morphological measurements from micro-CT analysis of the extracranial internal carotid arteries in mice with sickle trait (AS) and sickle cell anemia (SS).

	Left eICA					
Age (Weeks)	4		12		24	
Genotype	AS	SS	AS	SS	AS	SS
Diameter (mm)	0.43 (0.024)	0.423 (0.032)	0.421 (0.019)	0.503 (0.018)[a]	0.436 (0.013)	0.523 (0.048)
Perimeter (mm)	1.624 (0.048)	1.491 (0.106)	1.494 (0.071)	1.997 (0.147)[a]	1.681 (0.124)	2.048 (0.088)
Area (mm^2)	0.204 (0.014)	0.176 (0.024)	0.178 (0.018)	0.293 (0.03)[a]	0.216 (0.026)	0.311 (0.029)

	Right eICA					
Age (Weeks)	4		12		24	
Genotype	AS	SS	AS	SS	AS	SS
Diameter (mm)	0.465 (0.014)	0.436 (0.004)	0.428 (0.01)	0.475 (0.021)[a]	0.442 (0.01)	0.516 (0.068)
Perimeter (mm)	1.67 (0.039)	1.809 (0.235)	1.579 (0.065)	1.71 (0.058)	1.833 (0.237)	1.831 (0.244)
Area (mm^2)	0.217 (0.009)	0.243 (0.05)	0.194 (0.014)	0.229 (0.017)	0.246 (0.046)	0.272 (0.073)

eICA, Extracranial Internal Carotid Artery.
[a] $p < 0.05$ compared with AS by T-test.
Number in parentheses is standard deviation of the measurement.

4.3.3 Internal Carotid artery length is similar between SS and AS mice

Internal carotid artery measurements were captured with micro-CT. When examining the entire ICA (extracranial + intracranial) a significant increase occurred as mice aged from 4 to 12 weeks. Length in the left ICA increased by 11% ($p<0.001$) and 8% ($p<0.01$) in AS and SS mice, respectively, with similar increases of 16% ($p<0.001$) and 11% ($p=0.0525$) for the right ICA (Fig 4.5A). There was no significant difference between 12 and 24 weeks. Comparisons of body weight showed similar trends from 4 to 12 weeks. Body weight was 57% ($p<0.001$) and 53% ($p<0.001$) greater from 4 to 12 weeks in AS and SS mice, respectively. At 24 weeks, weight increased by 3% ($p>0.05$) in AS and 17% ($p<0.05$) in SS. No significant differences were found between genotypes at the same age. These results suggest that radial differences observed in the carotid arteries were not a result of differences in the length or weight of the animal.

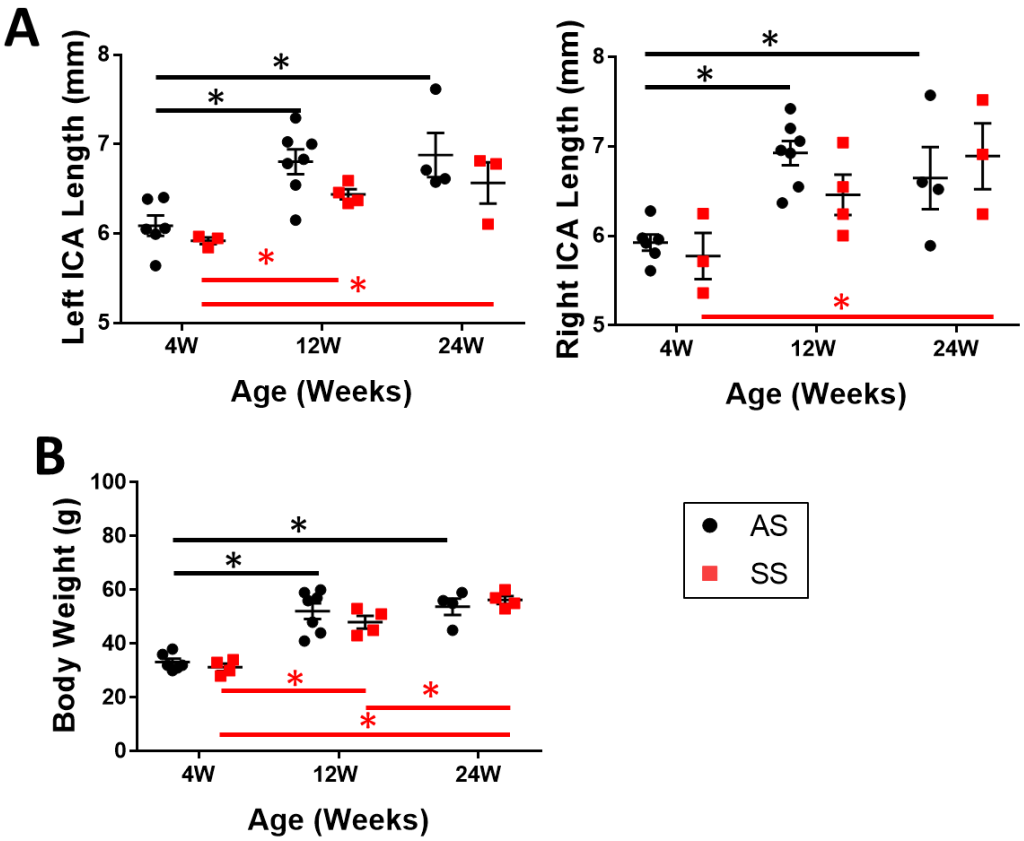

Figure 4.5: Size and axial growth is similar between homozygous and heterozygous sickle mice

(A) Growth axially is quantified based on ICA length (extracranial + intracranial). ICA length increases significantly from 4 to 24 weeks in AS and SS, and no significant differences were found between AS and SS mice in any of the age groups. **(B)** Significant increase in body weight occurs from 4 to 12 weeks in AS and SS mice, but no differences were found in the same age group between genotypes. SS was compared with AS via T-test. The same genotype was compared across ages using a one-way ANOVA, *$p < 0.05$.

4.3.4 Narrowing in the left distal intracranial ICA of 12 and 24-week SS mice

Next, we compared intracranial internal carotid arteries (ICA) reconstructed from 4, 12 and 24-weeks old mice. Averaged morphometric values were taken from two sections: (1) the proximal end, which begins 0.5mm from the beginning of the ICA to the midpoint of the vessel; and (2) the distal end, which extends from to the midpoint to 0.5 before the end of the vessel (Fig 4.6A). At 12-weeks, the proximal diameter, perimeter, and cross-sectional area on the left-side of SS mice were enlarged compared to AS controls, increased by 15% (0.048+/-0.02), 16% (1.322 mm +/- 0.025), and 34% (0.139 mm^2 +/- 0.005), respectively (Fig 4.6C&D). This difference continued distally, where a 16% ($p<0.05$) and 32% ($p<0.05$) increase was measured in perimeter and area. At 24 weeks, the left proximal section was also enlarged for SS mice, with a 17% increase in perimeter and 40% increase in area as compared to AS. Unlike, their younger 12-week counterparts, morphometric values were not significantly different at distal ICA.

These changes from the proximal to distal ICA could be visualized by plotting the mean area for each genotype along the length (Fig 4.7.1). At 4 weeks, SS and AS mice had similar areas along the length. However, in the 12- and 24-week age groups SS mice had significantly larger cross-sections at the proximal ICA, which narrowed, leading to a loss of differences once reaching the opposite end of the artery. To quantify this narrowing in the ICA, area was normalized to the area at the proximal start of the artery for each mouse (Fig 4.7.2). Using this method, variability between specimens can be accounted, and differences previously unseen begin to emerge. The normalized area in 12-week SS mice was as much as 36% lower compared to AS mice. At 24 weeks these differences were even larger; at certain points along the ICA the percent change in area for SS mice reached as

low as -62 and -56% in the left and right sides, respectively. Both the left and right intracranial internal carotid arteries narrowed in 12 and 24-week-old SS mice. Table 4.4 contains the measurements from micro-CT imaging for the intracranial internal carotid arteries.

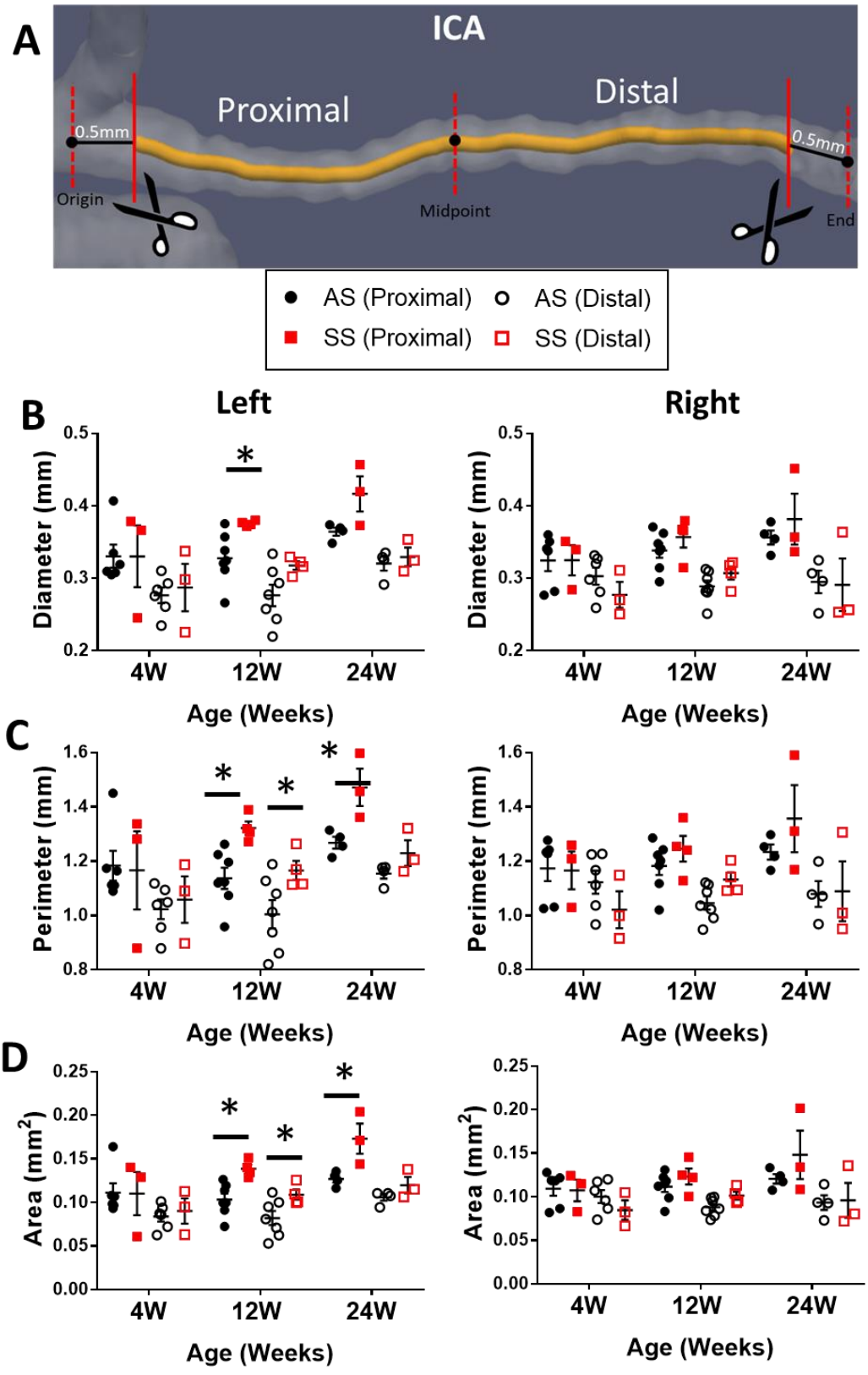
A
ICA
Proximal
Distal
0.5mm
0.5mm
Origin
Midpoint
End
AS (Proximal)
AS (Distal)
SS (Proximal)
SS (Distal)
B
Left
Right
Diameter (mm)
C
Perimeter (mm)
D
Area (mm²)
4W
12W
24W
Age (Weeks)
*

Figure 4.6: Radial growth of the distal intracranial ICA in SS mice is slowed between 12 and 24 weeks of age

(A) The intracranial ICA was divided into two regions: proximal, extending 0.5 from the origin to the midpoint and distal which continues from the midpoint to 0.5 mm before the ICA bifurcation (labeled end). **(B)** Diameter, **(C)** perimeter, and **(D)** cross-sectional area is compared between AS and SS mice at the proximal and distal segments of the intracranial ICA. The left ICA is significantly larger by all morphometric values at 12 weeks at the proximal and distal ends. The proximal ICA is also enlarged in 24-week SS mice but narrows at distal portion losing significance at that end of the ICA. *$p<0.05$ SS compared with AS by T-test. Error bars are SEM.

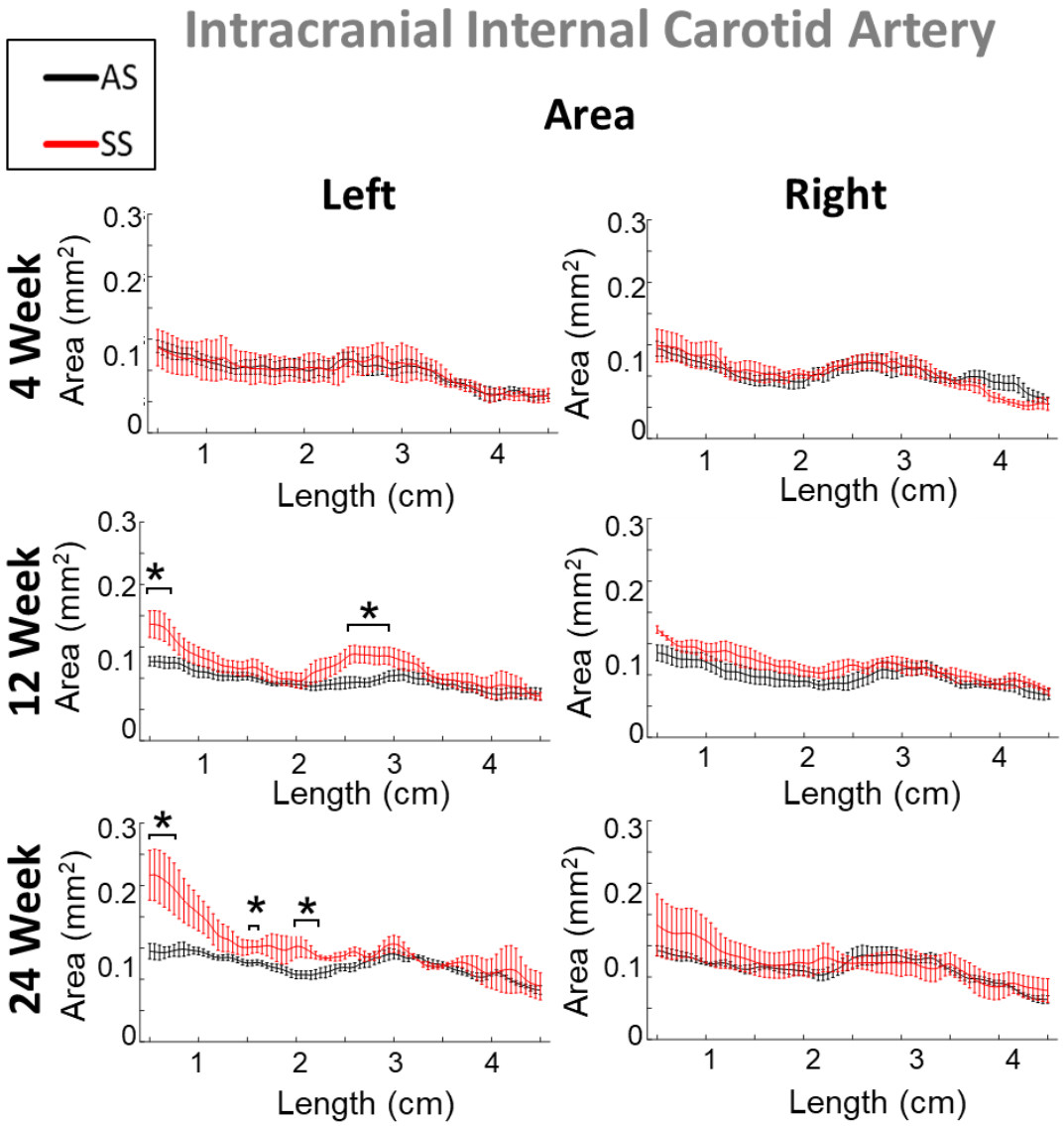

Figure 4.7.1: Distal Intracranial Internal Carotid Artery Narrows in 12 and 24-week SS mice.

Mean values for bulk area and percent change in area are plotted along the length of the intracranial ICA. **(A)** The left proximal ICA is enlarged in 12- and 24-week SS mice, but differences are lost upon moving towards the distal section of the artery. *$p<0.05$ SS compared with AS by T-test. Error bars are SEM.

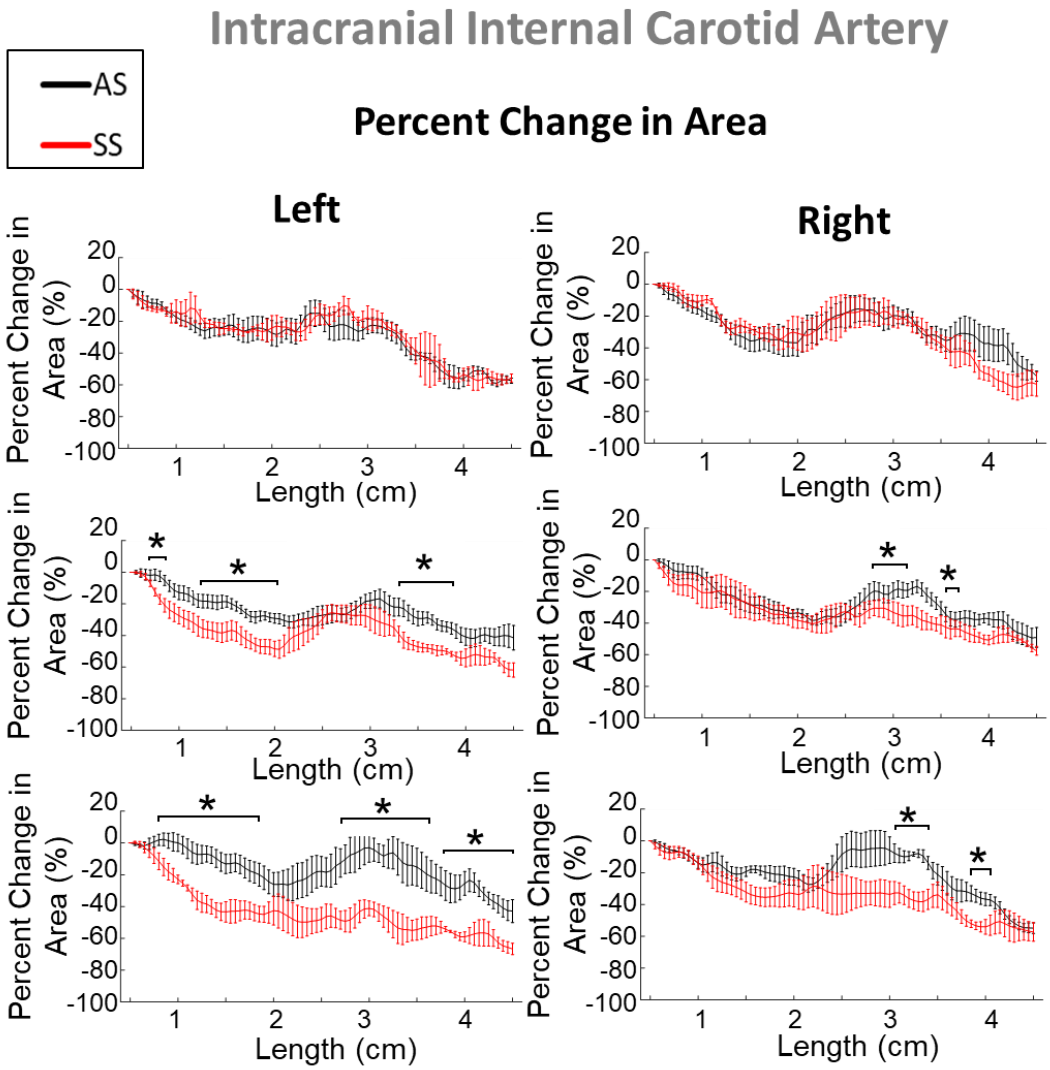

Figure 4.7.2: Distal Intracranial Internal Carotid Artery Narrows in 12 and 24-week SS mice.

Area was normalized to the starting point of artery to account for variability between subjects. The ICA narrows significantly from the proximal to distal end of the artery in 24-week SS mice as compared to age-matched controls. *p<0.05 SS compared with AS by T-test. Error bars are SEM.

Table 4.4: Morphological measurements from micro-CT analysis of the intracranial internal carotid arteries in mice with sickle trait (AS) and sickle cell anemia (SS).

		Left ICA					
Age (Weeks)		4		12		24	
Genotype		AS	SS	AS	SS	AS	SS
Diameter (mm)	Proximal	0.332 (0.016)	0.33 (0.044)	0.33 (0.013)	0.377 (0.003)[a]	0.365 (0.006)	0.423 (0.026)a
	Distal	0.268 (0.011)	0.277 (0.03)	0.272 (0.012)	0.312 (0.007)[a]	0.316 (0.008)	0.32 (0.016)
Perimeter (mm)	Proximal	1.187 (0.054)	1.169 (0.146)	1.143 (0.038)	1.322 (0.025)[a]	1.271 (0.022)	1.49 (0.072)[a]
	Distal	1.012 (0.042)	1.022 (0.082)	0.996 (0.044)	1.152 (0.039)[a]	1.141 (0.011)	1.208 (0.058)
Area (mm^2)	Proximal	0.112 (0.011)	0.111 (0.025)	0.104 (0.007)	0.139 (0.005)[a]	0.128 (0.004)	0.178 (0.018)[a]
	Distal	0.082 (0.007)	0.084 (0.013)	0.08 (0.007)	0.106 (0.007)[a]	0.103 (0.002)	0.116 (0.011)
Length		4.965 (0.091)	4.794 (0.068)	5.587 (0.133)	5.291 (0.034)	5.653 (0.196)	5.29 (0.203)

		Right ICA					
Age (Weeks)		4		12		24	
Genotype		AS	SS	AS	SS	AS	SS
Diameter (mm)	Proximal	0.326 (0.014)	0.326 (0.021)	0.34 (0.009)	0.36 (0.015)	0.355 (0.009)	0.389 (0.041)
	Distal	0.289 (0.011)	0.268 (0.015)	0.286 (0.008)	0.305 (0.005)	0.295 (0.012)	0.292 (0.035)
Perimeter (mm)	Proximal	1.176 (0.045)	1.169 (0.071)	1.186 (0.029)	1.252 (0.048)	1.227 (0.026)	1.368 (0.136)
	Distal	1.08 (0.039)	0.268 (0.015)	1.035 (0.027)	1.125 (0.02)[a]	1.086 (0.041)	1.1 (0.113)
Area (mm^2)	Proximal	0.11 (0.008)	0.108 (0.013)	0.112 (0.005)	0.125 (0.009)	0.119 (0.005)	0.151 (0.031)
	Distal	0.093 (0.007)	0.08 (0.009)	0.086 (0.004)	0.1 (0.003)	0.094 (0.007)	0.098 (0.02)
Length		4.973 (0.024)	4.983 (0.15)	5.724 (0.103)	5.362 (0.128)	5.73 (0.283)	5.744 (0.307)

ICA, Intracranial Internal Carotid Artery.
[a] $p < 0.05$ compared with AS by T-test.
Number in parentheses is standard deviation of the measurement.

4.3.5 Portions of the anterior cerebral arteries are significantly narrower in SS mice

Two tributaries branch from the ICA, the middle cerebral (MCA) and anterior cerebral arteries (ACA) and were examined using the same methods from the reconstructed micro-CT models. In the ACA, morphometric values were analyzed along a length of 0.5 to 2.5 mm, whereas the longer MCA calculated values from 0.5 to 4.5 mm of the origin. When examining the area, neither the ACA nor MCA differed significantly in size between AS and SS mice (Fig 4.8.1 & Fig 4.8.2). It should be noted that at 24 weeks, the right ACA in SS mice had significantly smaller diameters ($*p<0.05$). To investigate the geometry further, normalized area was plotted vs. length for the ACA and MCA (Fig 4.9 and Fig 4.10). Using this approach, the left ACA was found to be enlarged in 4-week SS mice. However, at 12 and 24 weeks the ACA of SS mice were significantly smaller in both the left and right sides, narrowing by up to 60% in some segments. The normalized MCA area between SS and AS mice changed throughout aging. SS mice had enlarged MCAs at 4-weeks, but by 24 weeks the cross-sectional area was narrowed compared to AS controls. Table 4.5 contains the measurements from micro-CT imaging of cast for the cerebral arteries.

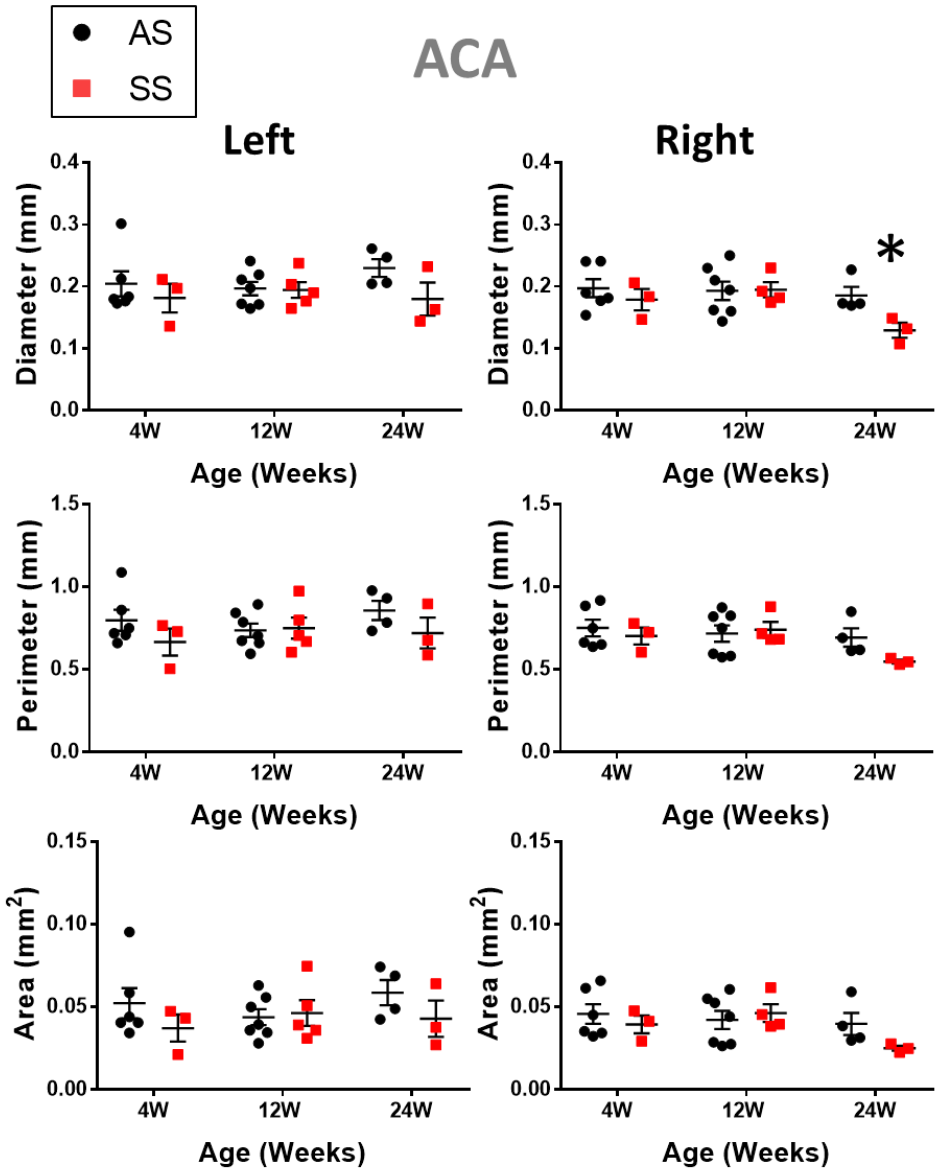

Figure 4.8.1: The morphology in the anterior cerebral arteries are similar between SS and AS mice.

The ACA does not significantly differ in size between AS and SS mice. At 24 weeks however, the right ACA in SS mice does tend to be smaller with diameters being significantly smaller. *$p < 0.05$ SS compared with AS by T-test. Error bars are SEM.

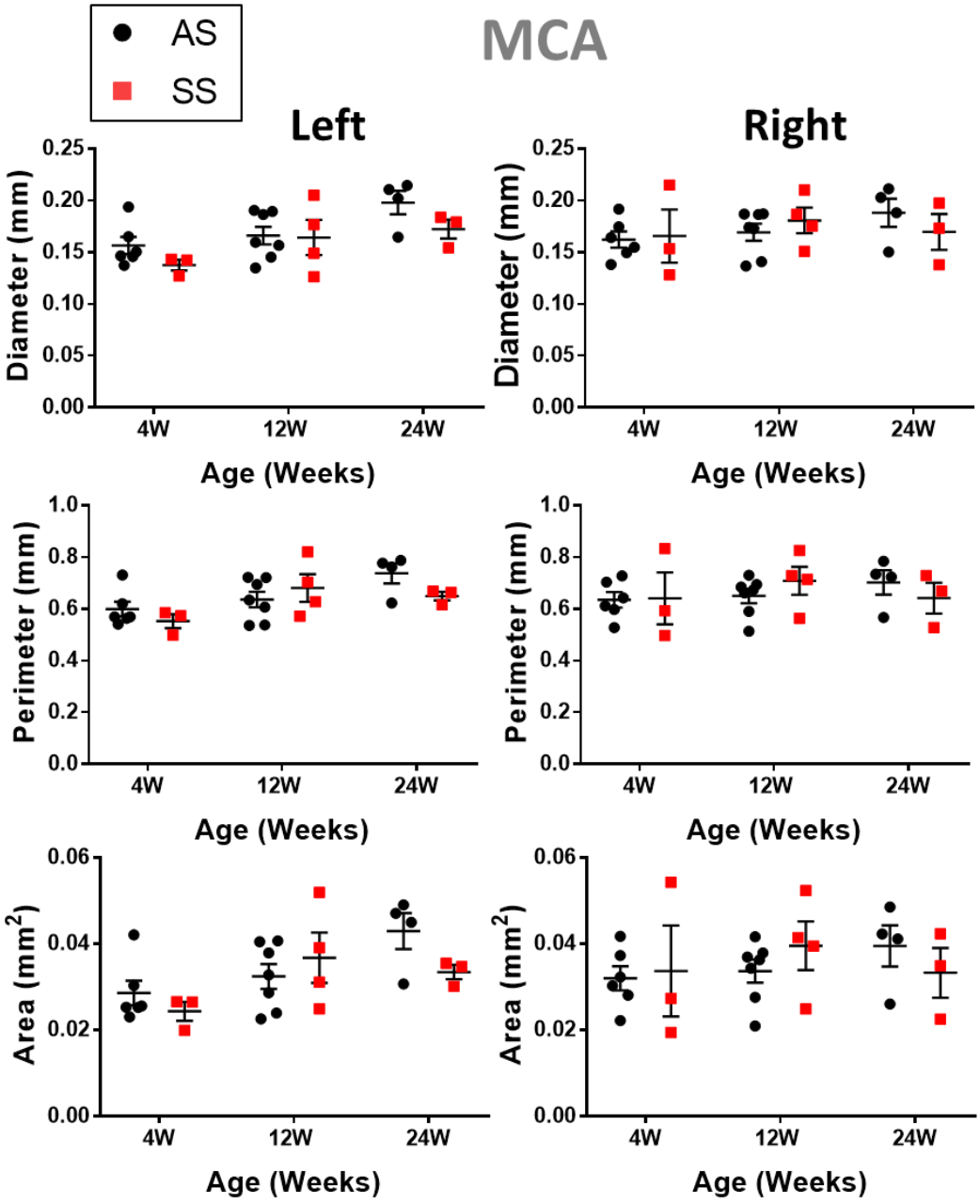

Figure 4.9.2: The morphology in the middle cerebral arteries are similar between SS and AS mice.

Morphology in the MCA is not affected by genotype as the diameter, perimeter, and cross-sectional area are not significantly different, regardless of age or side. *p < 0.05 SS compared with AS by T-test. Error bars are SEM.

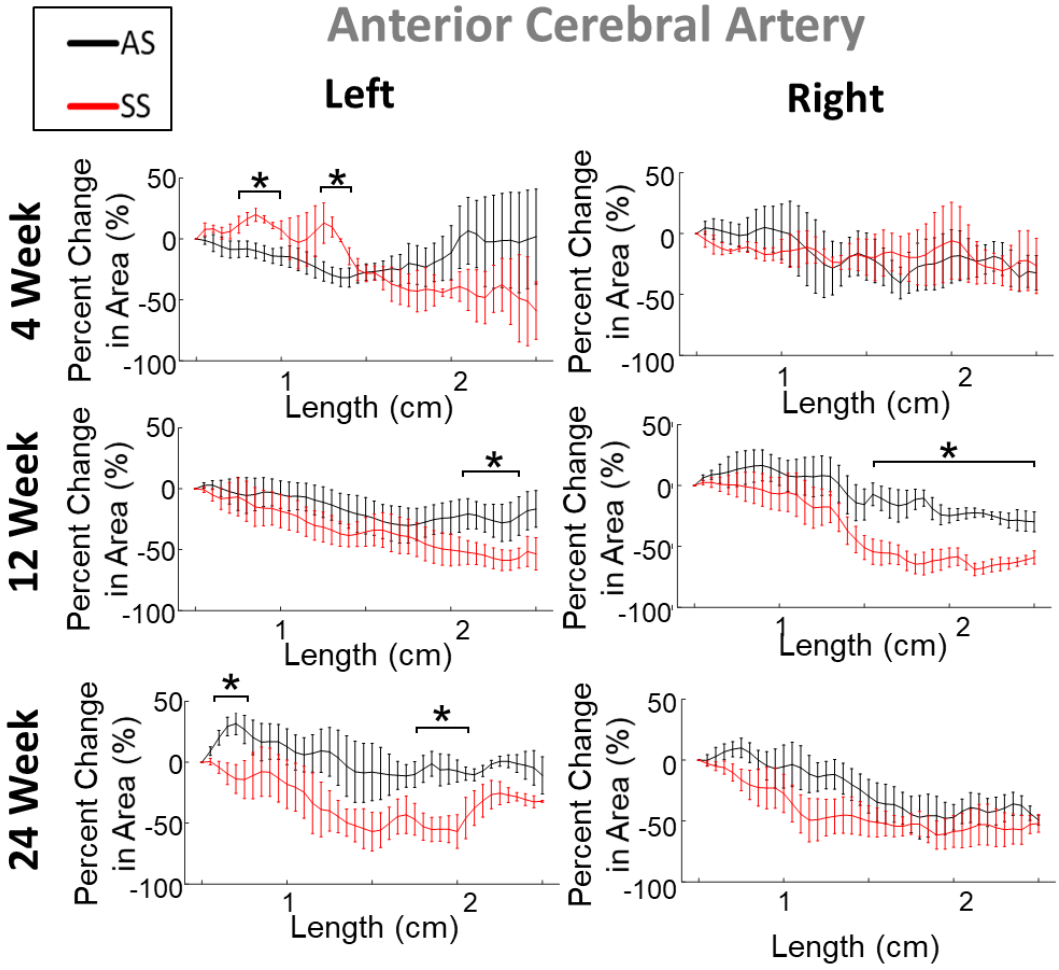

Figure 4.10: Portions of the anterior cerebral arteries are significantly narrower in SS mice.

Mean values of percent change in area are plotted along the length of the ACA. The left ACA is enlarged in 4-week SS mice. At 12 and 24 weeks the ACA of SS mice becomes narrowed at various portions of the ACA, in both the left and right sides. *p < 0.05 SS compared with AS by T-test. Error bars are SEM.

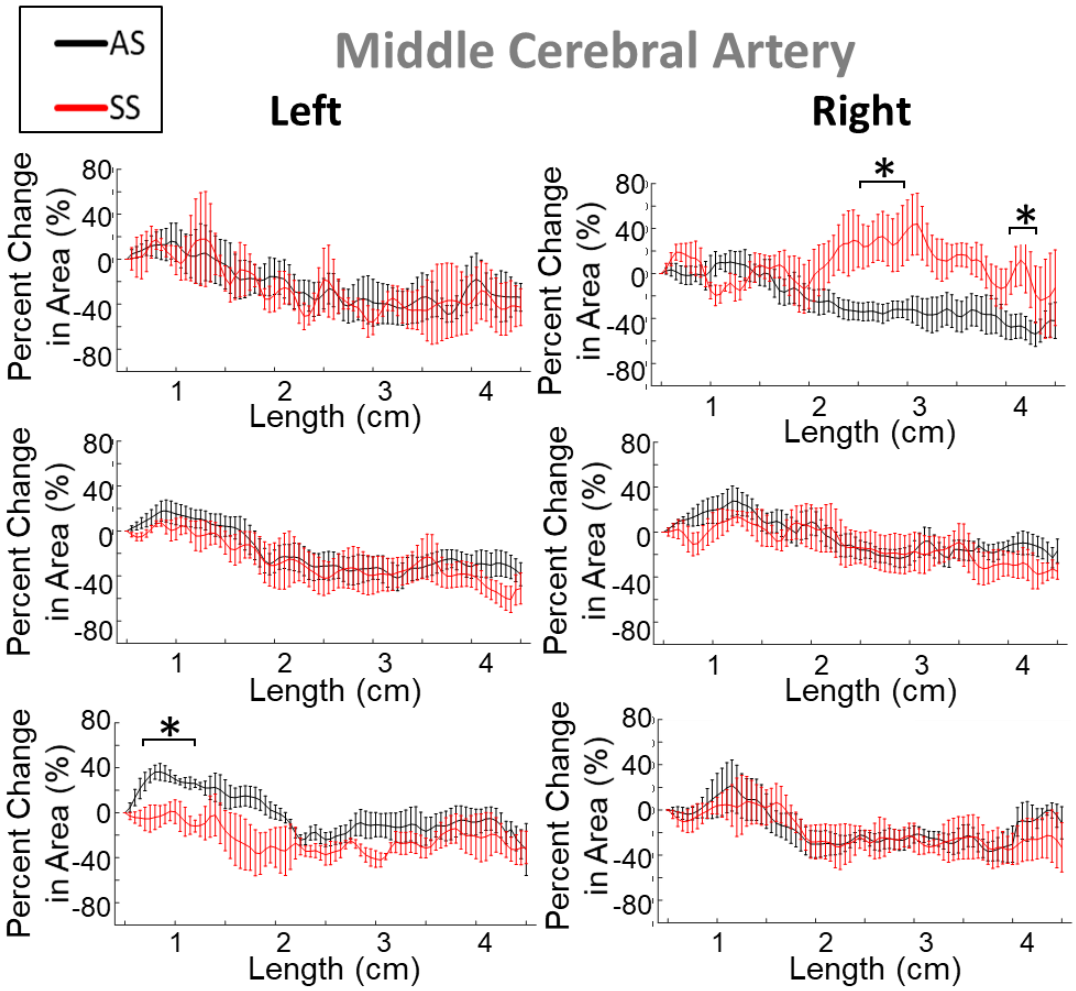

Figure 4.10: Portions of the anterior cerebral arteries are significantly narrower in SS mice.

Mean values of percent change in area are plotted along the length of the MCA. The right MCA is enlarged in 4-week SS mice, but this difference disappears as the mice age. The proximal section of the left MCA in 24-week SS mice is significantly narrower. *$p < 0.05$ SS compared with AS by T-test. Error bars are SEM.

Table 4.5: Morphological measurements from micro-CT analysis of the cerebral arteries in mice with sickle trait (AS) and sickle cell anemia (SS).

MCA	Left MCA						Right MCA					
	4		12		24		4		12		24	
	AS	SS	AS	SS	AS	SS	AS	SS	AS	SS	AS	SS
Diameter (mm)	0.147 (0.007)	0.136 (0.007)	0.16 (0.011)	0.155 (0.012)	0.187 (0.008)	0.163 (0.006)	0.158 (0.009)	0.161 (0.026)	0.161 (0.007)	0.171 (0.01)	0.182 (0.01)	0.162 (0.018)
Perimeter (mm)	0.61 (0.024)	0.57 (0.031)	0.617 (0.037)	0.647 (0.032)	0.773 (0.037)	0.657 (0.027)	0.682 (0.026)	0.677 (0.09)	0.626 (0.024)	0.673 (0.045)	0.763 (0.025)	0.651 (0.074)
Area (mm^2)	0.031 (0.003)	0.026 (0.003)	0.031 (0.003)	0.033 (0.004)	0.049 (0.005)	0.036 (0.004)	0.039 (0.003)	0.04 (0.009)	0.031 (0.002)	0.036 (0.005)	0.048 (0.003)	0.035 (0.008)
ACA	Left ACA						Right ACA					
	4		12		24		4		12		24	
	AS	SS	AS	SS	AS	SS	AS	SS	AS	SS	AS	SS
Diameter (mm)	0.218 (0.028)	0.177 (0.026)	0.194 (0.011)	0.198 (0.015)	0.218 (0.013)	0.192 (0.025)	0.193 (0.012)	0.185 (0.015)	0.19 (0.014)	0.194 (0.015)	0.186 (0.014)	0.138 (0.016)
Perimeter (mm)	0.888 (0.104)	0.756 (0.081)	0.797 (0.035)	0.895 (0.07)	0.88 (0.056)	0.862 (0.101)	0.848 (0.052)	0.754 (0.045)	0.784 (0.039)	0.807 (0.061)	0.787 (0.042)	0.632 (0.057)
Area (mm^2)	0.066 (0.017)	0.054 (0.003)	0.054 (0.004)	0.084 (0.024)	0.061 (0.007)	0.066 (0.014)	0.060 (0.008)	0.045 (0.005)	0.053 (0.005)	0.0556 (0.008)	0.054 (0.007)	0.036 (0.008)

MCA, Middle Cerebral Artery; ACA, Anterior Cerebral Artery. Standard error of the mean is shown in parentheses

[a] $p < 0.05$ compared with AS by T-test.

Number in parentheses is standard deviation of the measurement.

4.4 Discussion

Here we performed a cross-sectional study using a combination of ultrasound and micro-CT imaging to quantify and characterize morphology in the carotid and cerebral arteries at different ages of mice to examine differences between mice with sickle cell anemia (SS) or littermate heterozygous (AS) controls. Morphometric values calculated from micro-CT imaging of extracranial carotid artery casts paralleled measurements from the live mouse during systole. This suggest that morphometric values calculated in the cerebral arteries are within physiological norms. Significant differences found only through micro-CT in the extracranial ICA was a result of the greater resolution at which points can be measured. Through ultrasonography only a few distinct points can be measured in a vessel; however, using the reconstructed arteries multiple points can be analyzed along the length and averaged together. This reduces the overall error in the measurement. Additionally, the diameter measured from ultrasound is of a cross-section, and did not consider the irregular shape of the vessel. Measurements calculated through the reconstructed artery can provide area and perimeter, thereby quantifying the true shape of the vessel.

The greatest differences when examining the morphometric values were observed between AS and SS mice in the 12-week age group. The left common carotid artery diameter was larger in SS mice as measured through both ultrasound and micro-CT measurements. This result agrees with findings obtained by Cahill et. al, who compared the homozygous sickle Townes mice to C57BL/6J wild-type counterparts in 10 to 13-week-old mice [138] and also found SS mice to have significantly larger common carotid arteries measured via ultrasound. Extending downstream, the entire intracranial ICA was

significantly larger on the left side in SS mice 12 weeks of age. At 24 weeks however, only the proximal portion of the ICA was found to have significantly larger cross-sectional perimeters and areas. These results parallel findings in humans, as direct measurements via magnetic resonance angiography have shown luminal area to be larger in the ICA, ACA, and MCA of patients with SCD as compared to age matched controls [154]. Additionally, although there was a significant growth from 4 to 12 weeks; axially, ICA length was similar between SS and AS mice, and overall body weight showed no difference, matching previous studies [155]. Therefore, the radial differences observed in SS mice, is not due to differences in animal size but is a result of the animal genotype.

The larger luminal areas measured in SS mice may be an indication of vasodilation in order to generate higher cerebral blood flows. Reduced oxygen availability in SCA is compensated by elevated cerebral blood flow (CBF) to increase the rate of oxygen delivery [156, 157]. This is supported by a reduced cerebral vasculature reserve in humans and mice with sickle cell disease [37, 138, 158]. When subjected to hypoxic conditions the blood vessels in subjects affected by SCA are unable to dilate to the same extend as non-sickle cell controls, Therefore the change in cerebral blood flow is reduce in those with SCA. The enlarged lumens measured in the CCA and ICA of our SS mice could be attributed to this mechanism, and direct measurements of the luminal area in the cerebral arteries have also shown the ICA to be enlarged in humans with sickle cell disease [154]. It is important to note that both anesthetics used in this study, isoflurane for the ultrasound procedure and urethane for the perfusion casting of the arteries, are both vasodilators [159, 160]. Therefore, the morphological differences between AS and SS mice maybe even larger in the proximal internal carotid artery under normal physiological conditions.

In the distal intracranial ICA, however, a distinct narrowing was observed which led to a loss of the statistically significant difference between SS and AS mice at 24-weeks of age. This narrowing was quantified by normalizing the area to the most proximal point of the artery and plotting the percent change in area against length. Through this method we can see that the ICA was significantly narrower at certain portions of the distal ICA, in right and left sides of 12 and 24-week week old mice. Using this method again, significant narrowing occurred in the ACA of SS mice (Fig 9), despite seeing no significant differences in the morphometric properties, with the exception of the ACA diameter being smaller in 24-week SS mice. This narrowing in luminal area in SS mice suggests a potential for hemodynamic changes as well. Elevated blood velocities are known to occur in the presence of stenoses cerebral arteries, and high cerebral blood velocities have been associated with stroke risk in with sickle cell anemia[4, 28, 50]. Therefore, the narrowing observed in these mice with SCA could also produce elevated blood velocities

Reduction in normalized area in the ICA and ACA of SS mice could be associated with vascular remodeling. Cerebral angiograms of individuals who have suffered from strokes have shown that the occurrence of stenotic lesions in the cerebral arteries [4, 5]. Characterization of these stroke lesions have shown remarkable vascular remodeling characterized by intimal hyperplasia [5]. Additionally, increased cellular adhesion of leukocytes and erythrocytes in sickle cell anemia may also contribute to the observed luminal narrowing [29, 103, 161]. While this is mostly observed in the microvasculature others have shown that monocytes and red bloods cells can adhere in the large arteries as well [28, 103]. Determining the pathological mechanisms for this luminal narrowing may help in developing therapeutics for preventing strokes.

Differences between AS and SS were mostly observed in the 12-week age group. Age is known to be a strong factor of stroke risk in sickle cell anemia, with the highest risk of ischemic stroke occurring between the ages of two and five in humans [33]. Ages of mice do not correlate linearly to human age, as maturation in the first month of life occurs 150 times faster and later months have a third of the previous maturation rate [162]. Approximations can be made to compare mouse lifespans to clinical pathologies in humans with sickle cell at certain ages. At four weeks, mice are in early adolescence (approximating humans of 10-12 years old), while at 12 weeks mice approximate humans in their early 20s. At 24 weeks, the mice approximate humans in their early 30s. Individuals with SCA in their 20s have an elevated risk of hemorrhagic stroke [52]; the bulk morphometric differences observed in 12-week mice may be related to this type of stroke. Though no aneurysms were found in the mice themselves, uncontrolled expansion of the artery can lead to hemorrhagic stroke. At 24 weeks of age, mice approximate the age of humans in their 30s, and this is the age at which humans with SCA have an elevated risk of ischemic stroke [52]. The narrowing observed in the cerebral arteries of mice with SCA could potentially cause a stroke as blockages in these narrowed sections of the artery may prevent an adequate supply of blood and oxygen.

The left common carotid and internal carotid artery lumens were larger in SS mice compared to AS mice. The cause for these differences is not fully known. It has been previously reported that the hippocampus, thalamus, and visual cortex on the left side of the brain in C57BL/6J mice, one of the background strains for the Townes mice, are enlarged [163]. These regions are supplied by several arteries that branch from the ICA and may have higher oxygen demands than their counterparts on the right. This could

potentially be magnified in a mouse with sickle cell anemia, leading to the larger artery size that was observed.

This study has important limitations. Some age groups had as few as three mice per genotype, which limits our ability to generalize these results. We can therefore only draw conclusions regarding differences in vessel morphology across genotypes but not within the genotypes themselves. The Townes sickle transgenic mouse model are a clonal strain therefore there should be little variation within a single genotype. The precision of the measurements in the cerebral arteries are limited by variations in the perfusion casting and image resolution. To maximize reproducibility of our results we monitored the pressures used during the casting produce and perfused under physiological pressures of 100–120 mmHg [152, 153]. Additionally, during reconstruction of the cerebrovascular arteries, the same protocol was applied to each specimen to reduce inconsistency. Individuals were blinded during reconstruction, and the finalization of the model was performed by the same individual.

In conclusion, this cross-sectional study characterizes morphological characteristics in the carotid and cerebral arteries of SS and AS mice from ages 4 – 24 weeks. Casting of the arteries corresponds to *in vivo* measurements and provides information in regions of the vasculature that cannot be easily imaged with other modalities in mice. Morphological differences between genotypes were found to occur in 12- and 24-week mice, coinciding with the different types of strokes that are most prevalent in humans with SCA. This suggests that SCA affects the vascular morphology, continually changing the cerebrovascular system through the entire lifespan of the subject, whether mouse or human. Through quantification of the morphometric values it may be possible to predict

the type and likelihood of stroke in an individual with SCA. Future work is needed to determine the cause of these morphological changes, and ultimate consequences they produce.

CHAPTER 5 COMPUTATIONAL FLUIDIC DYNAMICS SIMULATION OF HEMODYNAMIC ABNORMALITIES IN THE CEREBROVASCULATURE OF MICE WITH SICKLE CELL ANEMIA

5.1 Introduction

Sickle cell anemia (SCA) is one of the most prevalent blood disorders afflicting millions globally. Amongst the morbidities associated with SCA, ischemic strokes occur at an abnormally high rate in children. Individuals with SCA have more than an 11% chance of developing overt strokes before the age of 20[3, 33]. Currently, the only method to determine stroke risk is through transcranial doppler (TCD), which is used to measure elevated blood velocities in cerebral arteries. When blood velocities in either the intracranial internal carotid (ICA), middle cerebral (MCA), and/or anterior cerebral arteries (ACA) exceed a time-average maximum-mean velocity (TAMMV) of 200 cm/s, an individual with SCA is classified as high stroke risk [1, 40, 41]. Several studies have shown the presence of large stenoses, via angiograms, in the cerebral arteries of individuals with elevated blood velocities [28, 43]. However elevated cerebral blood velocities can still occur in the absence of stenoses [51]. Therefore, the pathophysiology responsible for elevated blood flow in those with SCA at risk for stroke is not fully understood.

Mouse models offer a powerful tool for investigating the effect of genetic diseases on the cerebrovasculature. Atherosclerosis [3,4], stroke [5,6,7], aneurysms [8,9], are amongst several cerebrovascular pathologies being investigated in mice. The humanized Townes sickle cell transgenic mouse model is commonly used in the area of sickle cell research. Null for murine α, and β-globin genes and it contains knock-in genes that produce

human hemoglobin genes (α, β, and γ), including the β-globin S mutation [135]. Specifically, the Townes sickle mouse has been beneficial for investigating pulmonary and hematological pathophysiology, but a few studies target cerebrovascular research [135-137]. Characterization of the hemodynamics in the carotid and cerebral arteries is incomplete and it is unknown if the abnormal cerebral blood velocities observed in humans with SCA carry into the murine model. Therefore, characterizing the cerebral vasculature of the Townes mouse model is crucial to investigating sickle mediate strokes, and testing future pharmacological therapeutics.

High-frequency ultrasonography has been used to measure velocities in the carotid arteries of mice, however, obtaining accurate measurements in the cerebral arteries, has proven to be more difficult. This is due to a combination of the smaller vessels that comprise these arteries in addition to the shielding created by the skull. To overcome this deterrent, computational fluid dynamics (CFD) can be used to approximate cerebral blood velocities. CFD has often been used as a tool in the cardiovascular system to determine the hemodynamics in regions where traditional tools are ineffective, and thus can be used to investigate the biological processes that are occurring. Wall shear stress (WSS) and oscillatory shear index (OSI) [7, 8] are two hemodynamic parameters that play an important role in the pathogenesis of atherosclerosis. WSS acting on the endothelium surface is an important determinant of endothelial function and phenotype [8]. Additionally, Cheng et al. assessed the effect of in vivo alterations of shear stress on the development of atherosclerosis in apoE-deficient mouse and concluded that low WSS and OSI are both essential conditions in plaque formation [13].

The goal of this study is to examine the cerebrovascular hemodynamics in homozygous sickle cell (SS) mice at varying ages. Age is known to be a strong factor of stroke risk in sickle cell anemia, with the highest risk of ischemic stroke occurring between the ages of 2 and 8 [33], and decreases until the third decade of life whereupon risk begins risk again [52]. Therefore, it is important to determine the age-related morphometric changes that are occurring in the cerebral vasculature of the Townes mouse model, and how these changes relate to stroke risk.

To investigate cerebral blood flow in the Townes sickle cell mouse model, we use a combination of ultrasonography followed by casting in the carotid and cerebral arteries [150] to obtain boundary conditions for a CFD model based on the finite element method. The model was validated by comparing simulated extracranial ICA values to ultrasound measurements. Subject-specific blood flow was simulated in the ICA, MCA, and ACA of mice with sickle cell anemia in order to characterize the hemodynamics and approximate the velocity. Twelve-week SS mice were found to have higher TAMMV in the cerebral arteries as compared to heterozygous (AS) littermate controls. Additional simulations using the same inlet boundary condition for all samples, revealed significant hemodynamic differences between SS and AS mice were due to morphological differences. Together this work characterizes age-dependent hemodynamic changes in the carotid and cerebral morphology of the Townes transgenic and enables further investigation of sickle-mediated strokes.

5.2 Methods

5.2.1 High Frequency Ultrasonography

A VEVO 2100 Doppler system (VisualSonics, Toronto, ON, Canada) with a 22-55 Mhz transducer (MS550D, wavelength ~50 µm – 2 mm), was used to measure the blood velocities in the common carotid (CCA) and extracranial internal carotid arteries (eICA). Mice were anesthetized with 5% isoflurane and maintained at 1% on a horizontal platform in the supine position. Afterwards, hair was then removed from the neck and pectoralis, before ultrasound gel (Aquasonic, Parker Laboratories) was applied to improve signal acquisition. The ultrasound beam applied perpendicular to the arteries. The carotid bifurcation, which consist of the distal CCA, eICA, and external carotid artery (ECA), was identified in B-mode based on depth from the surface of the skin, direction of flow, and spatial orientation. In M-mode the velocity spectrum was recorded in the CCA (~1mm upstream of the carotid bifurcation), and in the extracranial ICA (~0.5 mm downstream of the carotid bifurcation) (Figure 5.1). The sample area was adjusted to encompass the entire lumen and have the smallest intercept angle to the direction of flow. This process was performed in the left and right sides and optimized to display the highest velocity and sharpest waveform possible for each artery before being recorded.

Mean waveforms from the velocity spectrum across 5-8 cardiac cycles were digitized using GetData and imported into a custom Matlab script (Appendix 2) to extract hemodynamic values. Briefly, velocities profiles were interpolated using a polynomial function to obtain a constant time step of 0.05 ms. Individual waveforms corresponding to one cardiac cycle were then identified and overlaid on top of each other, to calculate a time-average waveform (Figure 5.1B).

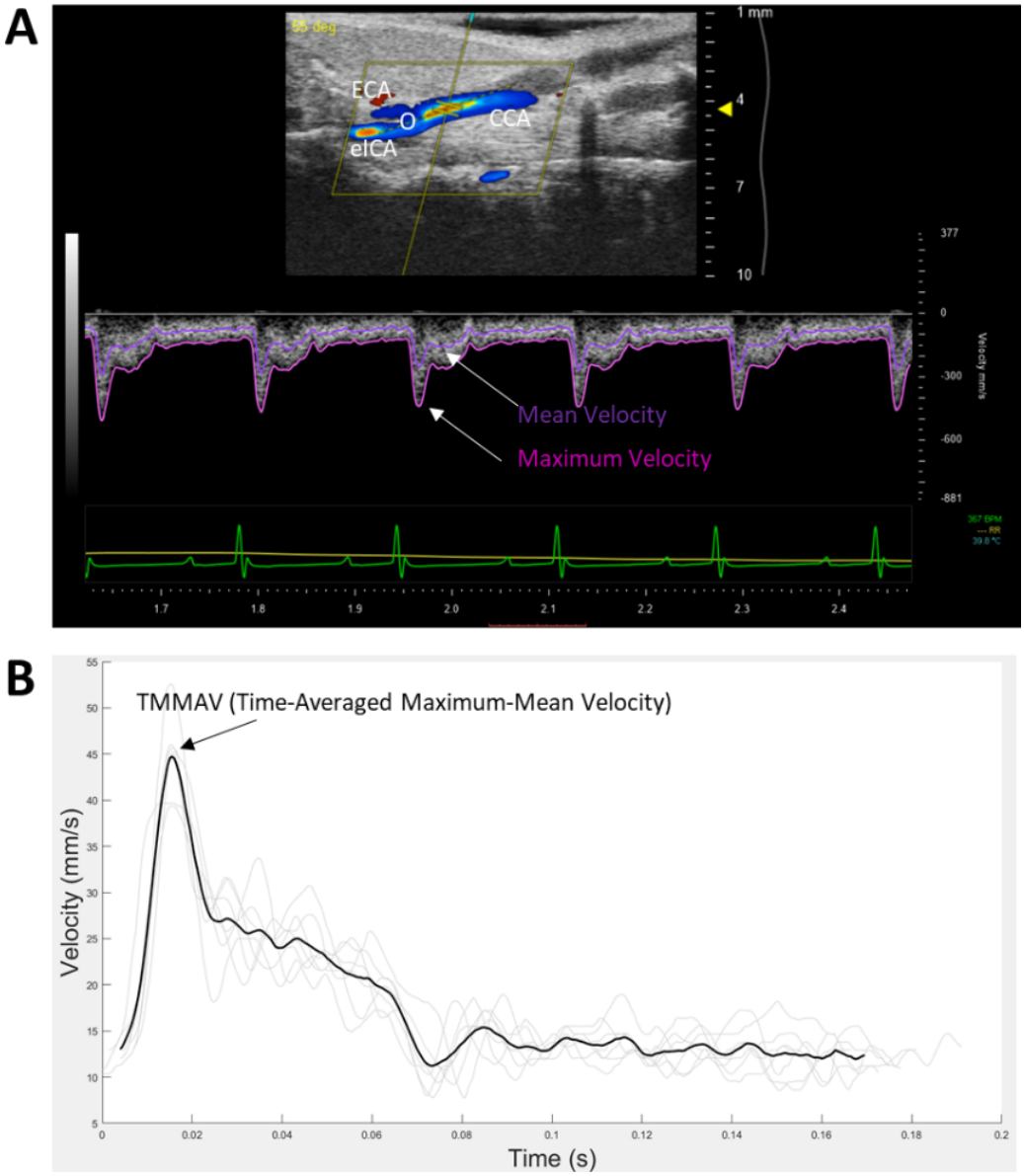

Figure 5.1: Quantification of time-averaged hemodynamic parameters.
(A) The blood velocity was obtained in the CCA ~1mm upstream of the common carotid bifurcation (labeled O), and in the eICA ~0.5mm downstream of the carotid bifurcation. The mean value of the velocity spectrum (purple line) was used for all analyses. The green line is heart rate. Ultrasound image was enlarged for clarity **(B)** The time-averaged hemodynamic parameters were obtained by identifying individual component waves and overlaying them on top of each other (grey lines). The individual waves were averaged to generate a time-averaged velocity profile (black line). Peak systolic velocity (PSV) is the highest peak of the average waveform, and the end diastolic velocity (EDV) is the velocity at the end of the cardiac cycle.

5.2.2 Perfusion Casting

Following ultrasound measurements, each mouse recuperated for 6-24 hours before being prepared for micro-CT [150]. Briefly, mice were anesthetized with urethane at a dose of 1g/kg, and laparotomy was performed to gain access to the abdominal aorta, where a 24-gauge catheter was used to make a direct puncture and held via sutures. An incision was created in the vena cava to provide an exit point for blood, whereupon a heparinized saline solution (25 U/mL) was injected through the catheter at a pressure of approximately 120 mmHg, the systolic pressure in mice [152, 153]. Pressure was monitored using a sphygmomanometer, and the heparinized solution was perfused through the mouse until the effluent at the vena cava became clear. Following exsanguination, a 10% solution of buffered formaldehyde was perfused through the catheter for 15 minutes at a pressure of 120 mmHg to fix the blood vessels. Afterwards, 5 mL of Microfil HV 122 Yellow (Flow Tech, Carver, MA) was manually perfused. Following the procedure, the upper torso of the mouse, including the head, was detached and stored in 10% buffered formaldehyde for 5 days before undergoing decalcification in 10% HCl for 48 hours. After decalcification, each mouse was again stored in 10% buffered formaldehyde, until undergoing micro-CT.

5.2.3 Micro-Computed Tomography

The carotid and cerebral arteries were examined using a high-resolution micro-CT imaging system (Quantum GX, Perkin Elmer). During the day of the examination, mouse heads were placed in a specimen tube (diameter 30.7 mm) in the prone position with the long axis of the head parallel to the tube's long axis. Examination of the brain was performed by scanning in the transverse plane with micro-CT images of the head taken over a 4-mm thick section extending from the nose to the back of the neck. All scans were

performed with a beam intensity of 80 microamperes, a beam energy of 70 kV, and an isotropic voxel resolution of 50 um.

5.2.4 Segmentation and Reconstruction of Carotid and Cerebral Arteries

Micro-computed tomography images were used to create 3D models of the carotid arteries for each specimen. Mimics Materialise 15.*0* (Leuven, Belgium), was used to manually segment and reconstruct the left and right arteries, extending from the common carotid arteries to the middle cerebral and anterior cerebral arteries (Figure 5.2). A minimum threshold was optimized for each specimen, which produced the largest vessel diameter without creating large irregularities on the surface. After a threshold was chosen, a preliminary mesh of the vascular network was created, containing arterial segments of the CCA, ECA, ICA, ACA, and MCA. The internal carotid artery is divided into two sections the extracranial internal carotid artery (eICA) and intracranial internal carotid artery (ICA). The intracranial ICA was defined as the section downstream of the ophthalmic artery branch. In order to remove any artifacts created from the reconstructive process, re-meshing and smoothing algorithms from Vascular Modeling Toolkit *(VMTK)* were applied to the model. After reconstruction, Mimics was used to calculate diameter along the length of each arterial segment.

The reconstructed arteries were separated into two sections: (1) the common carotid bifurcation (CCA, eICA, and ECA), and (2) the intracranial internal carotid bifurcation (ICA, MCA, ACA) (Figure 3). Flow extensions with a length equal to 4 times the corresponding inlet or outlet diameter was added to the model in order to ensure the fluid flow entering and exiting the system was undisturbed and parabolic. The final mesh used for simulations was created in the 3D tetrahedral mesh generator, Netgen.

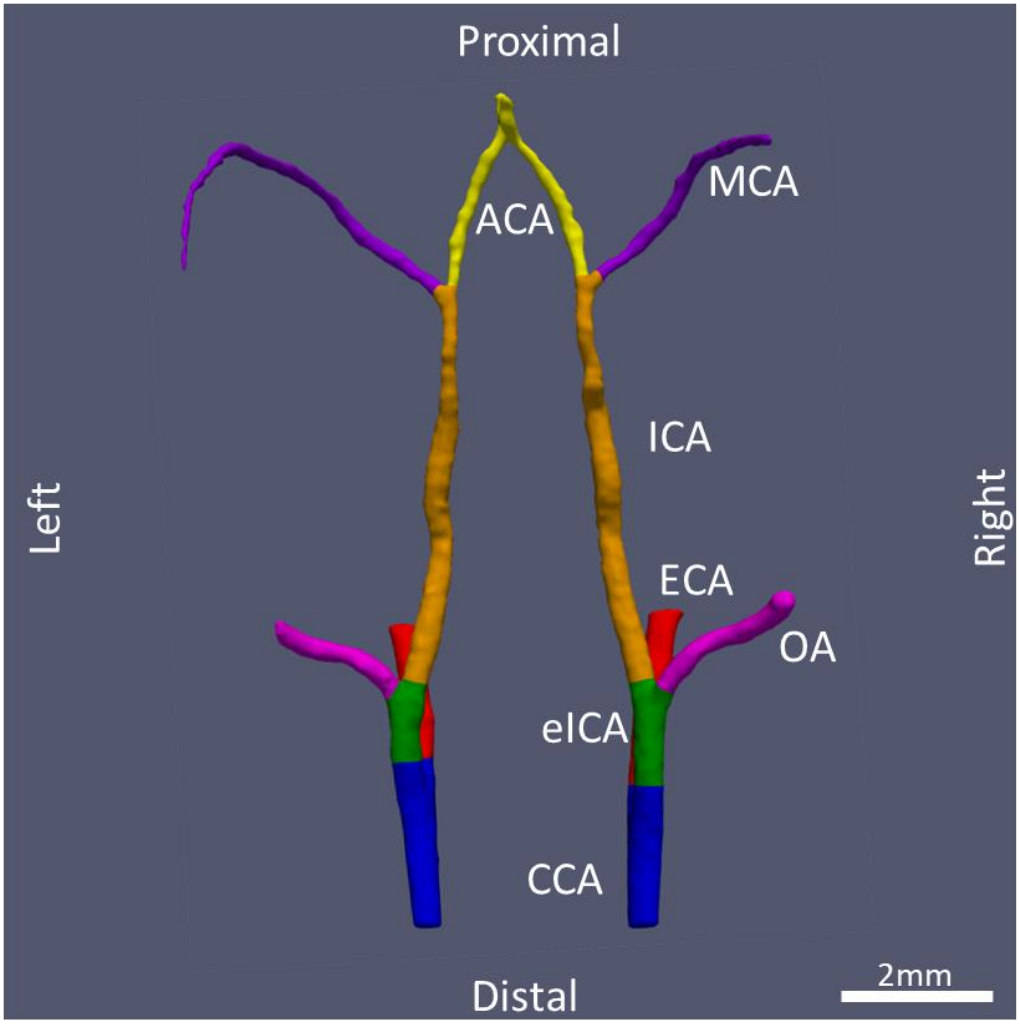

Figure 5.2: Carotid and Cerebral Artery Model of a Sickle Transgenic Mouse.
Reconstruction of the carotid and cerebral arteries segmented from micro-computed tomography images of perfusion casted vessels. CCA (common carotid artery), ECA (external carotid artery), eICA (extracranial internal carotid artery), OA (ophthalmic artery), ICA (intracranial internal carotid artery), MCA (middle cerebral artery), ACA (anterior cerebral artery).

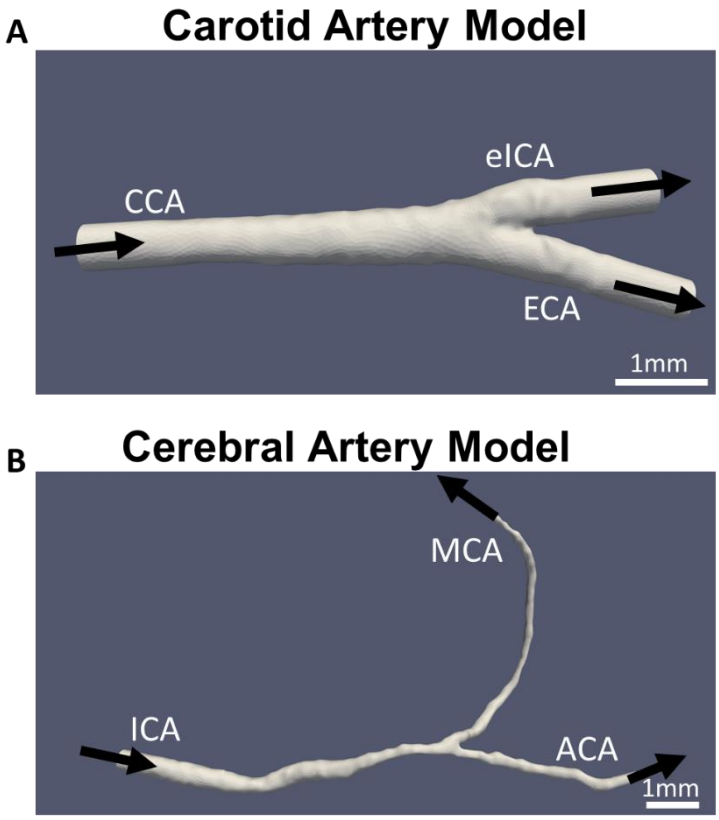

Figure 5.3: Partitioning of carotid and cerebral arteries for computational fluid dynamic simulations.
The reconstructed arteries were divided into two segments for finite element analysis. **(A)** The carotid artery system containing the CCA, eICA, and ECA was primarily used to validate the computational model. **(B)** The cerebral artery system contains ICA, MCA and ACA. Flow extensions were added to ensure the fluid flow entering and exiting the system was undisturbed.

5.2.5 Computational Fluid Dynamic Model

The finite element method was used to simulate blood flow in both arterial systems. Meshes were imported into LifeV, an open source Object Oriented C++ Finite Element solver developed as a joint initiative of Department of Mathematics at EPFL, Lausanne CH, Department of Mathematics at Politecnico di Milano, Milan, IT and the Department of Mathematics and Computer Science at Emory University, Atlanta (GA) USA [16].

The incompressible continuity equation (Eq. 5.1) and the Navier-Stokes equations for momentum (Eq 5.2) functioned as the governing equations and were applied to the region of the model delimited by the inlet, outlets, and walls of the vascular tree.

$$\nabla \cdot v = 0 \text{ (Equation 5.1)}$$

$$\rho \frac{D\boldsymbol{v}}{Dt} = \nabla P + \mu \nabla^2 \boldsymbol{v} \text{(Equation 5.2)}$$

Vessel walls were assumed to be rigid, and the no-slip condition was applied causing the velocity at the wall to be zero. Additionally, hydrostatic effects were assumed to be negligible and fluid was considered as a Newtonian and incompressible. The fluid was assumed to have the same properties of mouse blood with a density of 1057 kg/m^3 and viscosity of 4.879 cP [44, 88, 89].

At the inlets, a time-averaged velocity waveform calculated from the ultrasound measurements was applied for each individual animal. In the common carotid model, the exact waveform was applied to the CCA inlet. In the internal carotid artery, Murray's Law (Eq. 5.3) was used to approximate a flow split from the upstream eICA to the downstream intracranial ICA as some of the blood flows into the ophthalmic artery [164-166].

$$\frac{D^3_{downsteam}}{D^3_{upstream}} = \frac{\dot{V}_{downstream}}{\dot{V}_{upstream}} \text{(Equation 5.3)}$$

Where D is vessel diameter and ($\dot{V}$) is the volumetric flow rate through the vessel.

Simulations were performed in 4 and 12-week mice for both the left and right sides at a time step of 0.0005s across three cardiac cycles. Since each specimen had their own unique velocity profile, the total time varied.

Prior to the actual simulation the velocity entering the system was slowly ramped-up for several fictions time steps prior, until it matched the actual velocity waveform. This was done to avoid potential instabilities created from mismatches in the inlet boundary and initial conditions.

At the outlets a three-element Windkessel model consisting of a resistor in series with both a capacitor and resistor in parallel was utilized (Fig. 5.4). This was done to produce a pressure gradient and relate the outgoing artery velocity to the pressure of the outlet. The first resistor (R_1) represents the respective resistance of the outgoing artery; and the capacitor (C) and the second resistor (R_2) signifies the total compliance and resistance of all peripheral vessels to the outgoing artery. Outflow pressure is calculated based on outflow velocity and predetermined resistances and compliances of the vessel. Variables for the listed equations are defined as follows: density (ρ), inviscid wave speed or pulse wave velocity (c_i), viscosity (μ), length (L), radius (r), volume (V), and pressure (P).

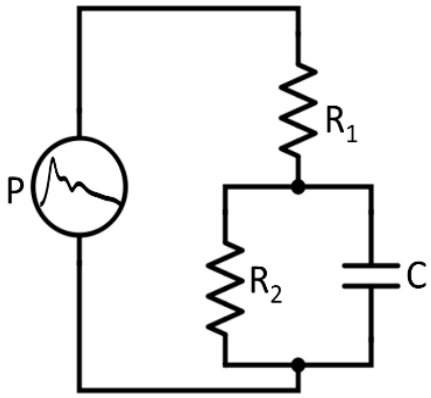

$$R_1 = \frac{\rho c_i}{\pi}\left(\frac{1}{r^2}\right) \text{ (Equation 5.4)}$$

$$R_2 = \frac{8\mu}{\pi}\left(\frac{L}{r^4}\right) \text{ (Equation 5.5)}$$

$$C = \frac{\Delta V}{\Delta P} \text{ (Equation 5.6)}$$

Figure 5.4: Three Element Windkessel Model
Schematic of a three element Windkessel model and the defining equation for the individual elements. The Windkessel is used to relate pressure and flowrate in the cardiovasculature using a system of resistances and compliances.

Peripheral resistance (R_2) can be approximated from the geometry of the outlet vessel (Eq 5.4), therefore the resistance at each outlet (ECA, eICA, MCA, and ACA) was estimated from calculated values of diameter and length. Calculating R_1 and C are more difficult as both pulse wave velocity (Eq 5.5) and change in vessel volume (Eq 5.6) could not be measured directly. Therefore, scaling laws were used to approximate these variables. While the classical impedance of a vessel is defined as the change in volume over the changed in pressure from systole to diastole, impedance can also be estimated from the pulse wave velocity (Eq 5.7) [167] using the following equation:

$$C = \frac{V}{\rho c_i} \text{ (Equation 5.7)}$$

Where ρ is density of blood, and V is the volume of the vessel, which can be approximated by assuming a cylindrical shape. Therefore, both R_1 and C can be estimated through scaling of pulse wave velocity. In work published by Aslanidou et. al., they were able to derive an equation (Eq 5.8) relating pulse wave velocity to lumen diameter in C57BlL/6 mice one of the background mice used in creating the Townes mouse model [168].

$$c_i = \frac{0.3693}{d^{0.3359}} \text{(Equation 5.8)}$$

To validate the model and ensure that the values for resistance were correct the common carotid artery model was used. Simulated values in the extracranial ICA were compared to the actual ultrasound measurements. The simulations were ran in parallel among 8 processors, which were afterwards compiled together using a script developed in $C++$. Visualization and analysis of the data from the simulation was completed in

Paraview. Only the third and final cardiac cycle was analyzed to avoid potential instabilities that might have occurred in earlier time steps. The TAMMV was calculated in each artery by taking a cross-sectional slice in each arterial segment at location at which velocity was highest.

.

5.2.6 Statistical Analysis

All statistical tests were performed in Graphpad Prism 7. Data was plotted across age, and data from each group of animals are reported as the mean ± standard mean error. A value of $p < 0.05$ was taken to be significant. The effect of genotype was examined using unpaired T-test. [4 weeks $n_{AS} = 6$, $n_{SS} = 3$), 12 weeks ($n_{AS} = 7$, $n_{SS} = 4$), 24 weeks ($n_{AS} = 4$, $n_{SS} = 3$)].

5.3 Results

5.3.1 Time-average maximum-mean velocities are similar in the carotid arteries of AS and SS mice

Doppler ultrasound revealed TAMMV in the common carotid artery was similar for AS and SS mice at all age groups ($n = 3\text{-}7$, $p > 0.05$) (Fig 5.5A). This pattern extended downstream into the extracranial ICA where no significant differences were found between the two genotypes ($n = 3\text{-}7$, $p > 0.05$). At 12 weeks however, AS mice had slightly elevated velocities compared to their SS counterparts (23.17 ± 2.12 cm/s vs 15.78 ± 3.69 cm/s in the left CCA) and (15.79.17 ± 2.28 cm/s vs 11.42 ± 0.92 cm/s in the left CCA).

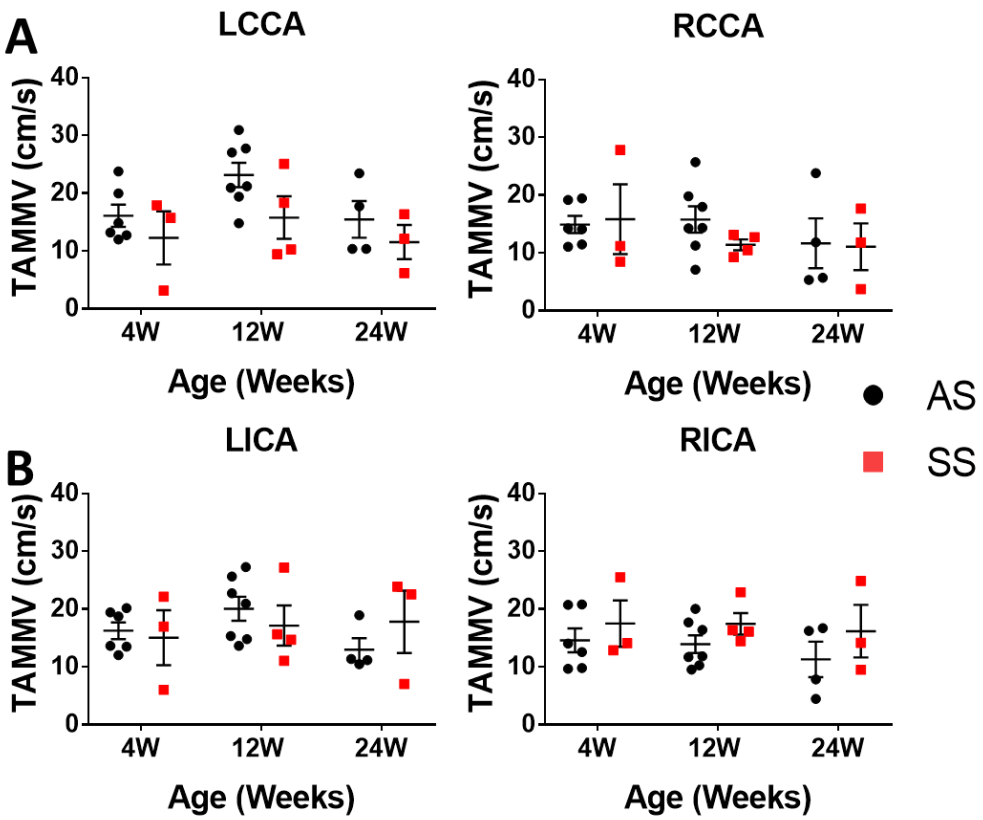

Figure 5.5: Velocities in the carotid arteries are similar between SS and AS mice
The mean of the velocity spectrum from 5-8 cardiac cycles in the CCA and eICA were averaged together to obtain a time-averaged mean waveform for each mouse, where upon the time-average maximum-mean velocity (TAMMV) was calculated. The TAMMV was not significantly different between in AS and SS mice at any age in either the common carotid **(A)** or extracranial internal carotid artery **(B)**. *$p < 0.05$ SS compared with AS by T-test. Error bars are SEM.

5.3.2 Computational fluid dynamic simulations can recapitulate *in vivo* ultrasound measurements in the carotid arteries

The carotid artery system was used to validate the computational model. Subject-specific simulations were performed such that the CCA waveform measured in a mouse was paired and used as the inlet velocity for that specific same mouse's geometry. Blood flow were simulated in 5 12-week AS mice, using the conditions previously described. Velocities were analyzed at cross-sections taken from the CCA and eICA. As expected, the inlet CCA velocity prescribed to the system perfectly matched the corresponding ultrasound measurements from which it was derived (Fig 5.6). Velocities in the eICA varied from the exact ultrasound measurement but the TAMMV did not differ by more than 30% in any of the samples. A comparison between simulated and ultrasound TAMMV in the eICA reveals no significant differences between the groups ($p > 0.05$).

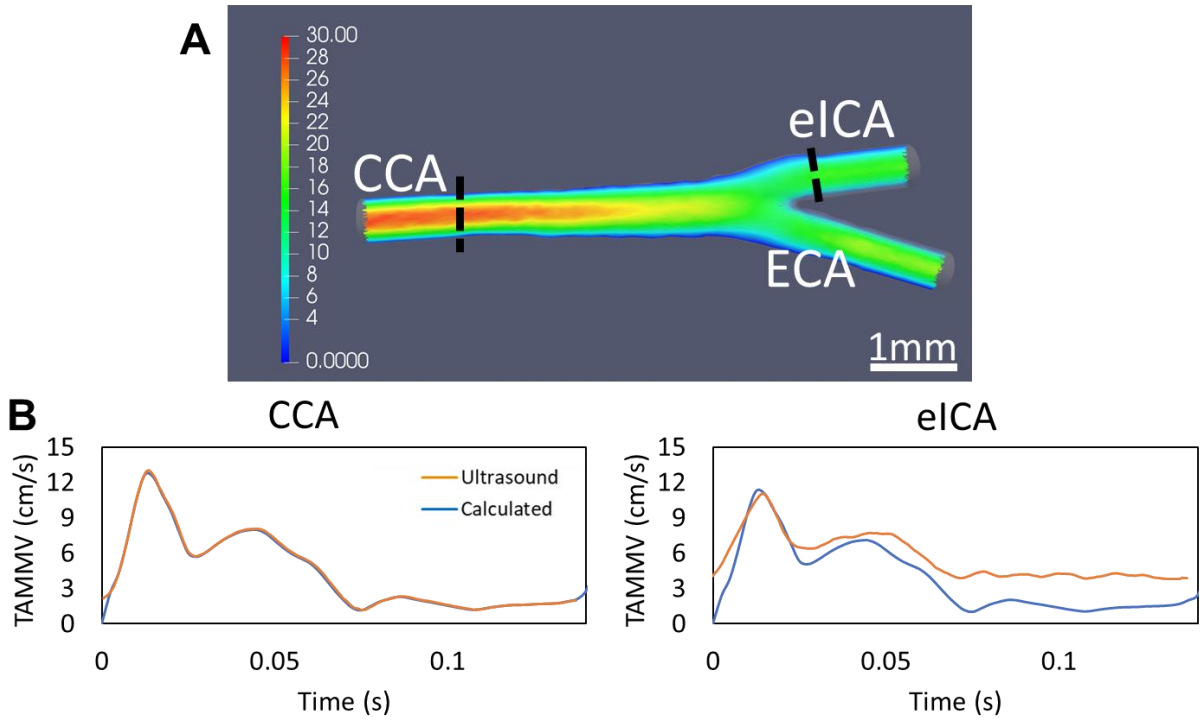

Figure 5.6: Simulated model flow velocity compared to *in vivo* ultrasound measurements.
(A) Blood flow was simulated in the carotid artery model. Cross-sections (dotted line) were taken from the CCA and eICA to determine the mean velocity profiles. **(B)** Representative figures of the mean velocity profiles in the CCA and eICA calculated from the simulation. The mean velocity in the CCA exactly matches the ultrasound measurement from which it was derived. There are some differences between the simulated eICA velocity and the ultrasound measurement.

5.3.3 Time-average maximum-mean velocities in subject-specific simulations are slightly elevated in SS Mice

Subject-specific CFD were performed using the cerebral artery model in order to estimate the velocities in the key arteries associated with stroke. Examining the velocity streamlines during systole, reveals cerebral velocities to be elevated in SS mice at 12 - weeks of age (Fig. 5.7). In order to quantify the differences that were visually observed, a technique was applied similarity to how TAMMV is reported clinically. While performing TCD on individuals with SCA, multiple measurements are made in the ACA, MCA, and ICA in both the left and right sides; and only the highest velocity is reported [36]. Therefore, using this method as a basis, each artery was examined separately for each animal, such that TAMMV was only calculated at the location in vessel where it was the highest. For analysis in the whole brain, only the highest TAMMV amongst all the cerebral arteries in an animal was used (Fig. 5.8A). Simulations revealed TAMMV in 4W mice were similar for AS (58.18 ± 7.14 cm/s) and SS mice (84.14 ± 36.23 cm/s) ($p > 0.05$). At 12 weeks, a trend towards elevated TAMMV was observed in SS mice (139.01 ± 59.15 cm/s) as compared to AS mice (54.13 ± 59 cm/s) ($p < 0.1$). Standard error was greater in the SS mice, indicating greater variance. When examining all the cerebral arteries separately, elevated TAMMV in the 12-week age group to be localized to the right ACA (Fig 5.8B). Two mice in this group had particularly high velocities (298.87 cm/s and 158.2 cm/s). An elevated velocity of 156.53 cm/s was also found in the right ICA of a 4W SS mouse.

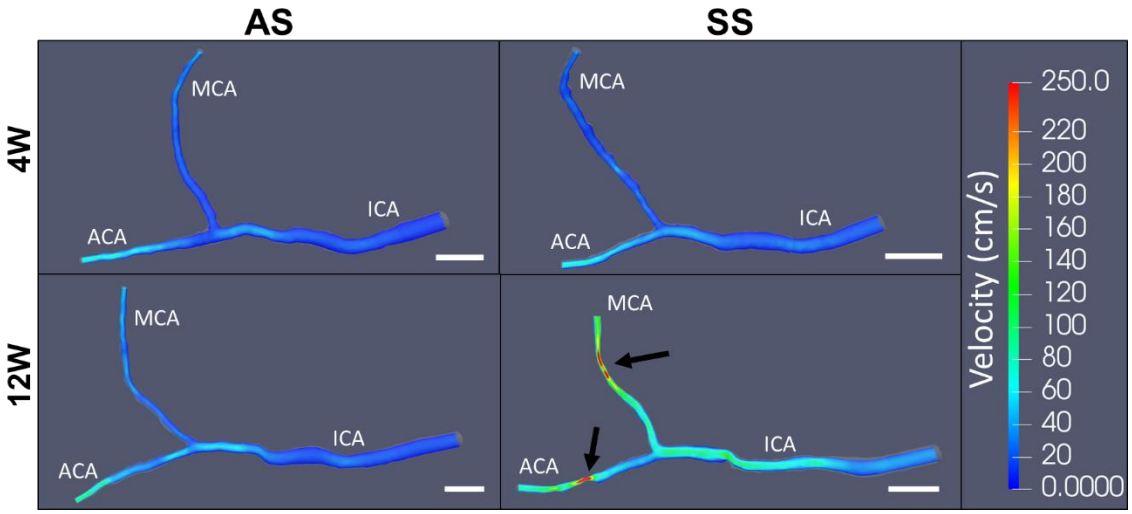

Figure 5.7: Velocities in the cerebral arteries are elevated in 12 SS mice.
Representative images of the velocity streamlines in the right ICA are shown for SS and AS mice at 4, and 12 of age. Regions of high velocity (arrows) were found to occur in 12 and 24-week mice.

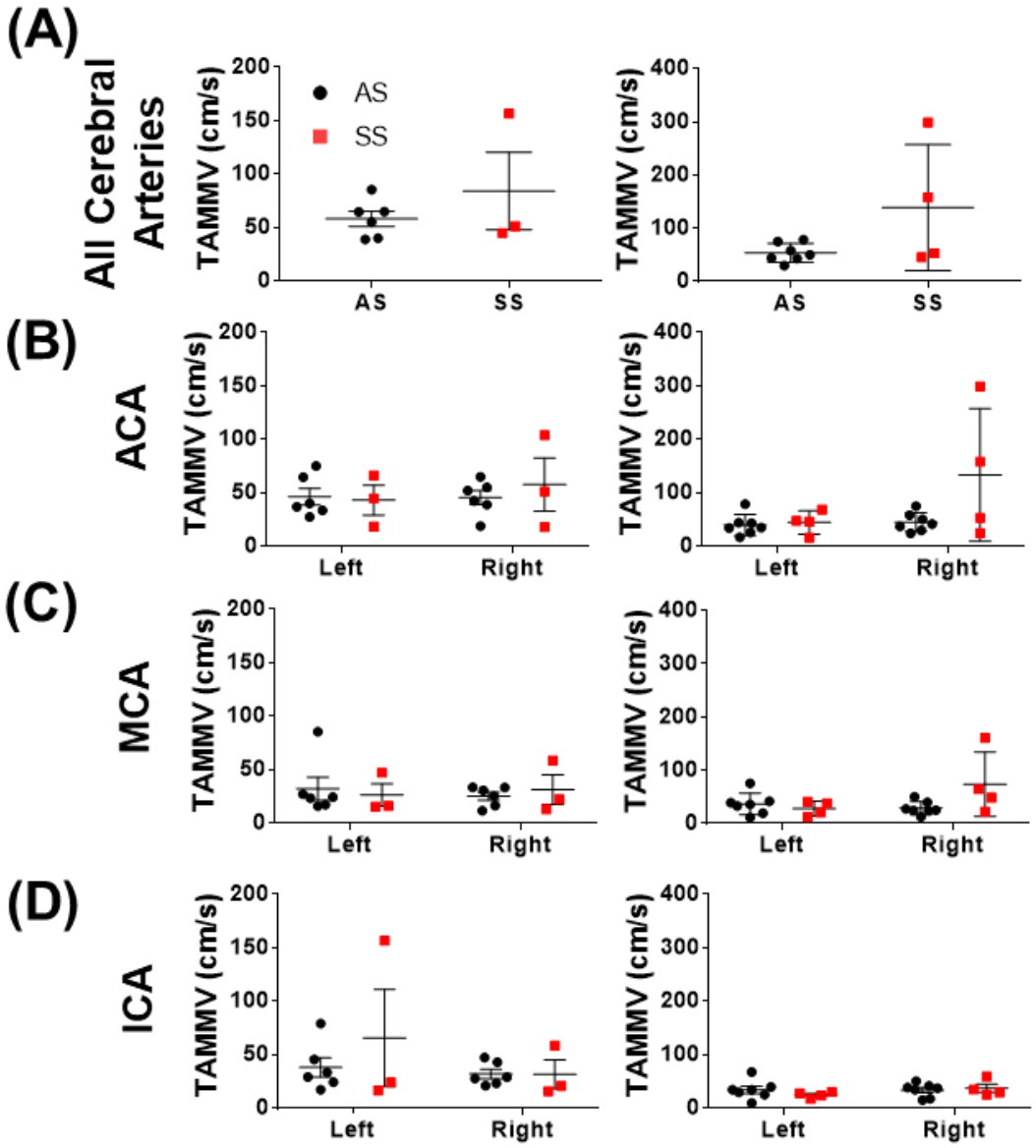

Figure 5.8: Time-averaged maximum-mean velocities from subject-specific simulations are slightly elevated in the right ACA of SS mice.
The highest TAMMV was calculated amongst all cerebral arteries **(A)** as well in each arterial segment: ACA **(B)**, MCA **(C)**, and ICA **(D)**. A trend towards elevated TAMMV is observed in SS mice, specifically due to high velocities measured in the right anterior cerebral artery. *$p < 0.05$ SS compared with AS by T-test. Error bars are SEM.

5.3.4 Geometries from 12-week sickle cell mice generate significantly elevated cerebral velocities with a fixed velocity waveform.

Simulations were repeated for the 12-week age group to determine if the elevated velocities observed in some of the SS mice were due to morphological differences created by SCA. The same inlet velocity profile was used for all subjects to remove variability produced from using subject-specific velocities. Using these new boundary conditions, SS mice were found to have a significantly higher TAMMV ($p < 0.05$), when examined across all cerebral arteries, and equated to a 143.9% increase from AS controls (Fig 5.9). Differences were again mostly found in the right ACA ($p < 0.1$), indicating that the geometry may be a probable cause for the elevated velocities. When the normalized cross-sectional area in the right ACA was examined, SS mice were found to have significant narrowing, up to 60% in some segments.

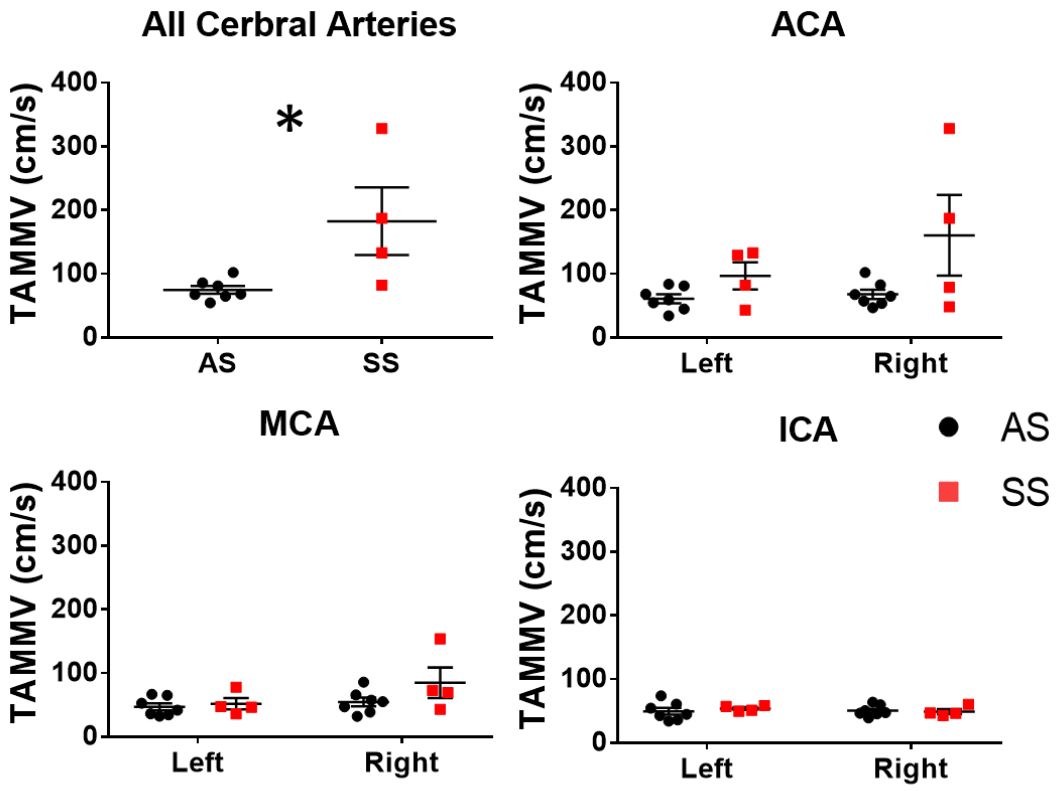

Figure 5.9: Geometries from 12-week sickle cell mice produce significantly elevated cerebral velocities when using the same inlet velocity.
Simulations were repeated in the 12-week age group utilizing the same inlet velocity boundary condition for all animals. Across the all cerebral arteries TAMMV was significantly in SS mice, and with differences due to elevated velocities in ACA. *$p < 0.05$ SS compared with AS by T-test. Error bars are SEM.

5.4 Discussion

Here we have developed a subject specific computational model for approximating the velocities in the cerebral arteries of a mouse with sickle cell disease. Using a combination of ultrasonography and plastination techniques we were able to quantify and characterize the hemodynamics in the cerebral arteries of sickle transgenic mice. This was validated by performing simulations in the carotid arteries. Simulated velocities in the extracranial carotid arteries matched well to *in vivo* ultrasound measurements.

Blood flow in the carotid arteries are can be higher in individuals with SCD regardless of stroke risk [169-171], and has been associated with increased cardiac output and/or decreased cerebrovascular reserve [172]. Sun et. al confirmed the CCA velocity in six-month (24 week) SS mice was elevated but only in comparison to AA counterparts [142]. Between AS and SS mice no differences were found in the peak systolic velocities or mean velocities for either 4 or 24-week mice, matching results from our study. This work demonstrated that in the cerebral arteries, velocities were elevated in mice with SCA. Though no significant differences were found in the subject-specific simulations a strong trend of elevated TAMMV was observed in 12-week SS mice. It is important to note that only ~10% of individuals with SCA suffer from ischemic strokes, and while this number is high compared to age-matched controls, it does represent a certain sub-population. TAMMV had a larger variance in the SS group, and these differences may be attributed to different sub-populations in sickle cell anemia. Performing additional studies on a larger sample size, may assist in identifying this population with high TAMMV in SCA.

Perturbation of the simulations by applying equivalent inlet velocity conditions has shown that geometries of mice with SCA produce significantly elevated TAMMV. Our

results suggest luminal narrowing in the intracranial ICA of SS mice is generating these higher velocities. Formation of stenosis are known to occur in sickle cell disease, and often associated with high velocities associated with stroke risk [4, 28, 50]. However abnormally high velocities can exist in the absence of large stenotic lesions [6]. Gradual narrowing of the cerebral arteries rather than a single large stenosis may explain this phenomenon.

Interestingly, in the Townes model elevated velocities and luminal narrowing was more prominent in the ACA rather in the MCA. This may be the results of evolutionary differences in the cerebrovascular network between the two species. In mice a majority of blood flowing from the ICA diverges into the ACA, providing nutrient to regions in the brain near the olfactory bulb. This is important as rodents rely heavily on their olfactory senses [134]. In humans, more blood is diverted to the MCA, supplying blood to cognitive regions in the brain.

Calculated velocities were mostly elevated on the right side of the brain. Side to side differences in hemodynamic parameters are usually negligible [95, 173, 174], therefore, the cause for these differences are not fully known. It has been previously reported that the hippocampus, thalamus, and visual cortex on the left side of the brain in C57BL/6J mice, one of the background strains for the Townes mice, are enlarged [163]. These regions are supplied by several arteries that branch from the ICA and may have higher oxygen demands than their counterparts on the right side. Maintaining cerebral blood flow to this region could potentially be magnified in the sickle mouse model leading side-to-side differences.

There are several limitations to this study. First, several tributaries along the ICA were removed to reduce computational cost. Addition of these arteries would create

additionally flow splits, which ultimately lowers the estimated velocities in the ACA and MCA. Future work will focus on using a more complete system which encompasses a more accurate representation of the cerebral arterial network. This, however, does not change the result that hemodynamic differences between the two genotypes were a result of SCA effecting the vascular morphology. Additionally, blood was modeled as a Newtonian substance, although this seems appropriate as shear rates in the cerebral arteries remained high, this does not consider the Fåhræus-Lindqvist effect. Apparent blood viscosity is a function of vessel size and decreases at when diameter is between 10 – 300 microns [175]. The cerebral arteries used in this system fall within this range; therefore, the viscosity used maybe lower than in the physiological system.

In conclusion, this study characterizes the velocity in the cerebral arteries of SS and AS mice at different ages. While velocities in the CCA and extracranial ICA do not significantly differ between AS and SS mice. Narrowing in the cerebral arteries of mice afflicted by SCA can significantly increase the blood velocity, one of the primary indicators of stroke risk in humans with SCA. Determining the pathological mechanisms for this luminal narrowing may help in developing therapeutics for preventing strokes. Additionally, such mechanistic studies and treatments can be evaluated using the framework of the computational model used in this study.

CHAPTER 6 FUTURE CONSIDERATIONS

6.1 Major Findings

The work presented in this thesis focused on developing a more complete understanding of the hemodynamic abnormalities associated with stroke risk in children with sickle cell anemia. Several paradoxes exist which complicate the overall understanding of fluid flow in SCA. To begin, knowledge of flow in tubes suggest that if flow rate is kept constant a localized increase in velocity is associated with a decrease in cross-sectional area. This principle is somewhat observed in SCA, as histological and radiological findings have shown the occurrence of stenotic lesions in individuals with a previous history of stroke. However, hemodynamic abnormalities indicative of stroke risk can occur before lesions become evident with magnetic resonance angiogram [6]. In addition, sickle red blood cells have increased rigidity, density, and viscosity which can ultimately impact the rheological properties of whole blood and in theory should slow rather increase the blood velocity. Through the utilization of computational fluid dynamics this work has elucidated the impact of sickle cell on the cerebrovascular anatomy and its effect on hemodynamics. This provides clues for determining the mechanisms associated with stroke in SCA. In addition, the framework of the computational models developed in this thesis can be used to investigate mechanisms and treatments related to stroke in SCA.

The work from the 2D computational model suggests that non-sickle blood has similar rheological properties to those so sickle blood in the large arteries. This is primarily due to a decrease in the overall hematocrit of whole blood in SCA (~25%), as red blood cells have a reduced life expectancy from premature lysing. In fact, extremely low hematocrits <20% can cause whole blood viscosity in patients with SCA to drop

significantly lower than non-sickle blood, and lead to extremely high velocities [107]. In addition, since shear rates in the large arteries exceeded 10 Hz, the computational model demonstrated that the sickle blood functions similarly to a non-Newtonian substance. Using this assumption can therefore significantly reduce the overall computation cost, when performing simulations in the large arteries of people with SCA.

Elucidating the influence of stenoses is important to determining the relationship between geometry and the hemodynamics. This work showed that even the addition of a large stenosis encompassing 75% of the luminal diameter was not enough to produce velocities indicative of stroke risk in a 2D model. This indicates that though large stenotic lesions are observed through radiological investigations, they are not the root cause for elevated velocities in people with SCA. This was confirmed in the 3D computational model where simulations were performed from geometries reconstructed from patients with and without SCA. This study demonstrated that even when the system was perturbed such that the inlet velocity was the same for all subjects, velocities remained elevated in the geometries of those with sickle cell. This suggest that SCA is altering the cerebrovascular geometry and generating abnormal hemodynamic profiles. Though the number of samples for this study was small, two characteristics were observed from the geometries with SCA. First though the MCA and ACA lacked any significant stenoses, small bumps were observed along the surface of the vascular, and these features appeared correlated to a narrowing in the cerebral arteries. The mechanism for these features is not fully understood; however, analysis of WSS revealed that the geometries from individuals with SCA, had larges areas affected by low and oscillatory shear stress that fell within ±5 dynes/cm^2. This work was published in Experimental Biology and Medicine [176].

The identification of large areas affected by low WSS in the cerebrovascular of patients with SCA, supports the hypothesis that SCA is altering the cerebrovascular anatomy. Low and oscillatory wall shear stress can cause endothelial cell dysfunction and initiate the beginning stages of vascular remodeling. The gradual narrowing observed in the human subjects could explain how velocities can be elevated in individuals with SCA, despite the lack of large morphological abnormalities.

In an effort to expand our findings from the 3D human simulations, a computational model was developed for investigating hemodynamics in the murine cerebrovascular system. Mouse models are extremely powerful tools, that can be used for studying pathophysiological mechanisms and testing potential therapeutic treatments. Unfortunately, few medical devices can measure cerebral artery velocities in a mouse with high accuracy. This creates a need for new methodologies, and CFD can be used to solve this problem. This study is among the first to perform 3D CFD simulations in the murine cerebrovascular with previous models using 1D approaches [168]. Though found to be highly accurate those models assume an average across an entire arterial segment and lack the ability to investigate specific geometric features. This model was validated through high frequency ultrasound. Diameters calculated in the ICA and eICA of reconstructed arteries did not significantly differ from *in vivo* diameters measured in ultrasound. Additionally, simulated velocity waveforms in the eICA was able to recapitulate measured ultrasound velocities.

Characterization of the vasculature in SS mice revealed that at 12 and 24-weeks the left proximal ICA was significantly enlarge in comparison to AS littermate controls. However, this morphological difference was lost at distal end, such that no differences

were observed in the MCA and ACA. To better characterize this trend luminal area was normalized to the proximal end of the artery for each animal. When analyzed in this manner the percent change in area was significantly lower in SS at certain sections of the artery. These morphological differences suggest two pathologies. First, the larger luminal areas measured in SS mice may be an indication of vasodilation in order to generate higher cerebral blood flows. Reduced oxygen availability in SCA is compensated by elevated cerebral blood flow (CBF) to increase the rate of oxygen delivery [156, 157]. This is supported by a reduced cerebral vasculature reserve in humans and mice with sickle cell disease [37, 138, 158]. When subjected to hypoxic conditions the blood vessels in SS subjects are unable to further dilate leading to a reduced increase in CBF, as compared to non-sickle controls. The enlarged lumens measured in the CCA and ICA of our SS mice could be attributed to this mechanism. Direct measurements of the luminal area in the cerebral arteries have also shown the ICA to be enlarged in humans with sickle cell disease [154].

Reduction in normalized area in the ICA and ACA of SS mice can be associated with luminal narrowing as was observed in human subjects. Subject-specific simulations of SS mouse geometries showed that narrowing in the ACA of 12-week SS mice equated to an increase in the TAMMV. Though no significant differences were found in the subject-specific simulations a strong trend of elevated TAMMV was observed. TAMMV had a larger variance in the SS group, and these differences may be attributed to different sub-populations in sickle cell anemia. Applying equivalent inlet velocity conditions; however, did significantly elevate the TAMMV in SS, showing that morphological changes in SCA can produce elevated velocities.

6.2 Examination of biochemical expression from patient specific cerebral blood flow

An aspect not covered by this thesis is the biomechanical influence of SCA. Current shear bioreactors allow for millisecond temporal accuracy, which enables analysis of unique patient specific hemodynamics on endothelial cells [177]. Individuals without SCA can be compared to those with SCA in order to demine if differences in in hemodynamic profiles from different set of patients effects biochemical response. Additionally, different stages of stroke risk can be examined by dividing individuals into categories: no history of stroke, risk for stroke, and those with a previous history of stroke. Using the computational model, magnetic resonance angiograms can be taken from these various subpopulations and used to derive wall shear stress profiles at specific locations in the artery. Sites near stenoses or vaso-occlusions would be of interest as these are known to stimulate endothelial cell dysfunction. Once shear profiles are actuated on to endothelial cells, biomarkers can be assayed to determine the impact of various hemodynamic profiles. Correlation of certain proteins or kinases to different levels of stroke risk could assist in developing predictive model. Currently, TCD is the only widely accepted method of determining stroke risk. Identification of certain biomarkers could help clinicians more accurately assess risk and provide an avenue for newer treatment options.

6.3 *in vivo* investigations of cerebrovascular diseases

The findings in this thesis suggests vascular remodeling may be involved in producing elevated velocities in SCA. Using the techniques utilized in the computational mouse model it is possible to investigate biochemical mechanisms that effect vascular remodeling in SCA. Several pathways have been implicated in vascular remodeling and

intimal hyperplasia. For example, upregulation of cathepsin K can initiate early stages of atherosclerosis [85]. Cathepsin K expression is tightly regulated through both biochemical and biomechanical interactions. Increased TNF-α in SCA has been shown to stimulate the cathepsin K expression in endothelial cells through JNK and c-Jun kinase pathways [178]. Additionally, through NF-κB, shear stress can either suppress or elevate cathepsin K expression [179]. Therefore, biomechanical pathway plays an important role in the matrix remodeling process.

Inhibitors can be used to evaluate the role of cathepsin K on both the vascular anatomy and hemodynamics in SCA. SP6000125 is a JNK inhibitor that has been shown to block upregulation of cathepsin K through the TNF-α pathway [178], and prevent elastin degradation in the carotid arteries of mice. Using the same procedures described in thesis, mice given a JNK inhibitor can be evaluated and compared to non-treated counterparts to demonstrate efficacy in preventing vascular remodeling. Analysis of morphometric values from treated mice can be used to determine if drug treatment prevents the luminal narrowing which was observed in this thesis. Simulations on reconstructed mouse models will also determine changes in the hemodynamic profiles. Additionally, future improvements with imaging modalities such as magnetic resonance angiogram [180] could also allow for longitudinal studies. Removing current limitation of endpoint analysis used in this system.

The computational models developed in this thesis can also be applied to other biological systems. Besides the cerebrovascular, sickle cell anemia also impacts various other organs. Among these co-morbidities there is an increase likelihood of avascular necrosis in the femoral head [181, 182]. This results in bone death leads and loss of

mechanical properties, requiring some individuals to have hip replacements during early adulthood. Studies have suggested intravascular sickling and the increased viscosity in the capillaries are related to avascular necrosis [183]; however, few studies have examined the large arteries in the femur [184]. Additionally, the mouse model developed in this study can adopted to investigate other cerebrovascular diseases outside SCA. This is beneficial in mice with hundreds pre-existing genetically modified. Some pathologies which can benefit from investigating cerebrovascular hemodynamics include Alzheimer's [185, 186], cancer [187], and atherosclerosis [188].

APPENDIX

A.1. Script for preforming computational fluid dynamic simulations in LifeV

```
#-----------------------------------------------
#    Data file for the MCA in Navier-Stokes
#-----------------------------------------------

[fluid]

    [fluid/problem]
        preloadT         = 0.0250 #Period of perload waveform
        startT           = 0. # Time when actual simulations
starts
        period           = 0.1445 #Cardiac period for velocity
waveform used in simulation

      interpolateBoundaryData = true
       cosinePreload    = true
        # Boundary Labels
        inflowList          = '1'
        wallList            = '10'
        RCRList             = '2,3'


#Input Boundary Condition
        [./inflow0]
            rescale      = 1.0
            correction   = 1.0
            smoothRatio  = 0.8
            profileShape = parabolic
             dataKind     = velocity
            input_file   = ../AS/Velocity/12W/050_LICA_M.dat
        [../]

#Outlet Boundary Conidtions
        [./outflow0]
            R1              = 2.8202e6
            R2              = 8.7776e6
            C               = 2.3894e-9
            RT              = 1.1598e7
        [../]

         [./outflow1]
           R1             = 2.4575e6
         R2          = 4.9904e6
         C                = 2.0128e-9
         RT          = 7.4479e6
        [../]
```

```
#Fluid Properties
    [fluid/physics]
        density          = 1.057        # density    g/cm^3
        viscosity        = 0.04879      # viscosity g/(cm*s)
(poise)

    [fluid/space_discretization]
        mesh_dir         = ../SS/Mesh/12W/
        mesh_type        = .vol
        mesh_file        = 095_LICA_NoPoCA.vol
        mesh_faces       = all                       # update all
faces elements
        mesh_edges       = all                       # update all
edges elements
        velocity_fespace = P1Bubble
        pressure_fespace = P1
        mass_lumping     = true           # mass lumping
accelerate convergence, reduce accuracy
        stiff_strain     = true                 # if true we
discretize \int (grad(u) + grad(u)^T)*(grad(v) + grad(v)^T)
        matrix_pattern   = true             #add \int div(w)u*v
stabilization
        offlinePartitioning = false

        [./stabilization]
            betaSD       = 0.5 #0     # scalar parameter of SD
stabilization
            divBetaUV    = false    # add \int div(w)u*v
stabilization
            stabilizeBackflows = 0.
        [../]

    [fluid/time_discretization]
        initialtime      = -0.125
        endtime          = 0.4350
        timestep         = 0.0005
        verbose          = 0
        BDF_order        = 1
        order_yosida     = 1
        nonlinearity_treatment = 0

[miscellaneous]
    verbose        = 1
    showdata       = false

[exporter]
    type           = Ensight
    post_dir       = ../SS/Results/12W/095_LICA_MS/
    multimesh      = false
    save           = 5
    exportMode     = 2        # only for VTK export
    floatPrecision = 1    # only for VTK export
```

```
time_id_width  = 6
```

A.2. Matlab code for calculating mean velocity across a cross-section of an artery

```
close all;
clear all;
clc;
tic;
%% Section 1: Extracting Key Variables from Excel Files
%-------------------------------------------------------
-------
%Creates a list and counts the number of CSV files in
folder
%-------------------------------------------------------
-------
timestep = 0.0025;
listOfCSVs = dir('*.csv');
NumberOfFiles = numel(listOfCSVs); %Total Number of CSV
Files i.e. number of timesteps
Nameholder = {listOfCSVs(:).name};
Nameholder2 = Nameholder{1,1};
token = strtok(Nameholder2,'.');

%Name of all the filenames organized in time
ListOfTimes = strings(1,NumberOfFiles);
for count0 = 0:NumberOfFiles
%     ListOfTimes(1,count0+1) =
strcat(token,'.',num2str(count0+1),'.csv');
    ListOfTimes(1,count0+1) =
strcat(token,'.',num2str(count0),'.csv');
end

%fnm = rot90(struct2cell(listOfCSVs)); %This needs to
be sorted by name
%fnm =sortrows(fnm,1);

%-------------------------------------------------------
-------
%Extracts Data from Directory and places it into a cell
%-------------------------------------------------------
-------

RAW_slice = cell(1,NumberOfFiles); %Empty Cell to Hold
all Data from Slice
for count0 = 1:NumberOfFiles
```

```
    RAW_slice{1,count0} =
csvread(ListOfTimes(1,count0),1,0);
end

NumberOfPoints = length(RAW_slice{1,1});

%-------------------------------------------------------
-------
%Extracts x, y, and z corrdinates of points
%-------------------------------------------------------
-------
Coord3 = zeros(3,NumberOfPoints);%Empty matrix to Hold
coordinates of all points in the Slice
for count0 = 1:NumberOfPoints
    for count1 = 1:3
        Coord3(count1,count0) =
RAW_slice{1,1}(count0,4+count1);
    end
end

x1 = Coord3(1,:);
y1 = Coord3(2,:);
z1 = Coord3(3,:);

%-------------------------------------------------------
-------
%Creates sub-Cell of only Velocity and Calculates its
Magnitude
%-------------------------------------------------------
-------
%[Long,Wide] = size(RAW_slice{1,1});
Vel = cell(1,NumberOfPoints);

for count1 = 1:NumberOfPoints
    for count2 = 1:NumberOfFiles
        for count3 = 1:3
            Vel{1,count1}(count2,count3) =
RAW_slice{1,count2}(count1,count3); %Extracting x, y,
and z values for Velocity
        end
        Vel{1,count1}(count2,4) =
sqrt(Vel{1,count1}(count2,1)^2 +
Vel{1,count1}(count2,2)^2 + Vel{1,count1}(count2,3)^2);
%Calculates Magnitude of Velocity
```

```
    end
end

%Creates Matrix for both Velocity Magnitude and Time
Time = zeros(NumberOfFiles,1);
Mag_Vel = zeros(NumberOfFiles,NumberOfPoints);

for count1 = 1:NumberOfFiles-1
   Time(count1+1,1) = Time(count1,1)+timestep;%Extracts
Time
end

for count1 = 1:NumberOfFiles
    for count2 = 1:NumberOfPoints
        Mag_Vel(count1,count2) =
Vel{1,count2}(count1,4); %Calculates Maximum Velocity
    end
end

%Calculate Time of Systole
collect_mag_vel1 = 0;
for count1 = 1:NumberOfPoints
    for count2 = 1:NumberOfFiles
        collect_mag_vel2 =  Mag_Vel(count2,count1);
        if collect_mag_vel2 > collect_mag_vel1
            collect_mag_vel1 = collect_mag_vel2;
            Time_Max_Vel = count2;
        else
            %collect_mag_vel1 = collect_mag_vel1;
        end
    end
end

%-----------------------------------------------------
-------
%Creates cell for Pressure
%-----------------------------------------------------
-------
Press = cell(1,NumberOfFiles);

for count1 = 1:NumberOfPoints
    for count2 = 1:NumberOfFiles
```

```
        Press{1,count2}(count1,1) =
RAW_slice{1,count2}(count1,4); %Extracting x, y, and z
values for Velocity
    end
end


%% Section 2: Rotates Slice from 3D to 2D Coordiante
System and Calulates the Perimeter
%-----------------------------------------------------
-------
%Convert 3D plane to 2D
%-----------------------------------------------------
-------
Coord3_O =
bsxfun(@minus,rot90(Coord3),mean(rot90(Coord3))); % Set
Mean of scatter points to Origin
[c,xyz] = pca(Coord3_O); % xyz2 will be what you want.
Coord2 = rot90(xyz,-1);

x2 = Coord2(1,:);
y2 = Coord2(2,:);
x2rot = rot90(Coord2(1,:));
y2rot = rot90(Coord2(2,:));

%Check
xyz_hat = xyz*c'; % xyz_hat = Coord3_O

% Round_xyz_hat = round(xyz_hat, 5);
% Round_Coord3_O = round(Coord3_O,5);
%
% if Round_xyz_hat == Round_Coord3_O
%     fprintf('Rotation is Good!\n\n');
% else
%     fprintf('Rotation is Bad\n\n');
% end

%% Section 3: Triangulation
%-----------------------------------------------------
-------
%Traditional Triangulation
%-----------------------------------------------------
-------
DT = delaunayTriangulation(x2rot,y2rot);
```

```
k = convexHull(DT);
Area = polyarea(DT.Points(k,1),DT.Points(k,2));

%-------------------------------------------------------
-------
%Alpha Triangulation
%-------------------------------------------------------
-------
Coord2_2 = zeros(NumberOfPoints,2);
Coord2_2(:,1) = x2rot;
Coord2_2(:,2) = y2rot;

center_2D = [mean(x2rot); mean(y2rot)]; %Calculates
Center Using All points

Mag_Coord_2D = zeros(NumberOfPoints,1); %Emty holding
variable to hold distance of each point from center 1

for count1 = 1:NumberOfPoints
    Mag_Coord_2D(count1,1) = sqrt( ((center_2D(1,1)) -
(Coord2_2(count1,1)))^2 +  ((center_2D(2,1)) -
(Coord2_2(count1,2)) )^2);
end

mean1 = mean(Mag_Coord_2D);

[Area_2,Alpha] = alphavol(Coord2_2,mean1/2,1);

Alpha_Cell = struct2cell(Alpha);
Alpha_Tri = Alpha_Cell{1,1};
Alpha_Area = Alpha_Cell{2,1};
Alpha_RCC = Alpha_Cell{3,1};
Alpha_BD = Alpha_Cell{4,1};

DT_BD = delaunayTriangulation(x2rot,y2rot,Alpha_BD);
IO = isInterior(DT_BD);
IO2 = double(IO);

Connect = DT_BD.ConnectivityList(IO,:);
Points = DT_BD.Points;
%
% %k3 = k(IO, :);
% %DT3_bd = DT3(IO, :);
%Area3 = polyarea(DT.Points(k3,1),DT.Points(k3,2));
```

```
Time_Setup = toc;

%% Section 4: Interpolating Values
tic;
%-------------------------------------------------------
-------
%Interpolated Points in a Grid
%-------------------------------------------------------
-------
mesh_size = 100;
x_grid = min(x2rot):(max(x2rot)-
min(x2rot))/mesh_size:max(x2rot); %Proxy points in x
y_grid = min(y2rot):(max(y2rot)-
min(y2rot))/mesh_size:max(y2rot); %Proxy points in y
[xq,yq] = meshgrid(x_grid,y_grid); % Grid of proxy
points
IN = inpolygon(xq, yq,
DT_BD.Points(k,1),DT_BD.Points(k,2));
IN2 = double(IN);

%Interpolation of Velocity Profile during Systole
F = scatteredInterpolant(x2rot, y2rot,
rot90(Mag_Vel(Time_Max_Vel,:)),'linear'); %Creates
function relating x and y to velocity at arbitary Time
point
vq = F(xq,yq); %Calculates Velocity Values for proxy
points at arbitary Time point

%Interpolation across all time points
Mag_Vel_interp = cell(1,NumberOfFiles);

for count1 = 1:NumberOfFiles
f = scatteredInterpolant(x2rot, y2rot,
rot90(Mag_Vel(count1,:)), 'linear');
Mag_Vel_interp{1,count1} = (f(xq,yq));
%Mag_Vel_interp{1,count1} = rot90(f(xq,yq));
end

%-------------------------------------------------------
-------
% Create Single Matrix to holding variables for only
coordinates values within the slice area
```

```
%-------------------------------------------------
-------
Long2 = length(x_grid);
Long3 = sum(sum(IN2));
interp_coord = zeros(Long3,2);
interp_v = zeros(Long3,NumberOfFiles);

One_count = 1;

for count1 = 1:Long2
    for count2 = 1:Long2
        if IN2(count1, count2) == 1
            interp_coord(One_count,1) = xq(count1,
count2);
            interp_coord(One_count,2) = yq(count1,
count2);
            One_count = One_count + 1;
        else One_count = One_count;
        end
    end
end

DT2 =
delaunayTriangulation(interp_coord(:,1),interp_coord(:,
2));
k2 = convexHull(DT2);

for count1 = 1:NumberOfFiles
    One_count = 1;
    for count2 = 1:Long2
        for count3 = 1:Long2
            if IN2(count2, count3) == 1
                interp_v(One_count,count1) =
Mag_Vel_interp{1,count1}(count2, count3);
                One_count = One_count + 1;
            else One_count = One_count;
            end
        end
    end
end

Time_Interp = toc;
```

```
%% Section 5: Calculating the Velcoity by Integrating
over Surface
tic;
%-------------------------------------------------------
-------
%Integrating Velocity Over Surface
%-------------------------------------------------------
-------
int1 = zeros(NumberOfFiles,1);
int2 = zeros(NumberOfFiles,1);
int3 = zeros(NumberOfFiles,1);

for count1 = 1:NumberOfFiles
int1(count1,1) =
integrate(DT,rot90(Mag_Vel(count1,:)))/sum(getElementAr
eas(DT));
end

for count1 = 1:NumberOfFiles
int2(count1,1) =
integrate(DT2,interp_v(:,count1))/sum(getElementAreas(D
T2));
end

for count1 = 1:NumberOfFiles
int3(count1,1) =
integrate2(Points,rot90(Mag_Vel(count1,:)),Connect)/sum
(getElementAreas2(Points,Connect));
end


Velocity(:,1) = Time;
Velocity(:,2) = int3;

Time_integrating = toc;
%% Mean Press
%-------------------------------------------------------
-------
%Calculating Mean Pressure in Slice
%-------------------------------------------------------
-------
Avg_Press = zeros(1,NumberOfFiles);

for count0 = 1:NumberOfFiles
```

```
    Avg_Press(1,count0) = mean(Press{1,count0});
end
Press_at_Sys = Avg_Press(1,Time_Max_Vel);

%% Section 6: Graphs
% tic
% %-------------------------------------------------------
---------
% %Plots Scatter Plot of Slice Points in 3D
% %-------------------------------------------------------
---------
% figure(2)
% subplot(1,3,1);
% scatter3(x1,y1,z1,'filled'); %Scatter Plot of Points
in Slice
% title('Scatter Plot of Points in 3D');
% xlabel('X Coordinates (cm)');
% ylabel('Y Coordinates (cm)');
% zlabel('z Coordinates (cm)');
% legend('Points','Location','Best');
% rotate3d on;
%
% %-------------------------------------------------------
---------
% %Plots Scatter Plot of Slice Points Rotated
Coordinate System (2D)
% %-------------------------------------------------------
---------
% subplot(1,3,2);
% triplot(DT,'g');
% hold on
% triplot(DT_BD(IO, :),DT_BD.Points(:,1),
DT_BD.Points(:,2),'k');
% hold on
% scatter(Coord2(1,:),Coord2(2,:),'filled');hold on
%
plot(DT_BD.Points(k,1),DT_BD.Points(k,2),'r','LineWidth
', 2);
% title('Scatter Plot of Points Rotated to a 2D
Coordinate System');
% xlabel('X Coordinates (cm)');
% ylabel('Y Coordinates (cm)');
% legend('Normal Triangulation','Alpha Triangulation
','Points','Perimeter','Location','Best');
```

```
%
% %-------------------------------------------------
---------
% %Plots Interpolation Coordinates Rotated Coordinate
System
% %-------------------------------------------------
---------
% subplot(1,3,3);
% scatter(interp_coord(:,1),interp_coord(:,2),'+');
% hold on
% plot(DT2.Points(k2,1),DT2.Points(k2,2),'r-');
% title('Scatter Plot of Interpolated Points in 2D
System');
% xlabel('X Coordinates (cm)');
% ylabel('Y Coordinates (cm)');
% legend('Interpolated
Points','Perimeter','Location','Best');
%
% %-------------------------------------------------
---------
% %Plotting The Averages of Velocity
% %-------------------------------------------------
---------
% figure(3)
% plot(Time,int1,Time,int2,Time,int3);
% title('Average Velocity of Slice');
% xlabel('Time (s)');
% ylabel('Average Velocity (cm/s)');
% legend('Integration Using Given Points','Integration
Using Interpolated Points','Integration Using Given
Points (Alpha Triangulation)','Location','Best')
%
% %-------------------------------------------------
---------
% %Plots Surface of Velocity During Systole
% %-------------------------------------------------
---------
% figure(4)
% scatter3(x2rot, y2rot,
rot90(Mag_Vel(floor(Time_Max_Vel),:)),'r','filled');
%Plots known points at arbirary time
% hold on;
% mesh(xq,yq,vq); %Plots interpolated Grid
% hold on
```

```
% plot(xq(IN),yq(IN),'k+')
% hold on;
% plot(xq(~IN),yq(~IN),'m+')
% hold on;
% plot(DT.Points(k,1),DT.Points(k,2),'r-
','LineWidth',4); %Plots Perimeter of slice
% title('3D Representation of Velocity');
% xlabel('X Coordinates (cm)');
% ylabel('Y Coordinates (cm)');
% zlabel('Velocity (cm/s)');
% legend('Given Points','Interpolated Values','Area of
Integration','Area Outside of
Integration','Perimeter','Location','Best')
%
% hcb = colorbar;
% colorTitleHandle = get(hcb,'Title');
% titleString = 'Velocity (cm/s)';
% set(colorTitleHandle ,'String',titleString);
% rotate3d on;
%
% Time_Plots = toc;

%% Section 7: Results
%-----------------------------------------------------
-------
%Printing Results
%-----------------------------------------------------
-------
close all;
fprintf('\nResults:\n')
%fprintf('Total Time %4.3f s\n', Time_Setup +
Time_Interp + Time_integrating + Time_Plots);
Round_xyz_hat = round(xyz_hat, 5);
Round_Coord3_O = round(Coord3_O,5);

if Round_xyz_hat == Round_Coord3_O
    fprintf('Rotation is Good!\n\n');
else
    fprintf('Rotation is Bad\n\n');
end

fprintf('Area of Slice (Normal Triangulation): %4.7f
cm^2\n', Area);
```

```
fprintf('Area of Slice (Alpha  Triangulation): %4.7f
cm^2\n', Area_2);
fprintf('Maximum Velocity: %4.2f cm/s\n',
max(max(Mag_Vel)));
fprintf('Maximum Flow Rate: %4.7f cm^3/s\n\n',
max(max(Mag_Vel))*Area_2);

fprintf('Velocity Measurments Using Integration
Method:\n');
fprintf('Maximum Value for Integration of Given Points:
%4.2f cm/s\n', max(int1));
fprintf('Maximum Value for Integration of Interpolated
Points: %4.2f cm/s \n', max(int2));
fprintf('Maximum Value for Integration of Given Points
with Alpha Triangulation: %4.2f cm/s \n', max(int3));
fprintf('Flow Rate: %4.7f cm^3/s\n',max(int3)*Area_2);
fprintf('Mean Pressure at Systole: %4.2f
dynes/cm^2/s\n\n',Press_at_Sys);

AAA = rot90([Area_2, max(int3), max(int3)*Area_2,
Press_at_Sys], 3);
```

A.3. Matlab code for calculating time-average mean waveforms

```
function [avg, x, peakSV, avgVel, endVel, T, aT, dT,
pI, rI] = processVelocity(matrix, lengths, name)
%processVelocity Processes velocity data to get the avg
waveform and its
%key characteristics
[diff, meanX, meanY] = checkXValues(matrix, lengths,
name); %Checks for and removes duplicate X values

% Separates the file name into its component parts
[~, rem] = strtok(name, '\');
for ndx = 1:7
    [~, rem] = strtok(rem, '\');
end
[typeWeek, rem] = strtok(rem, '\');
[type, week] = strtok(typeWeek, '_');
week(1) = [];
[num, rem] = strtok(rem, '\');
[art, ~] = strtok(rem, '\');
myTitle = sprintf('%s : %sW : %s : %s', type, week,
num, art); %Creates title for the graph
myTitle_Profile = sprintf('%s_%sW_%s_%s', type, week,
num, art); %Creates title for the graph
if (strcmp(myTitle, 'WT : 6W : 119 : LICA'))
    stopper = false;
end

p1 = meanX(1);
p2 = meanX(end);
%Removes NaN values from the end of the mean data
while (isnan(p2))
    meanX(end) = [];
    meanY(end) = [];
    p2 = meanX(end);
end
delta = 0.0005; %Sets the delta desired between x
values
%Adjusts delta if the actual difference between the x
values is smaller
%than the preset delta
while (diff < delta)
    delta = delta - 0.0001;
end
```

```
newX = p1:delta:p2; %Generates a new set of x values
% Interpolates using spline y values to correspond with
the new x values.
% This is done to have the x and y values be
consistently spaced
try
[meanY] = interp1(meanX, meanY, newX, 'spline');
catch
    stopper = false;
end
% Determines the thresholds for the wave data
maxY = max(meanY);
maxP = 0.20;
maxT = maxY - (maxP * maxY); %Max threshold
minT = median(meanY); %Min threshold
xVals = newX(meanY >= maxT); %Grabs xVals above the max
threshold
% Plots the wave form data with the thresholds

% figure
% hold on;
% xlabel('Time (s)', 'FontSize', 24);
% ylabel('Velocity (mm/s)', 'FontSize', 24);
% plot(newX, meanY);
% plot([newX(1),newX(end)], [maxT, maxT]);
% plot([newX(1),newX(end)], [minT, minT]);

% Uses Fourier Transform to filter data
fourier = fft(meanY);
fourierM = abs(fourier);
four_filter = zeros(1, length(fourierM));
[order,originalpos] = sort(fourierM, 'descend' );
thresh = order(1,15);
for r = 1:length(fourierM)
    if fourierM(1,r) < thresh
        four_filter(1,r) = 0;
    else
        four_filter(1,r) = fourier(1,r);
    end
end
four_filterMag = abs(four_filter);
inverse_fourier = ifft(four_filter);

% plot(newX, inverse_fourier)
```

```
maxY2 = max(inverse_fourier);
maxP2 = 0.25;
maxT2 = maxY2 - (maxP2 * maxY2); %Max threshold
minT2 = median(inverse_fourier); %Min threshold
xVals2 = newX(inverse_fourier >= maxT2);

if (any(strcmp(myTitle, {'WT : 4W : 120 : LICA', 'WT :
4W : 120 : RICA', 'WT : 4W : 122 : LICA', 'WT : 4W :
125 : LICA'})))
    maxT2 = maxT2 + 15;
end
if (any(strcmp(myTitle, {'WT : 6W : 116 : LICA', 'WT :
6W : 118 : LICA'})))
    maxT2 = maxT2 + 22;
end
if (any(strcmp(myTitle, {'WT : 4W : 123 : LICA', 'WT :
6W : 119 : LICA'})))
    maxT2 = maxT2 + 25;
end

% plot([newX(1),newX(end)], [maxT2, maxT2]);
% plot([newX(1),newX(end)], [minT2, minT2]);
% set(gca,'FontSize',18)

xVals3 = newX(meanY >= maxT2); %Catches more peaks

% [mat] = splitPeaks(xVals, (delta + .0001));
%Seperates the the x values into groups of peaks
% [mat3] = splitPeaks(xVals2, (delta + .0001));
[mat4] = splitPeaks(xVals3, (delta + .0001));
%Seperates the the x values into groups of peaks
[peaks] = getPeaks(mat4, meanY, newX, myTitle); %Gets
the highest peak and x value from each set of x values
in mat4
[mat2] = getWaves(peaks, minT, meanY, newX, myTitle);
%Gets the waveform associated with each peak and
removes bad waveforms
[r, ~] = size(mat2);
% Plots each wave form and a before shift avg and a
post shift avg

% figure
% subplot(1,1,1);
```

```
% hold on;

yVectors = [];
for ndx = 1:r
    xVec = mat2{ndx, 1}(2,:);
    yVec = mat2{ndx, 1}(1,:);
    colorVal = 0.8; %Causes line to be light gray
%     plot(xVec, yVec, 'color', [colorVal, colorVal,
colorVal]);
    [~, c] = size(yVectors);
    if (~isempty(yVectors))
        [~, c2] = size(yVec);
        if (c2 >= c)
            yVec = yVec(1:c);
        else
            yVectors = yVectors(:, 1:c2);
        end
    end
%     Stores the waveforms and conforms to shortest
wave form
    yVectors = [yVectors; yVec];
end
avg = mean(yVectors); %Gets the average wave form
[~, col] = size(avg);
x = 0:delta:(col - 1) * delta;
% Plots the avg wave form
% graph1 = plot(x, avg, '-k');
% set(graph1,'LineWidth',2);
% xlabel('Time (s)', 'FontSize', 24);
% ylabel('Velocity (mm/s)', 'FontSize', 24);
% Plots shifted data
% figure
% subplot(1,1,1);
% hold on;
% graph1 = plot(x, avg, '--b');
% xlabel('Time (s)', 'FontSize', 24);
% ylabel('Velocity (mm/s)', 'FontSize', 24);
% set(graph1,'LineWidth',2);

[mat2, yVecAVG, remIndex] = phaseShift(mat2, myTitle);
%Corrects out of phase waveforms
[r, ~] = size(mat2);
for ndx = 1:r
    xVec = mat2{ndx, 1}(2,:);
```

```
    yVec = mat2{ndx, 1}(1,:);
    colorVal = 0.8; %Causes line to be light gray
%     plot(xVec, yVec, 'color', [colorVal, colorVal,
colorVal]);
end
avg = nanmean(yVecAVG); %Gets the average wave form
discluding NaNs
avg(1:remIndex) = [];
avg = snipper(avg, myTitle);
avg = smoother(avg);
[~, col] = size(avg);
[~, Avg_PSV_Index] = max(avg);
[~, maxYVal_Index] = max(mat2{1, 1}(1,:));
maxXVal = mat2{1, 1}(2,maxYVal_Index);
x = 0:delta:(col - 1) * delta;
maxAvgX = x(Avg_PSV_Index);
diffX = maxXVal - maxAvgX;
x = x + diffX;
% Plots the avg wave form

% graph1 = plot(x, avg, '-k');
x = x - diffX;
% set(graph1,'LineWidth',2);
% set(gca,'FontSize',18)
% title(myTitle, 'FontSize', 32);
%
% title(myTitle, 'FontSize', 18);
fprintf([myTitle, '\n']) %Prints the title into command
window to show which file the function has processed
% Plots the avg and the max and min lines of the
waveform data
% box on;
% hold off;
% figure;
% maxAvg = max(yVectors);
% minAvg = min(yVectors);
% hold on;
% X=[x, fliplr(x)];                %create continuous x
value array for plotting
% Y=[maxAvg,fliplr(minAvg)];              %create y
values for out and then back
% fill(X,Y,[0.5, 0.8, 0.95]);
% graph2 = plot(x, avg, '-k');
% set(graph2,'LineWidth',2);
```

```
% xlabel('Time (s)', 'FontSize', 16);
% ylabel('Velocity (mm/s)', 'FontSize', 16);
% myTitle = sprintf('%s : %sW : %s : %s', type, week,
num, art);
% title(myTitle, 'FontSize', 18);
% box on;
% hold off;
%Extracts the key characteristics from the avg wave
form
[peakSV, x2] = max(avg);
avgVel = mean(avg);
endVel = avg(end);
T = x(end);
% x2 = x(avg == peakSV);
x1 = x(1);
y2 = peakSV;
y1 = avg(1);
aT = x2 - x1;
dT = (y2 - y1)/aT;
pI = (peakSV - endVel)/avgVel;
rI = (peakSV - endVel)/peakSV;

% Export the velocity profile of mouse to excel sheet
avg = avg./10;
profile = num2cell([x',avg']);
header = {'Time', 'Velocity'};
myLength = cell(1, 2);
myLength{1, 2} = length(avg) + 1;
header = [header; myLength];
profile = [header; profile];
[rNum, ~] = size(profile);
period = cell(rNum, 3);
period{1, 2} = 'Period';
period(3:7, 2) = {'delta t'; 'T'; '3T'; '4T'; '5T'};
period(3:7, 3) = {round((x(2) - x(1)), 4); T; 3*T; 4*T;
5*T};
profile = [profile, period];
xlswrite(myTitle_Profile, profile);
close all;
end

function [delta, x, y] = checkXValues(mat, lengths,
name)
```

```
% checkXValues Checks for duplicate x values and
removes them if possible
x = mat(:, 1);
y = mat(:, 2);
%Separates the file name into its component parts
[~, rem] = strtok(name, '\');
for ndx = 1:7
    [~, rem] = strtok(rem, '\');
end
[typeWeek, rem] = strtok(rem, '\');
[num, rem] = strtok(rem, '\');
[art, ~] = strtok(rem, '\');
name = sprintf('%s : %s : %s', typeWeek, num, art);
%Name of the data being processed

num1 = x(1);
num2 = x(2);
delta = num2 - num1; %Determines the delta between two
points in the x values
[r, ~] = size(x);
removeVector = [];
%Iterates through the x values looking for duplicates
for ndx = 1:r - 3
    x1 = x(ndx);
    x2 = x(ndx + 1);
    x3 = x(ndx + 2);
    x4 = x(ndx + 3);
    y1 = y(ndx);
    y2 = y(ndx + 1);
    y3 = y(ndx + 2);
    y4 = y(ndx + 3);
    %Throws exception if there are three duplicate x
values
    if (x1 == x2 == x3)
        ind = ndx;
        stopper = true;
        counter = 1;
        %Determines where the duplicates are to output
in the exception
        while stopper
            if ind < lengths(1)
                stopper = false;
            else
                ind = ind - lengths(1);
```

```
                lengths(1) = [];
                counter = counter + 1;
            end
        end
        msgID2 = 'Data:DuplicateXValue';
        msg2 = sprintf('There is at least one duplicate
X value in %s at index %d in file %d', name, ind,
counter);
        baseException = MException(msgID2,msg2);
        throw(baseException);
    end
%     Handles the case where two duplicate x values are
found
    if (x2 == x3)
        m = (y4 - y1)/(x4 - x1);
        newY = m*x2 + (y1-x1*m);
        diff2 = abs(newY - y2);
        diff3 = abs(newY - y3);
        if (diff2 >= diff3)
            removeVector = [removeVector, ndx + 1];
        else
            removeVector = [removeVector, ndx + 2];
        end
    end
%     Adjusts delta to be the small possible
    diff = num2 - num1;
    if (diff < delta)
        delta = diff;
    end
end
% Removes the duplicate x values and corresponding y
values
x(removeVector) = [];
y(removeVector) = [];
end

function [mat] = splitPeaks(xVals, delta)
% getWaves splits a vector of x values into the
individual waveforms and
% stored in the output matrix
xVals(end + 1) = 0;
[~, c] = size(xVals);
ind1 = 1;
mat = [];
```

```
for ndx = 1:c - 1
   num1 = xVals(ndx);
   num2 = xVals(ndx + 1);
   if ((num2 - num1) > delta || num2 == 0)
       ind2 = ndx;
       vec = xVals(ind1:ind2);
       ind1 = ndx + 1;
       vec = {vec};
       mat = [mat; vec];
   end
end
end

function [peaks] = getPeaks(mat, yVec, xVec, myTitle)
% getPeaks Takes in the matrices of the x values and
returns the peaks of
% the waveforms and their respective x values;
[r, ~] = size(mat);
peaks = zeros(2,r);
% Iterates through mat and picks the highest point in
each
for ndx = 1:r
    vec = mat{ndx, 1};
    [~, c] = size(vec);
    xMax = vec(1);
    yMax = yVec(xMax == xVec);
    for ind = 2:c
        x = vec(ind);
        y = yVec(x == xVec);
        if (y > yMax)
            yMax = y;
            xMax = x;
        end
    end
    %Stores the highest peak in terms of x and y in
peaks
    peaks(1, ndx) = yMax;
    peaks(2, ndx) = xMax;
end
    [~, c] = size(peaks);
    if (any(strcmp(myTitle, {'SS : 6W : 085 : LICA'})))
        remVec = 1:c;
        log = peaks(1, :) < 100;
        remInd = remVec(log);
```

```
        peaks(:, remInd) = []; %removes "peaks" that
are not actually peaks
    end
    [~, c] = size(peaks);
    counter = 1;
%     Removes peaks that are too close together to
indicate the peak of a
%     new wave form
    while counter < c
        x1 = peaks(2, counter);
        x2 = peaks(2, counter + 1);
        log1 = (x2 - x1) < 0.1;
        y1 = peaks(1, counter);
        y2 = peaks(1, counter + 1);
        log2 = y1 > y2;
        log3 = y2 > y1;
        if (log1 && log2)
            peaks(:, counter + 1) = [];
            c = c - 1;
        elseif (log1 && log3)
            peaks(:, counter) = [];
            c = c - 1;
        else
            counter = counter + 1;
        end
    end
end

function [mat] = getWaves(peaks, minT, yVec, xVec,
myTitle)
% getWaves Splits velocity data into valid single
waveforms and stores them
% in a matrix. Invalid waveforms will be discarded
[~, c] = size(peaks);
startVec = zeros(1, c);
remVec = [];
% Iterates through each peak to extract its wave form
for ndx = 1:c
    ind = find(peaks(2, ndx) == xVec);
    stopper = true;
%     Heads backward from the peak to determine the
wave's start
    while stopper
        ind = ind - 1;
```

```
        if (ind <=1)
            remVec = [remVec, ndx];
            stopper = false;
        else
            y1 = yVec(ind);
            y2 = yVec(ind - 1);
            diff = y2 - y1;
            if (y2 > minT && diff > 0) %Will remove
this peak b/c it indicates an artifact in the wave
%                 remVec = [remVec, ndx];
            elseif (y2 < minT && diff > 0) %Stores this
start index
                startVec(1,ndx) = ind;
                stopper = false;
            elseif (ind <= 2) %Will remove this wave
because it cannot have a start
                remVec = [remVec, ndx];
                stopper = false;
            elseif (ndx > 1) %Prevents the start of
current wave from going beyond previous wave
                if (ind <= startVec(ndx - 1))
                    startVec(1,ndx) = ind;
                    stopper = false;
                end
            end
        end
    end
end
remVec = unique(remVec);
endVec = zeros(1,c);
diffVec = zeros(1,c-1);
%Generates end of wave index vector and difference
vector
for ndx = 1:c - 1
    endVec(ndx) = startVec(ndx + 1);
    diffVec(ndx) = peaks(2, ndx + 1) - peaks(2, ndx);
end
[~, c2] = size(xVec);
endVec(end) = c2;

peaks = [peaks; startVec; endVec];
diff2 = endVec - startVec;
avg2 = mean(diff2);
dev2 = std(diff2);
```

```
lB2 = avg2 - (1.5 * dev2);
uB2 = avg2 + (2.5 * dev2);
lB2 = floor(lB2);
uB2 = floor(uB2);
if (any(strcmp(myTitle, {'WT : 6W : 118 : LICA'})))
    uB2 = uB2 - 5;
end
if (any(strcmp(myTitle, {'SS : 12W : 036 : LICA', 'SS :
12W : 036 : RICA', 'SS : 24W : 025 : RCCA', 'SS : 4W :
101 : RICA', 'WT : 24W : 111 : LCCA', 'WT : 6W : 114 :
LICA'})))
    uB2 = uB2 - 20;
end
if (any(strcmp(myTitle, {'SS : 4W : 095 : LICA'})))
    uB2 = uB2 - 27;
end
if (any(strcmp(myTitle, {'AS : 6W : 135 : RICA', 'SS :
12W : 045 : LICA', 'SS : 24W : 068 : RCCA', 'WT : 4W :
125 : LCCA', 'WT : 6W : 116 : LICA', 'WT : 6W : 119 :
LICA'})))
    uB2 = uB2 - 50;
end
if (any(strcmp(myTitle, {'WT : 24W : 110 : RCCA', 'WT :
24W : 113 : RICA'})))
    uB2 = uB2 - 100;
end
if (any(strcmp(myTitle, {'SS : 24W : 068 : LCCA', 'SS :
12W : 037 : LICA', 'AS : 6W : 138 : LICA', 'WT : 24W :
111 : RCCA'})))
    uB2 = uB2 - 175;
end
if (any(strcmp(myTitle, {'SS : 6W : 069 : RCCA', 'SS :
24W : 027 : LCCA', 'SS : 6W : 128 : LICA', 'WT : 4W :
123 : LICA', 'WT : 6W : 116 : LCCA'})))
    lB2 = lB2 - 2;
end
if (any(strcmp(myTitle, {'AS : 6W : 135 : RICA', 'SS :
12W : 036 : LICA', 'SS : 24W : 003 : RCCA', 'SS : 12W :
045 : RCCA', 'SS : 4W : 101 : RICA', 'WT : 24W : 109 :
RICA', 'WT : 4W : 123 : LCCA', 'WT : 6W : 114 : LICA',
'WT : 6W : 116 : LICA'})))
    lB2 = lB2 + 20;
end
```

```
if (any(strcmp(myTitle, {'AS : 12W : 091 : LICA', 'AS :
6W : 086 : RICA', 'AS : 6W : 073 : RICA', 'AS : 6W :
097 : LICA', 'WT : 24W : 111 : RICA', 'WT : 4W : 125 :
RICA', 'WT : 6W : 119 : LICA'})))
    lB2 = lB2 + 50;
end
if (any(strcmp(myTitle, {'SS : 12W : 037 : LICA', 'SS :
12W : 045 : LICA', 'AS : 4W : 099 : RICA', 'WT : 24W :
112 : LICA', 'WT : 24W : 113 : RICA', 'WT : 6W : 114 :
RICA'})))
    lB2 = lB2 + 100;
end
for ndx = 1:c
    val = diff2(ndx);
%     Removes waves that are too short or drastically
too longwhen compared to the lengths of the
%     other vectors
    if (val < lB2 || val > uB2)
        remVec = [remVec, ndx];
    end
end
remVec = unique(remVec);
peaks(:, remVec) = []; %Removes the bad wave forms
[~, c3] = size(peaks);
% Stores the wave forms in a cell array
mat = cell(c3, 1);
for ndx = 1:c3
    v1 = peaks(3, ndx);
    v2 = peaks(4, ndx) - 1;
    range = v1:v2;
    xWave = xVec(range);
    try
    xWave = xWave - xWave(1);
    catch
        stop = false;
    end
    yWave = yVec(peaks(3, ndx) : peaks(4, ndx) - 1);
    newCell = {[yWave; xWave]};
    mat(ndx, 1) = newCell;
end
end
```

REFERENCES

[1] R. J. Adams, V. C. McKie, L. Hsu, B. Files, E. Vichinsky, C. Pegelow, *et al.*, "Prevention of a first stroke by transfusions in children with sickle, cell anemia and abnormal results on transcranial Doppler ultrasonography," *New England Journal of Medicine,* vol. 339, pp. 5-11, Jul 2 1998.

[2] C. J. Earley, S. J. Kittner, B. R. Feeser, J. Gardner, A. Epstein, M. A. Wozniak, *et al.*, "Stroke in children and sickle-cell disease: Baltimore-Washington Cooperative Young Stroke Study," *Neurology,* vol. 51, pp. 169-76, Jul 1998.

[3] M. R. DeBaun, F. D. Armstrong, R. C. McKinstry, R. E. Ware, E. Vichinsky, and F. J. Kirkham, "Silent cerebral infarcts: a review on a prevalent and progressive cause of neurologic injury in sickle cell anemia," *Blood,* vol. 119, pp. 4587-96, May 17 2012.

[4] L. Boros, C. Thomas, and W. J. Weiner, "Large cerebral vessel disease in sickle cell anaemia," *J Neurol Neurosurg Psychiatry,* vol. 39, pp. 1236-9, Dec 1976.

[5] R. B. Francis, "Large-vessel occlusion in sickle cell disease: pathogenesis, clinical consequences, and therapeutic implications," *Med Hypotheses,* vol. 35, pp. 88-95, Jun 1991.

[6] M. R. Abboud, J. Cure, S. Granger, D. Gallagher, L. Hsu, W. Wang, *et al.*, "Magnetic resonance angiography in children with sickle cell disease and abnormal transcranial Doppler ultrasonography findings enrolled in the STOP study," *Blood,* vol. 103, pp. 2822-6, Apr 1 2004.

[7] D. N. Ku, D. P. Giddens, C. K. Zarins, and S. Glagov, "Pulsatile flow and atherosclerosis in the human carotid bifurcation. Positive correlation between plaque location and low oscillating shear stress," *Arteriosclerosis,* vol. 5, pp. 293-302, May-Jun 1985.

[8] A. M. Malek, S. L. Alper, and S. Izumo, "Hemodynamic shear stress and its role in atherosclerosis," *JAMA,* vol. 282, pp. 2035-42, Dec 1 1999.

[9] C. K. Zarins, D. P. Giddens, B. K. Bharadvaj, V. S. Sottiurai, R. F. Mabon, and S. Glagov, "Carotid bifurcation atherosclerosis. Quantitative correlation of plaque localization with flow velocity profiles and wall shear stress," *Circ Res,* vol. 53, pp. 502-14, Oct 1983.

[10] S. Bacigaluppi, M. Piccinelli, L. Antiga, A. Veneziani, T. Passerini, P. Rampini, *et al.*, "Factors affecting formation and rupture of intracranial saccular aneurysms," *Neurosurgical Review,* vol. 37, pp. 1-14, Jan 2014.

[11] K. L. Hassell, "Population estimates of sickle cell disease in the U.S," *Am J Prev Med,* vol. 38, pp. S512-21, Apr 2010.

[12] S. K. Ballas, "The cost of health care for patients with sickle cell disease," *American Journal of Hematology,* vol. 84, pp. 320-322, Jun 2009.

[13] X. R. Lu, D. K. Wood, and J. M. Higgins, "Deoxygenation Reduces Sickle Cell Blood Flow at Arterial Oxygen Tension," *Biophysical Journal,* vol. 110, pp. 2751-2758, Jun 21 2016.

[14] O. S. Platt, D. J. Brambilla, W. F. Rosse, P. F. Milner, O. Castro, M. H. Steinberg, *et al.*, "Mortality in sickle cell disease. Life expectancy and risk factors for early death," *N Engl J Med,* vol. 330, pp. 1639-44, Jun 9 1994.

[15] S. Kapoor, J. A. Little, and L. H. Pecker, "Advances in the Treatment of Sickle Cell Disease," *Mayo Clin Proc,* vol. 93, pp. 1810-1824, Dec 2018.
[16] H. F. Bunn, "Pathogenesis and treatment of sickle cell disease," *N Engl J Med,* vol. 337, pp. 762-9, Sep 11 1997.
[17] C. J. Moran, M. J. Siegel, and M. R. DeBaun, "Sickle cell disease: imaging of cerebrovascular complications," *Radiology,* vol. 206, pp. 311-21, Feb 1998.
[18] S. Chien, S. Usami, and J. F. Bertles, "Abnormal rheology of oxygenated blood in sickle cell anemia," *J Clin Invest,* vol. 49, pp. 623-34, Apr 1970.
[19] S. Chien, S. Usami, R. J. Dellenback, and M. I. Gregersen, "Blood Viscosity: Influence of Erythrocyte Deformation," *Science,* vol. 157, pp. 827-829, Aug 18 1967.
[20] S. Chien, S. Usami, R. J. Dellenback, M. I. Gregersen, L. B. Nanninga, and M. M. Guest, "Blood Viscosity: Influence of Erythrocyte Aggregation," *Science,* vol. 157, pp. 829-831, Aug 18 1967.
[21] G. B. Nash, C. S. Johnson, and H. J. Meiselman, "Mechanical properties of oxygenated red blood cells in sickle cell (HbSS) disease," *Blood,* vol. 63, pp. 73-82, Jan 1984.
[22] J. F. Bertles and J. Dobler, "Reversible and irreversible sickling: a distinction by electron microscopy," *Blood,* vol. 33, pp. 884-98, Jun 1969.
[23] P. R. McCurdy, "32-DFP and 51-Cr for measurement of red cell life span in abnormal hemoglobin syndromes," *Blood,* vol. 33, pp. 214-24, Feb 1969.
[24] J. S. Gibson and D. C. Rees, "How benign is sickle cell trait?," *Ebiomedicine,* vol. 11, pp. 21-+, Sep 2016.
[25] S. R. Jones, R. A. Binder, and E. M. Donowho, Jr., "Sudden death in sickle-cell trait," *N Engl J Med,* vol. 282, pp. 323-5, Feb 5 1970.
[26] J. C. Goldsmith, V. L. Bonham, C. H. Joiner, G. J. Kato, A. S. Noonan, and M. H. Steinberg, "Framing the research agenda for sickle cell trait: building on the current understanding of clinical events and their potential implications," *Am J Hematol,* vol. 87, pp. 340-6, Mar 2012.
[27] R. J. Adams, V. C. McKie, D. Brambilla, E. Carl, D. Gallagher, F. T. Nichols, *et al.*, "Stroke prevention trial in sickle cell anemia," *Control Clin Trials,* vol. 19, pp. 110-29, Feb 1998.
[28] J. A. Switzer, D. C. Hess, F. T. Nichols, and R. J. Adams, "Pathophysiology and treatment of stroke in sickle-cell disease: present and future," *Lancet Neurol,* vol. 5, pp. 501-12, Jun 2006.
[29] D. K. Kaul, M. E. Fabry, and R. L. Nagel, "Microvascular sites and characteristics of sickle cell adhesion to vascular endothelium in shear flow conditions: pathophysiological implications," *Proc Natl Acad Sci U S A,* vol. 86, pp. 3356-60, May 1989.
[30] S. Lanzkron, C. P. Carroll, and C. Haywood, "Mortality Rates and Age at Death from Sickle Cell Disease: US, 1979-2005," *Public Health Reports,* vol. 128, pp. 110-116, Mar-Apr 2013.
[31] M. J. Stuart and R. L. Nagel, "Sickle-cell disease," *Lancet,* vol. 364, pp. 1343-60, Oct 9-15 2004.
[32] D. C. Rees, T. N. Williams, and M. T. Gladwin, "Sickle-cell disease," *Lancet,* vol. 376, pp. 2018-31, Dec 11 2010.

[33] C. A. Hillery and J. A. Panepinto, "Pathophysiology of stroke in sickle cell disease," *Microcirculation,* vol. 11, pp. 195-208, Mar 2004.
[34] C. Hillery and J. Panepinto, "Pathophysiology of Stroke in Sickle Cell Disease," *Microcirculation,* vol. 11, pp. 195-208, Mar 1 2004.
[35] R. J. Adams, D. Brambilla, and I. Optimizing Primary Stroke Prevention in Sickle Cell Anemia Trial, "Discontinuing prophylactic transfusions used to prevent stroke in sickle cell disease," *N Engl J Med,* vol. 353, pp. 2769-78, Dec 29 2005.
[36] R. J. Adams, V. C. McKie, L. Hsu, B. Files, E. Vichinsky, C. Pegelow, *et al.*, "Prevention of a first stroke by transfusions in children with sickle cell anemia and abnormal results on transcranial Doppler ultrasonography," *N Engl J Med,* vol. 339, pp. 5-11, Jul 2 1998.
[37] I. Prohovnik, A. Hurlet-Jensen, R. Adams, D. De Vivo, and S. G. Pavlakis, "Hemodynamic etiology of elevated flow velocity and stroke in sickle-cell disease," *J Cereb Blood Flow Metab,* vol. 29, pp. 803-10, Apr 2009.
[38] R. J. Adams, F. T. Nichols, R. Aaslid, V. C. Mckie, K. Mckie, E. Carl, *et al.*, "Cerebral Vessel Stenosis in Sickle-Cell Disease - Criteria for Detection by Transcranial Doppler," *American Journal of Pediatric Hematology Oncology,* vol. 12, pp. 277-282, Fal 1990.
[39] A. S. Neish, D. E. Blews, C. A. Simms, R. K. Merritt, and A. J. Spinks, "Screening for stroke in sickle cell anemia: comparison of transcranial Doppler imaging and nonimaging US techniques," *Radiology,* vol. 222, pp. 709-14, Mar 2002.
[40] N. Venketasubramanian, I. Prohovnik, A. Hurlet, J. P. Mohr, and S. Piomelli, "Middle cerebral artery velocity changes during transfusion in sickle cell anemia," *Stroke,* vol. 25, pp. 2153-8, Nov 1994.
[41] M. T. Lee, S. Piomelli, S. Granger, S. T. Miller, S. Harkness, D. J. Brambilla, *et al.*, "Stroke Prevention Trial in Sickle Cell Anemia (STOP): extended follow-up and final results," *Blood,* vol. 108, pp. 847-52, Aug 1 2006.
[42] J. S. Hankins, G. L. Fortner, M. B. McCarville, M. P. Smeltzer, W. C. Wang, C. S. Li, *et al.*, "The natural history of conditional transcranial Doppler flow velocities in children with sickle cell anaemia," *Br J Haematol,* vol. 142, pp. 94-9, Jul 2008.
[43] K. H. Merkel, P. L. Ginsberg, J. C. Parker, Jr., and M. J. Post, "Cerebrovascular disease in sickle cell anemia: a clinical, pathological and radiological correlation," *Stroke,* vol. 9, pp. 45-52, Jan-Feb 1978.
[44] D. N. Ku, "Blood flow in arteries," *Annual Review of Fluid Mechanics,* vol. 29, pp. 399-434, 1997.
[45] E. S. Roach, "Etiology of stroke in children," *Semin Pediatr Neurol,* vol. 7, pp. 244-60, Dec 2000.
[46] A. M. Shaaban and A. J. Duerinckx, "Wall shear stress and early atherosclerosis: a review," *AJR Am J Roentgenol,* vol. 174, pp. 1657-65, Jun 2000.
[47] R. A. Vogel, "Coronary risk factors, endothelial function, and atherosclerosis: a review," *Clin Cardiol,* vol. 20, pp. 426-32, May 1997.
[48] R. Ross, "The pathogenesis of atherosclerosis--an update," *N Engl J Med,* vol. 314, pp. 488-500, Feb 20 1986.
[49] J. J. Chiu, C. N. Chen, P. L. Lee, C. T. Yang, H. S. Chuang, S. Chien, *et al.*, "Analysis of the effect of disturbed flow on monocytic adhesion to endothelial cells," *Journal of Biomechanics,* vol. 36, pp. 1883-1895, Dec 2003.

[50] A. R. Riela and E. S. Roach, "Etiology of stroke in children," *J Child Neurol,* vol. 8, pp. 201-20, Jul 1993.
[51] W. C. Wang, S. G. Pavlakis, K. J. Helton, R. C. McKinstry, J. F. Casella, R. J. Adams, *et al.*, "MRI abnormalities of the brain in one-year-old children with sickle cell anemia," *Pediatr Blood Cancer,* vol. 51, pp. 643-6, Nov 2008.
[52] K. Ohene-Frempong, S. J. Weiner, L. A. Sleeper, S. T. Miller, S. Embury, J. W. Moohr, *et al.*, "Cerebrovascular accidents in sickle cell disease: rates and risk factors," *Blood,* vol. 91, pp. 288-94, Jan 1 1998.
[53] R. J. Adams, D. J. Brambilla, S. Granger, D. Gallagher, E. Vichinsky, M. R. Abboud, *et al.*, "Stroke and conversion to high risk in children screened with transcranial Doppler ultrasound during the STOP study," *Blood,* vol. 103, pp. 3689-94, May 15 2004.
[54] C. H. Pegelow, R. J. Adams, V. McKie, M. Abboud, B. Berman, S. T. Miller, *et al.*, "Risk of recurrent stroke in patients with sickle cell disease treated with erythrocyte transfusions," *J Pediatr,* vol. 126, pp. 896-9, Jun 1995.
[55] E. P. Vichinsky, C. M. Haberkern, L. Neumayr, A. N. Earles, D. Black, M. Koshy, *et al.*, "A comparison of conservative and aggressive transfusion regimens in the perioperative management of sickle cell disease. The Preoperative Transfusion in Sickle Cell Disease Study Group," *N Engl J Med,* vol. 333, pp. 206-13, Jul 27 1995.
[56] S. A. Zimmerman, W. H. Schultz, J. S. Davis, C. V. Pickens, N. A. Mortier, T. A. Howard, *et al.*, "Sustained long-term hematologic efficacy of hydroxyurea at maximum tolerated dose in children with sickle cell disease," *Blood,* vol. 103, pp. 2039-45, Mar 15 2004.
[57] S. Charache, M. L. Terrin, R. D. Moore, G. J. Dover, F. B. Barton, S. V. Eckert, *et al.*, "Effect of hydroxyurea on the frequency of painful crises in sickle cell anemia. Investigators of the Multicenter Study of Hydroxyurea in Sickle Cell Anemia," *N Engl J Med,* vol. 332, pp. 1317-22, May 18 1995.
[58] R. E. Ware, B. R. Davis, W. H. Schultz, R. C. Brown, B. Aygun, S. Sarnaik, *et al.*, "Hydroxycarbamide versus chronic transfusion for maintenance of transcranial doppler flow velocities in children with sickle cell anaemia-TCD With Transfusions Changing to Hydroxyurea (TWiTCH): a multicentre, open-label, phase 3, non-inferiority trial," *Lancet,* vol. 387, pp. 661-70, Feb 13 2016.
[59] R. E. Ware, R. W. Helms, and S. W. Investigators, "Stroke With Transfusions Changing to Hydroxyurea (SWiTCH)," *Blood,* vol. 119, pp. 3925-32, Apr 26 2012.
[60] R. V. Gardner, "Sickle Cell Disease: Advances in Treatment," *Ochsner J,* vol. 18, pp. 377-389, Winter 2018.
[61] M. Bhatia and S. Sheth, "Hematopoietic stem cell transplantation in sickle cell disease: patient selection and special considerations," *J Blood Med,* vol. 6, pp. 229-38, 2015.
[62] M. M. Hsieh, E. M. Kang, C. D. Fitzhugh, M. B. Link, C. D. Bolan, R. Kurlander, *et al.*, "Allogeneic hematopoietic stem-cell transplantation for sickle cell disease," *N Engl J Med,* vol. 361, pp. 2309-17, Dec 10 2009.
[63] E. Gluckman, B. Cappelli, F. Bernaudin, M. Labopin, F. Volt, J. Carreras, *et al.*, "Sickle cell disease: an international survey of results of HLA-identical sibling hematopoietic stem cell transplantation," *Blood,* vol. 129, pp. 1548-1556, Mar 16 2017.

[64] W. C. Mentzer, S. Heller, P. R. Pearle, E. Hackney, and E. Vichinsky, "Availability of related donors for bone marrow transplantation in sickle cell anemia," *Am J Pediatr Hematol Oncol,* vol. 16, pp. 27-9, Feb 1994.

[65] J. A. Ribeil, S. Hacein-Bey-Abina, E. Payen, A. Magnani, M. Semeraro, E. Magrin, *et al.*, "Gene Therapy in a Patient with Sickle Cell Disease," *N Engl J Med,* vol. 376, pp. 848-855, Mar 2 2017.

[66] M. D. Hoban, D. Lumaquin, C. Y. Kuo, Z. Romero, J. Long, M. Ho, *et al.*, "CRISPR/Cas9-Mediated Correction of the Sickle Mutation in Human CD34+ cells," *Mol Ther,* vol. 24, pp. 1561-9, Sep 2016.

[67] L. Ye, J. Wang, Y. Tan, A. I. Beyer, F. Xie, M. O. Muench, *et al.*, "Genome editing using CRISPR-Cas9 to create the HPFH genotype in HSPCs: An approach for treating sickle cell disease and beta-thalassemia," *Proc Natl Acad Sci U S A,* vol. 113, pp. 10661-5, Sep 20 2016.

[68] L. Shariati, H. Khanahmad, M. Salehi, Z. Hejazi, I. Rahimmanesh, M. A. Tabatabaiefar, *et al.*, "Genetic disruption of the KLF1 gene to overexpress the gamma-globin gene using the CRISPR/Cas9 system," *J Gene Med,* vol. 18, pp. 294-301, Oct 2016.

[69] J. J. Chiu and S. Chien, "Effects of disturbed flow on vascular endothelium: pathophysiological basis and clinical perspectives," *Physiol Rev,* vol. 91, pp. 327-87, Jan 2011.

[70] P. Rajendran, T. Rengarajan, J. Thangavel, Y. Nishigaki, D. Sakthisekaran, G. Sethi, *et al.*, "The vascular endothelium and human diseases," *Int J Biol Sci,* vol. 9, pp. 1057-69, 2013.

[71] T. Asakura and T. Karino, "Flow Patterns and Spatial-Distribution of Atherosclerotic Lesions in Human Coronary-Arteries," *Circulation Research,* vol. 66, pp. 1045-1066, Apr 1990.

[72] T. Alexy, E. Pais, J. K. Armstrong, H. J. Meiselman, C. S. Johnson, and T. C. Fisher, "Rheologic behavior of sickle and normal red blood cell mixtures in sickle plasma: implications for transfusion therapy," *Transfusion,* vol. 46, pp. 912-918, Jun 2006.

[73] S. Chien, S. Usami, and J. F. Bertles, "Abnormal Rheology of Oxygenated Blood in Sickle Cell Anemia," *Journal of Clinical Investigation,* vol. 49, pp. 623-&, 1970.

[74] E. A. Schmalzer, J. O. Lee, A. K. Brown, S. Usami, and S. Chien, "Viscosity of Mixtures of Sickle and Normal Red-Cells at Varying Hematocrit Levels - Implications for Transfusion," *Transfusion,* vol. 27, pp. 228-233, May-Jun 1987.

[75] D. P. Giddens, C. K. Zarins, and S. Glagov, "The role of fluid mechanics in the localization and detection of atherosclerosis," *J Biomech Eng,* vol. 115, pp. 588-94., 1993.

[76] M. O. Platt, R. F. Ankeny, and H. Jo, "Laminar shear stress inhibits cathepsin L activity in endothelial cells," *Arterioscler Thromb Vasc Biol,* vol. 26, pp. 1784-90, Aug 2006.

[77] M. O. Platt, R. F. Ankeny, G. P. Shi, D. Weiss, J. D. Vega, W. R. Taylor, *et al.*, "Expression of cathepsin K is regulated by shear stress in cultured endothelial cells and is increased in endothelium in human atherosclerosis," *Am J Physiol Heart Circ Physiol,* vol. 292, pp. H1479-86, Mar 2007.

[78] M. O. Platt and W. A. Shockey, "Endothelial cells and cathepsins: Biochemical and biomechanical regulation," *Biochimie,* vol. 122, pp. 314-23, Mar 2016.
[79] Y. C. Boo, G. Sorescu, N. Boyd, I. Shiojima, K. Walsh, J. Du, *et al.*, "Shear stress stimulates phosphorylation of endothelial nitric-oxide synthase at Ser1179 by Akt-independent mechanisms: role of protein kinase A," *J Biol Chem,* vol. 277, pp. 3388-96, Feb 1 2002.
[80] D. G. Harrison, J. Widder, I. Grumbach, W. Chen, M. Weber, and C. Searles, "Endothelial mechanotransduction, nitric oxide and vascular inflammation," *J Intern Med,* vol. 259, pp. 351-63, Apr 2006.
[81] S. Dimmeler, C. Hermann, J. Galle, and A. M. Zeiher, "Upregulation of superoxide dismutase and nitric oxide synthase mediates the apoptosis-suppressive effects of shear stress on endothelial cells," *Arterioscler Thromb Vasc Biol,* vol. 19, pp. 656-64, Mar 1999.
[82] S. Mohan, N. Mohan, A. J. Valente, and E. A. Sprague, "Regulation of low shear flow-induced HAEC VCAM-1 expression and monocyte adhesion," *Am J Physiol,* vol. 276, pp. C1100-7, May 1999.
[83] M. I. Cybulsky, K. Iiyama, H. Li, S. Zhu, M. Chen, M. Iiyama, *et al.*, "A major role for VCAM-1, but not ICAM-1, in early atherosclerosis," *J Clin Invest,* vol. 107, pp. 1255-62, May 2001.
[84] M. O. Platt, R. F. Ankeny, and H. J. Jo, "Laminar shear stress inhibits cathepsin L activity in endothelial cells," *Arteriosclerosis Thrombosis and Vascular Biology,* vol. 26, pp. 1784-1790, Aug 2006.
[85] M. O. Platt, R. F. Ankeny, G. P. Shi, D. Weiss, J. D. Vega, W. R. Taylor, *et al.*, "Expression of cathepsin K is regulated by shear stress in cultured endothelial cells and is increased in endothelium in human atherosclerosis," *American Journal of Physiology-Heart and Circulatory Physiology,* vol. 292, pp. H1479-H1486, Mar 2007.
[86] D. A. Steinman, "Image-based computational fluid dynamics modeling in realistic arterial geometries," *Annals of Biomedical Engineering,* vol. 30, pp. 483-497, Apr 2002.
[87] B. K. Lee, "Computational fluid dynamics in cardiovascular disease," *Korean Circ J,* vol. 41, pp. 423-30, Aug 2011.
[88] S. K. Jeong and R. S. Rosenson, "Shear rate specific blood viscosity and shear stress of carotid artery duplex ultrasonography in patients with lacunar infarction," *Bmc Neurology,* vol. 13, Apr 18 2013.
[89] J. K. Cutnell, Johnson *Physics, Fourth Edition*: Wiley, 1998.
[90] C. C. Botar-Jid, P. S. Agachi, and S. Clichici, "Computational fluid dynamics applied to study the hemodynamics in sangvin vessels. Case study - the portal system," *19th European Symposium on Computer Aided Process Engineering,* vol. 26, pp. 677-682, 2009.
[91] N. Westerhof, G. Elzinga, and P. Sipkema, "An artificial arterial system for pumping hearts," *J Appl Physiol,* vol. 31, pp. 776-81, Nov 1971.
[92] I. E. Vignon-Clementel, C. A. Figueroa, K. E. Jansen, and C. A. Taylor, "Outflow boundary conditions for three-dimensional finite element modeling of blood flow and pressure in arteries," *Computer Methods in Applied Mechanics and Engineering,* vol. 195, pp. 3776-3796, 2006.

[93] R. J. Adams, D. J. Brambilla, S. Granger, D. Gallagher, E. Vichinsky, M. R. Abboud, *et al.*, "Stroke and conversion to high risk in children screened with transcranial Doppler ultrasound during the STOP study," *Blood,* vol. 103, pp. 3689-94, May 15 2004.

[94] R. Adams, V. Mckie, F. Nichols, E. Carl, D. L. Zhang, K. Mckie, *et al.*, "The Use of Transcranial Ultrasonography to Predict Stroke in Sickle-Cell Disease," *New England Journal of Medicine,* vol. 326, pp. 605-610, Feb 27 1992.

[95] R. J. Adams, F. T. Nichols, R. Figueroa, V. McKie, and T. Lott, "Transcranial Doppler correlation with cerebral angiography in sickle cell disease," *Stroke,* vol. 23, pp. 1073-7, Aug 1992.

[96] S. Takeuchi and T. Karino, "Flow patterns and distributions of fluid velocity and wall shear stress in the human internal carotid and middle cerebral arteries," *World Neurosurg,* vol. 73, pp. 174-85; discussion e27, Mar 2010.

[97] V. M. Pereira, O. Brina, A. M. Gonzales, A. P. Narata, P. Bijlenga, K. Schaller, *et al.*, "Evaluation of the influence of inlet boundary conditions on computational fluid dynamics for intracranial aneurysms: A virtual experiment," *Journal of Biomechanics,* vol. 46, pp. 1531-1539, May 31 2013.

[98] L. Antiga, B. Ene-Iordache, L. Caverni, G. P. Cornalba, and A. Remuzzi, "Geometric reconstruction for computational mesh generation of arterial bifurcations from CT angiography," *Computerized Medical Imaging and Graphics,* vol. 26, pp. 227-235, Jul-Aug 2002.

[99] M. Schoning, J. Walter, and P. Scheel, "Estimation of Cerebral Blood-Flow through Color Duplex Sonography of the Carotid and Vertebral Arteries in Healthy-Adults," *Stroke,* vol. 25, pp. 17-22, Jan 1994.

[100] E. B. Ringelstein, B. Kahlscheuer, E. Niggemeyer, and S. M. Otis, "Transcranial Doppler sonography: anatomical landmarks and normal velocity values," *Ultrasound Med Biol,* vol. 16, pp. 745-61, 1990.

[101] A. S. Neish, D. E. Blews, C. A. Simms, R. K. Merritt, and A. J. Spinks, "Screening for stroke in sickle cell anemia: Comparison of transcranial Doppler Imaging and nonimaging US techniques," *Radiology,* vol. 222, pp. 709-714, Mar 2002.

[102] H. H. Billett, "Hemoglobin and Hematocrit," in *Clinical Methods: The History, Physical, and Laboratory Examinations*, H. K. Walker, W. D. Hall, and J. W. Hurst, Eds., 3rd ed Boston, 1990.

[103] G. A. Barabino, M. O. Platt, and D. K. Kaul, "Sickle cell biomechanics," *Annu Rev Biomed Eng,* vol. 12, pp. 345-67, Aug 15 2010.

[104] S. P. Wu, S. Ringgaard, S. Oyre, M. S. Hansen, S. Rasmus, and E. M. Pedersen, "Wall shear rates differ between the normal carotid, femoral, and brachial arteries: An in vivo MRI study," *Journal of Magnetic Resonance Imaging,* vol. 19, pp. 188-193, Feb 2004.

[105] T. G. Papaioannou and C. Stefanadis, "Vascular wall shear stress: basic principles and methods," *Hellenic J Cardiol,* vol. 46, pp. 9-15, Jan-Feb 2005.

[106] D. K. Kaul, M. E. Fabry, P. Windisch, S. Baez, and R. L. Nagel, "Erythrocytes in Sickle-Cell-Anemia Are Heterogeneous in Their Rheological and Hemodynamic Characteristics," *Journal of Clinical Investigation,* vol. 72, pp. 22-31, 1983.

[107] R. G. Steen, X. Xiong, R. K. Mulhern, J. W. Langston, and W. C. Wang, "Subtle brain abnormalities in children with sickle cell disease: relationship to blood hematocrit," *Ann Neurol,* vol. 45, pp. 279-86, Mar 1999.
[108] S. Chien, S. Usami, R. J. Dellenback, and M. I. Gregersen, "Blood viscosity: influence of erythrocyte deformation," *Science,* vol. 157, pp. 827-9, Aug 18 1967.
[109] S. Chien, S. Usami, R. J. Dellenback, M. I. Gregersen, L. B. Nanninga, and M. M. Guest, "Blood viscosity: influence of erythrocyte aggregation," *Science,* vol. 157, pp. 829-31, Aug 18 1967.
[110] S. Tabakova, N. Kutev, and S. Radev, "Application of the Carreau Viscosity Model to the Oscillatory Flow in Blood Vessels," *41st International Conference Applications of Mathematics in Engineering and Economics (Amee'15),* vol. 1690, 2015.
[111] S. S. Shibeshi and W. E. Collins, "The rheology of blood flow in a branched arterial system," *Applied Rheology,* vol. 15, pp. 398-405, 2005.
[112] F. J. H. Gijsen, E. Allanic, F. N. van de Vosse, and J. D. Janssen, "The influence of the non-Newtonian properties of blood on the flow in large arteries: unsteady flow in a 90 degrees curved tube," *Journal of Biomechanics,* vol. 32, pp. 705-713, Jul 1999.
[113] L. S. Antiga, S, "VMTK: Vascular Modeling Toolkit," *http://www.vmtk.org/,* 2009.
[114] M. Piccinelli, A. Veneziani, D. A. Steinman, A. Remuzzi, and L. Antiga, "A framework for geometric analysis of vascular structures: application to cerebral aneurysms," *IEEE Trans Med Imaging,* vol. 28, pp. 1141-55, Aug 2009.
[115] M. E. Moghadam, Y. Bazilevs, T. Y. Hsia, I. E. Vignon-Clementel, A. L. Marsden, and M. C. H. Allianc, "A comparison of outlet boundary treatments for prevention of backflow divergence with relevance to blood flow simulations," *Computational Mechanics,* vol. 48, pp. 277-291, Sep 2011.
[116] A. Veneziani and C. Vergara, "An approximate method for solving incompressible Navier-Stokes problems with flow rate conditions," *Computer Methods in Applied Mechanics and Engineering,* vol. 196, pp. 1685-1700, 2007.
[117] D. Maffiodo, G. De Nisco, D. Gallo, A. Audenino, U. Morbiducci, and C. Ferraresi, "A reduced-order model-based study on the effect of intermittent pneumatic compression of limbs on the cardiovascular system," *Proceedings of the Institution of Mechanical Engineers Part H-Journal of Engineering in Medicine,* vol. 230, pp. 279-287, Apr 2016.
[118] J. Schöberl, "NETGEN An advancing front 2D/3D-mesh generator based on abstract rules," *Computing and visualization in science,* vol. 1, pp. 41-52, 1997.
[119] A. C. Guyton and J. E. Hall, *Textbook of medical physiology*, 10th ed. Philadelphia: Saunders, 2000.
[120] M. O. Platt and W. A. Shockey, "Endothelial cells and cathepsins: Biochemical and biomechanical regulation," *Biochimie,* Oct 13 2015.
[121] A. M. Khalifa and D. P. Giddens, "Characterization and evolution poststenotic flow disturbances," *J Biomech,* vol. 14, pp. 279-96, 1981.
[122] L. Boros, C. Thomas, and W. J. Weiner, "Large Cerebral Vessel Disease in Sickle-Cell Anemia," *Journal of Neurology Neurosurgery and Psychiatry,* vol. 39, pp. 1236-1239, 1976.

[123] K. H. H. Merkel, P. L. Ginsberg, J. C. Parker, and M. J. Donovanpost, "Cerebrovascular-Disease in Sickle-Cell Anemia - Clinical, Pathological and Radiological Correlation," *Stroke,* vol. 9, pp. 45-52, 1978.
[124] R. M. Fasano, E. R. Meier, and M. L. Hulbert, "Cerebral vasculopathy in children with sickle cell anemia," *Blood Cells Molecules and Diseases,* vol. 54, pp. 17-25, Jan 2015.
[125] J. D. Belcher, P. H. Marker, J. P. Weber, R. P. Hebbel, and G. M. Vercellotti, "Activated monocytes in sickle cell disease: potential role in the activation of vascular endothelium and vaso-occlusion," *Blood,* vol. 96, pp. 2451-9, Oct 1 2000.
[126] S. W. Lee, L. Antiga, J. D. Spence, and D. A. Steinman, "Geometry of the carotid bifurcation predicts its exposure to disturbed flow," *Stroke,* vol. 39, pp. 2341-7, Aug 2008.
[127] R. Aaslid, T. M. Markwalder, and H. Nornes, "Noninvasive transcranial Doppler ultrasound recording of flow velocity in basal cerebral arteries," *J Neurosurg,* vol. 57, pp. 769-74, Dec 1982.
[128] W. Reinke, P. Gaehtgens, and P. C. Johnson, "Blood viscosity in small tubes: effect of shear rate, aggregation, and sedimentation," *Am J Physiol,* vol. 253, pp. H540-7, Sep 1987.
[129] L. Bertagna, D'Elia, M., Perego, M., & Veneziani, A, *Data Assimilation in Cardiovascular Fluid–Structure Interaction Problems: An Introduction. In Fluid-Structure Interaction and Biomedical Applications*: Springer Basel, 2014.
[130] H. Yang, & Veneziani, A, "Variational estimation of cardiac conductivities by a data assimilation procedure," *Technical Report TR-2013-007, Math&CS, Emory University. to appear in Inverse Problems,* 2013.
[131] L. Bertagna and A. Veneziani, "A model reduction approach for the variational estimation of vascular compliance by solving an inverse fluid-structure interaction problem," *Inverse Problems,* vol. 30, May 2014.
[132] F. Bernaudin, S. Verlhac, C. Arnaud, A. Kamdem, M. Vasile, F. Kasbi, *et al.*, "Chronic and acute anemia and extracranial internal carotid stenosis are risk factors for silent cerebral infarcts in sickle cell anemia," *Blood,* vol. 125, pp. 1653-61, Mar 5 2015.
[133] M. Piccinelli, S. Bacigaluppi, E. Boccardi, B. Ene-Iordache, A. Remuzzi, A. Veneziani, *et al.*, "Geometry of the internal carotid artery and recurrent patterns in location, orientation, and rupture status of lateral aneurysms: an image-based computational study," *Neurosurgery,* vol. 68, pp. 1270-85; discussion 1285, May 2011.
[134] S. Okuyama, J. Okuyama, J. Okuyama, Y. Tamatsu, K. Shimada, H. Hoshi, *et al.*, "The arterial circle of Willis of the mouse helps to decipher secrets of cerebral vascular accidents in the human," *Med Hypotheses,* vol. 63, pp. 997-1009, 2004.
[135] T. M. Ryan, D. J. Ciavatta, and T. M. Townes, "Knockout-transgenic mouse model of sickle cell disease," *Science,* vol. 278, pp. 873-6, Oct 31 1997.
[136] L. L. Hsu, H. C. Champion, S. A. Campbell-Lee, T. J. Bivalacqua, E. A. Manci, B. A. Diwan, *et al.*, "Hemolysis in sickle cell mice causes pulmonary hypertension due to global impairment in nitric oxide bioavailability," *Blood,* vol. 109, pp. 3088-3098, Apr 1 2007.

[137] M. Aslan, T. M. Ryan, B. Adler, T. M. Townes, D. A. Parks, J. A. Thompson, *et al.*, "Oxygen radical inhibition of nitric oxide-dependent vascular function in sickle cell disease," *Proc Natl Acad Sci U S A,* vol. 98, pp. 15215-20, Dec 18 2001.
[138] L. S. Cahill, L. M. Gazdzinski, A. K. Y. Tsui, Y. Q. Zhou, S. Portnoy, E. Liu, *et al.*, "Functional and anatomical evidence of cerebral tissue hypoxia in young sickle cell anemia mice," *Journal of Cerebral Blood Flow and Metabolism,* vol. 37, pp. 994-1005, Mar 2017.
[139] H. I. Hyacinth, C. L. Sugihara, T. L. Spencer, D. R. Archer, and A. Y. Shih, "Higher prevalence of spontaneous cerebral vasculopathy and cerebral infarcts in a mouse model of sickle cell disease," *J Cereb Blood Flow Metab,* vol. 39, pp. 342-351, Feb 2017.
[140] R. P. Kennan, S. M. Suzuka, R. L. Nagel, and M. E. Fabry, "Decreased cerebral perfusion correlates with increased BOLD hyperoxia response in transgenic mouse models of sickle cell disease," *Magn Reson Med,* vol. 51, pp. 525-32, Mar 2004.
[141] W. Luo, E. J. Su, J. Wang, H. Wang, C. Guo, A. Pawar, *et al.*, "Increased stroke size following MCA occlusion in a mouse model of sickle cell disease," *Blood,* vol. 123, pp. 1965-7, Mar 20 2014.
[142] Y. Y. Sun, J. Lee, H. Huang, M. B. Wagner, C. H. Joiner, D. R. Archer, *et al.*, "Sickle Mice Are Sensitive to Hypoxia/Ischemia-Induced Stroke but Respond to Tissue-Type Plasminogen Activator Treatment," *Stroke,* vol. 48, pp. 3347-3355, Dec 2017.
[143] P. M. Keegan, O. P. Keifer, I. L. Parker, S. D. Keilholz, and M. O. Platt, "Spontaneous Strokes In Sickle Cell Transgenic Mice Captured Ex Vivo With Magnetic Resonance Imaging," *Stroke,* vol. 44, Feb 2013.
[144] B. G. Qian, R. F. Rudy, T. X. Cai, and R. Du, "Cerebral Artery Diameter in Inbred Mice Varies as a Function of Strain," *Frontiers in Neuroanatomy,* vol. 12, Feb 20 2018.
[145] J. Krejza, M. Arkuszewski, S. E. Kasner, J. Weigele, A. Ustymowicz, R. W. Hurst, *et al.*, "Carotid artery diameter in men and women and the relation to body and neck size," *Stroke,* vol. 37, pp. 1103-5, Apr 2006.
[146] J. W. Thuroff, W. Hort, and H. Lichti, "Diameter of coronary arteries in 36 species of mammalian from mouse to giraffe," *Basic Res Cardiol,* vol. 79, pp. 199-206, Mar-Apr 1984.
[147] C. L. Duvall, W. R. Taylor, D. Weiss, and R. E. Guldberg, "Quantitative microcomputed tomography analysis of collateral vessel development after ischemic injury," *American Journal of Physiology-Heart and Circulatory Physiology,* vol. 287, pp. H302-H310, Jul 2004.
[148] S. Ghanavati, J. P. Lerch, and J. G. Sled, "Automatic anatomical labeling of the complete cerebral vasculature in mouse models," *Neuroimage,* vol. 95, pp. 117-28, Jul 15 2014.
[149] C. J. Flurkey K, Harrison DE, *The Mouse in Biomedical Research* American College Laboratory Animal Medicine, 2007.
[150] T. Abruzzo, L. Tumialan, C. Chaalala, S. Kim, R. E. Guldberg, A. Lin, *et al.*, "Microscopic computed tomography imaging of the cerebral circulation in mice: Feasibility and pitfalls," *Synapse,* vol. 62, pp. 557-565, Aug 2008.

[151] Y. Huo, X. Guo, and G. S. Kassab, "The flow field along the entire length of mouse aorta and primary branches," *Ann Biomed Eng,* vol. 36, pp. 685-99, May 2008.
[152] H. Yanagisawa, E. C. Davis, B. C. Starcher, T. Ouchi, M. Yanagisawa, J. A. Richardson, *et al.*, "Fibulin-5 is an elastin-binding protein essential for elastic fibre development in vivo," *Nature,* vol. 415, pp. 168-171, Jan 10 2002.
[153] D. L. Mattson, "Comparison of arterial blood pressure in different strains of mice," *Am J Hypertens,* vol. 14, pp. 405-8, May 2001.
[154] L. Vaclavu, Z. A. V. Baldew, S. Gevers, H. Mutsaerts, K. Fijnvandraat, M. H. Cnossen, *et al.*, "Intracranial 4D flow magnetic resonance imaging reveals altered haemodynamics in sickle cell disease," *Br J Haematol,* vol. 180, pp. 432-442, Feb 2018.
[155] L. Xiao, B. Andemariam, P. Taxel, D. J. Adams, W. T. Zempsky, V. Dorcelus, *et al.*, "Loss of Bone in Sickle Cell Trait and Sickle Cell Disease Female Mice Is Associated With Reduced IGF-1 in Bone and Serum," *Endocrinology,* vol. 157, pp. 3036-46, Aug 2016.
[156] I. Prohovnik, S. G. Pavlakis, S. Piomelli, J. Bello, J. P. Mohr, S. Hilal, *et al.*, "Cerebral hyperemia, stroke, and transfusion in sickle cell disease," *Neurology,* vol. 39, pp. 344-8, Mar 1989.
[157] A. M. Bush, M. T. Borzage, S. Choi, L. Vaclavu, B. Tamrazi, A. J. Nederveen, *et al.*, "Determinants of resting cerebral blood flow in sickle cell disease," *Am J Hematol,* vol. 91, pp. 912-7, Sep 2016.
[158] P. D. Kosinski, P. L. Croal, J. Leung, S. Williams, I. Odame, G. M. Hare, *et al.*, "The severity of anaemia depletes cerebrovascular dilatory reserve in children with sickle cell disease: a quantitative magnetic resonance imaging study," *Br J Haematol,* vol. 176, pp. 280-287, Jan 2017.
[159] B. M. Altura and J. Weinberg, "Urethane and contraction of vascular smooth muscle," *Br J Pharmacol,* vol. 67, pp. 255-63, Oct 1979.
[160] H. Iida, H. Ohata, M. Iida, Y. Watanabe, and S. Dohi, "Isoflurane and sevoflurane induce vasodilation of cerebral vessels via ATP-sensitive K+ channel activation," *Anesthesiology,* vol. 89, pp. 954-60, Oct 1998.
[161] P. M. Keegan, S. Surapaneni, and M. O. Platt, "Sickle cell disease activates peripheral blood mononuclear cells to induce cathepsins k and v activity in endothelial cells," *Anemia,* vol. 2012, p. 201781, 2012.
[162] S. P. Dutta S, "Men and mice: Relating their ages," *Life Sci,* vol. 152, pp. 244-248, 2016.
[163] S. Spring, J. P. Lerch, M. K. Wetzel, A. C. Evans, and R. M. Henkelman, "Cerebral asymmetries in 12-week-old C57Bl/6J mice measured by magnetic resonance imaging," *Neuroimage,* vol. 50, pp. 409-15, Apr 1 2010.
[164] C. D. Murray, "The physiological principle of minimum work applied to the angle of branching of arteries.," *Journal of General Physiology,* vol. 9, pp. 835-841, Jul 1926.
[165] B. Trachet, J. Bols, G. De Santis, S. Vandenberghe, B. Loeys, and P. Segers, "The Impact of Simplified Boundary Conditions and Aortic Arch Inclusion on CFD Simulations in the Mouse Aorta: A Comparison With Mouse-specific Reference Data," *Journal of Biomechanical Engineering-Transactions of the Asme,* vol. 133, Dec 2011.

[166] T. F. Sherman, "On Connecting Large Vessels to Small - the Meaning of Murray Law," *Journal of General Physiology,* vol. 78, pp. 431-453, 1981.
[167] J. S. Lillie, A. S. Liberson, D. Mix, K. Q. Schwarz, A. Chandra, D. B. Phillips, *et al.*, "Pulse Wave Velocity Prediction and Compliance Assessment in Elastic Arterial Segments," *Cardiovascular Engineering and Technology,* vol. 6, pp. 49-58, Mar 2015.
[168] L. Aslanidou, B. Trachet, P. Reymond, R. A. Fraga-Silva, P. Segers, and N. Stergiopulos, "A 1D Model of the Arterial Circulation in Mice," *Altex-Alternatives to Animal Experimentation,* vol. 33, pp. 13-28, 2016.
[169] P. Scheel, C. Ruge, and M. Schoning, "Flow velocity and flow volume measurements in the extracranial carotid and vertebral arteries in healthy adults: reference data and the effects of age," *Ultrasound Med Biol,* vol. 26, pp. 1261-6, Oct 2000.
[170] B. Yazici, B. Erdogmus, and A. Tugay, "Cerebral blood flow measurements of the extracranial carotid and vertebral arteries with Doppler ultrasonography in healthy adults," *Diagn Interv Radiol,* vol. 11, pp. 195-8, Dec 2005.
[171] C. R. Deane, D. Goss, J. Bartram, K. R. Pohl, S. E. Height, N. Sibtain, *et al.*, "Extracranial internal carotid arterial disease in children with sickle cell anemia," *Haematologica,* vol. 95, pp. 1287-92, Aug 2010.
[172] M. T. Gladwin and V. Sachdev, "Cardiovascular abnormalities in sickle cell disease," *J Am Coll Cardiol,* vol. 59, pp. 1123-33, Mar 27 2012.
[173] J. Krejza, R. Chen, G. Romanowicz, J. L. Kwiatkowski, R. Ichord, M. Arkuszewski, *et al.*, "Sickle cell disease and transcranial Doppler imaging: inter-hemispheric differences in blood flow Doppler parameters," *Stroke,* vol. 42, pp. 81-6, Jan 2011.
[174] W. Sorteberg, I. A. Langmoen, K. F. Lindegaard, and H. Nornes, "Side-to-side differences and day-to-day variations of transcranial Doppler parameters in normal subjects," *J Ultrasound Med,* vol. 9, pp. 403-9, Jul 1990.
[175] R. Fahraeus and T. Lindqvist, "The viscosity of the blood in narrow capillary tubes," *American Journal of Physiology,* vol. 96, pp. 562-568, Mar 1931.
[176] C. P. Rivera, A. Veneziani, R. E. Ware, and M. O. Platt, "Original Research: Sickle cell anemia and pediatric strokes: Computational fluid dynamics analysis in the middle cerebral artery," *Exp Biol Med (Maywood),* vol. 241, pp. 755-65, Apr 2016.
[177] G. Dai, M. R. Kaazempur-Mofrad, S. Natarajan, Y. Zhang, S. Vaughn, B. R. Blackman, *et al.*, "Distinct endothelial phenotypes evoked by arterial waveforms derived from atherosclerosis-susceptible and -resistant regions of human vasculature," *Proc Natl Acad Sci U S A,* vol. 101, pp. 14871-6, Oct 12 2004.
[178] P. M. Keegan, C. L. Wilder, and M. O. Platt, "Tumor necrosis factor alpha stimulates cathepsin K and V activity via juxtacrine monocyte-endothelial cell signaling and JNK activation," *Mol Cell Biochem,* vol. 367, pp. 65-72, Aug 2012.
[179] P. M. Keegan, S. Anbazhakan, B. Kang, B. S. Pace, and M. O. Platt, "Biomechanical and biochemical regulation of cathepsin K expression in endothelial cells converge at AP-1 and NF-kappaB," *Biol Chem,* Jan 13 2016.
[180] N. Beckmann, R. Stirnimann, and D. Bochelen, "High-resolution magnetic resonance angiography of the mouse brain: application to murine focal cerebral ischemia models," *J Magn Reson,* vol. 140, pp. 442-50, Oct 1999.

[181] H. E. Ware, A. P. Brooks, R. Toye, and S. I. Berney, "Sickle cell disease and silent avascular necrosis of the hip," *J Bone Joint Surg Br,* vol. 73, pp. 947-9, Nov 1991.
[182] H. J. Clarke, R. H. Jinnah, A. F. Brooker, and J. D. Michaelson, "Total replacement of the hip for avascular necrosis in sickle cell disease," *J Bone Joint Surg Br,* vol. 71, pp. 465-70, May 1989.
[183] H. Hawker, H. Neilson, R. J. Hayes, and G. R. Serjeant, "Haematological factors associated with avascular necrosis of the femoral head in homozygous sickle cell disease," *Br J Haematol,* vol. 50, pp. 29-34, Jan 1982.
[184] R. A. B. Oluwagbemiga O. Ayoola, Uvie U. Onakpoya, Tewogbade A. Adedeji, Chidiogo C. Onwuka and Bukunmi M. Idowu, "Intima-media thickness of the common femoral artery as a marker of leg ulceration in sickle cell disease patients," *Blood Advances,* vol. 2, pp. 3112-3117, 2018.
[185] T. Krucker, A. Schuler, E. P. Meyer, M. Staufenbiel, and N. Beckmann, "Magnetic resonance angiography and vascular corrosion casting as tools in biomedical research: application to transgenic mice modeling Alzheimer's disease," *Neurological Research,* vol. 26, pp. 507-516, Jul 2004.
[186] E. P. Meyer, A. Ulmann-Schuler, M. Staufenbiel, and T. Krucker, "Altered morphology and 3D architecture of brain vasculature in a mouse model for Alzheimer's disease," *Proc Natl Acad Sci U S A,* vol. 105, pp. 3587-92, Mar 4 2008.
[187] E. Kim, S. Stamatelos, J. Cebulla, Z. M. Bhujwalla, A. S. Popel, and A. P. Pathak, "Multiscale imaging and computational modeling of blood flow in the tumor vasculature," *Ann Biomed Eng,* vol. 40, pp. 2425-41, Nov 2012.
[188] D. I. Bink, K. Ritz, E. Aronica, L. van der Weerd, and M. J. Daemen, "Mouse models to study the effect of cardiovascular risk factors on brain structure and cognition," *J Cereb Blood Flow Metab,* vol. 33, pp. 1666-84, Nov 2013.